SAHC

Numerical Analysis of Climatic Conditions Influence on the Current State of the St. Ann Church

Brenda Natalie Podio

Czech Republic | 2019

ADVANCED MASTERS IN STRUCTURAL ANALYSIS OF MONUMENTS AND HISTORICAL CONSTRUCTIONS

Master's Thesis

Brenda Natalie Podio

Numerical Analysis of Climatic Conditions Influence on the Current State of the St. Ann Church

CTU CZECH TECHNICAL UNIVERSITY IN PRAGUE

University of Minho

Czech Republic | 2019



ADVANCED MASTERS IN STRUCTURAL ANALYSIS
OF MONUMENTS AND HISTORICAL CONSTRUCTIONS

Master's Thesis

Brenda Natalie Podio

Numerical Analysis of Climatic Conditions Influence on the Current State of the St. Ann Church

Czech Republic | 2019

CZECH TECHNICAL UNIVERSITY IN PRAGUE
Faculty of Civil Engineering
Thákurova 7, 166 29 Prague 6, Czech Republic

MASTER'S THESIS PROPOSAL

study programme: Civil Engineering

study branch: Advanced Masters in Structural Analysis of Monuments and Historical Constructions

academic year: 2018/2019

Student's name and surname: Brenda Natalie Podio

Department: Department of Mechanics

Thesis supervisor: Tomáš Krejčí

Thesis title: Numerical Analysis of Climatic Conditions Influence on the Current State of the St. Ann Church

Thesis title in English see above

Framework content: The thesis aim is to simulate the behavior of the St. Ann church located in Viznov, Czech Republic, caused by climatic loading mainly due to temperature changes during the year, and their effect on the stress state and a possible damage evolution of the church. The 3D thermo-mechanical analysis was focused only on church walls. A historical review and detailed visual inspection were performed, followed by the definition of material properties. A finite element computer simulation of heat transfer using in situ temperature measurements and available climatic data was performed. Subsequently, a mechanical analysis was followed as a prognosis of a current stress state and possible crack nucleation. Results of the computation were analyzed in cooperation with the results of previous analyses of the structure. The thermo-mechanical analysis will be used as support for further structure reconstruction and rehabilitation.

Assignment date: 1/04/2019 Submission date: 8/09/2019

If the student fails to submit the Master's thesis on time, they are obliged to justify this fact in advance in writing, if this request (submitted through the Student Registrar) is granted by the Dean, the Dean will assign the student a substitute date for holding the final graduation examination (2 attempts for FGE remain). If this fact is not appropriately excused or if the request is not granted by the Dean, the Dean will assign the student a date for retaking the final graduation examination, FGE can be retaken only once. (Study and Examination Code, Art 22, Par 3, 4.)

The student takes notice of the obligation of working out the Master's thesis on their own, without any outside help, except for consultation. The list of references, other sources and names of consultants must be included in the Master's thesis.

....
Master's thesis supervisor Head of department

Date of Master's thesis proposal take over: July 2019

.....
Student

This form must be completed in 3 copies – 1x department, 1x student, 1x Student Registrar (sent by department)

No later than by the end of the 2nd week of instruction in the semester, the department shall send one copy of BT Proposal to the Student Registrar and enter data into the faculty information system KOS. (Dean's Instruction for Implementation of Study Programmes and FGE at FCE CTU Art. 5, Par. 7)

DECLARATION

Name:	Brenda Natalie Podio
Email:	nataliepodio@gmail.com

Title of the Msc Dissertation:	Numerical Analysis of Climatic Conditions Influence on the Current State of the St. Ann Church
Supervisor(s):	Eng. Tomáš Krejčí, Ph.D.
Year:	2019

I hereby declare that all information in this document has been obtained and presented in accordance with academic rules and ethical conduct. I also declare that, as required by these rules and conduct, I have fully cited and referenced all material and results that are not original to this work.

I hereby declare that the MSc Consortium responsible for the Advanced Masters in Structural Analysis of Monuments and Historical Constructions is allowed to store and make available electronically the present MSc Dissertation.

University:	CVUT – Prague
Date:	25/07/2019
Signature:	_____

This page is left blank on purpose.

ACKNOWLEDGEMENTS

First I would like to thank my supervisor, Prof. Tomáš Krejčí, whose dedication, experience and help were fundamental in the completion of this thesis. I would like to thank those who gave a contribution to this thesis with their previous work, suggestions and information. Thank you to Prof. Pavel Kuklik for organizing the site visit and for the valuable information shared.

A sincerest gratitude to the MSc Consortium that allowed me to participate in this Master's program, and with the fundamental support of a scholarship. A thank you to the professors at the University of Minho, for their experience, knowledge and passion that was shared with us.

I would like to thank Dr. Nigel Shrive, from the University of Calgary, for introducing me to the field, and believing in my passion and capabilities.

I am grateful for the friendships made this past year. I thank you for making this experience unbelievable, for the great times, for showing me that there is laugher in difficulties, and for supporting me through this year.

Last, but not least, I would like to thank my family, partner and friends for being my greatest strength. Thank you for the constant love, support and encouragement.

This page is left blank on purpose.

ABSTRACT

The Broumov Group of Churches, Baroque style monuments rich in history and architectural progression, is a symbol of Czech Republic's cultural heritage. The churches, built in a short amount of time, have several defining features making them unique for their architecture and cultural heritage. The St. Ann Church, built by Killian Ignaz Dientzenhofer in the early 18th century, belongs to the Broumov Group of Churches located in the small village of Viznov. Unfortunately, the church is found in its current damaged state in part due to its remote location and lack of maintenance over the decades.

The aim of this thesis is to simulate the behaviour of the St. Ann Church caused by climatic loading mainly due to temperature changes during the year, and their effect on the stress state and a possible damage evolution of the church. A detailed condition assessment is completed to understand the structure and current damaged state. A one-way coupled heat transfer analysis to simulate the distribution of temperatures for a one-year cycle using in-situ measurements and climatic data is performed. Insolation, wind effects and changes in air temperature around the structure are included in the heat transfer analysis. The computed temperature fields are used as loading for the static analysis of the St. Ann Church. The 3D thermo-mechanical analysis focuses on masonry church walls. Subsequently, a mechanical analysis is followed as a prognosis of a current stress state and possible crack nucleation. The static model is completed using linear elastic then nonlinear material properties. The stresses, deformations and structure behaviour obtained by means of the 3D finite element model are compared with damages observed on site.

Results show that the structure is periodically under temperature strain, with more adverse conditions affecting the structure under winter climatic loading. The most vulnerable parts of the structure include the thinly walled staircase connecting the bell tower to the main nave, the west end of the main nave near openings and the sacristy foundations and openings. The results from the numerical model are compared to observations made on the current state of the structure. Results of the computation are analyzed in cooperation with the results of previous analyses of the structure. The thermo-mechanical analysis is used as support for further structure reconstruction and rehabilitation.

Keywords: masonry church, nonlinear analysis, climatic conditions, heat transfer, numerical analysis, FEM, thermo-mechanical analysis, rehabilitation, a prognosis of crack evolution

This page is left blank on purpose.

ABSTRAKT

Broumovská skupina kostelů patří mezi symboly bohatého historického a kulturního dědictví České republiky. Jedná se o unikátní soubor devíti barokních kostelů postavených v poměrně krátké době počátkem 18. století. Jedním z těchto architektonických skvostů je kostel sv. Anny ve Vižňově od Killiana Ignáce Dientzenhofera. Díky svému umístění a kvůli nedostatku údržby po mnoha desetiletí se kostel nachází v poškozeném stavu.

Cílem této práce je analýza dopadu klimatických podmínek zejména teplotních změn na současný stav kostela. Základem analýzy je trojrozměrná numerická simulace přenosu tepla po dobu jednoho roku vycházející z klimatických dat a měření in situ, ve kterých jsou zahrnuty účinky větru a slunečního záření. Získaná teplotní pole jsou použita jako zatížení do následné mechanické analýzy stavu napjatosti a poškození konstrukce. Ve statickém konečně prvkovém modelu je nejdříve uvažováno lineární elastické působení materiálu pro získání základní představy o odezvě konstrukce na teplotní zatížení. Následně je analýza rozšířena o model nelineárního chování materiálu za účelem predikce možného poškození vlivem klimatických podmínek.

Výsledky počítačové simulace, které jsou konfrontovány se současným stavem, ukazují na periodické teplotní namáhání konstrukce s horšími účinky v zimním období. Mezi nejzranitelnější části stavby patří stěny kolem schodiště spojující zvonici s hlavní lodí a západním koncem hlavní lodi a sakristie. Výsledky výpočtů jsou dále analyzovány s přihlédnutím k výsledkům předchozích studií provedených na tomto kostelu. Tuto termomechanickou analýzu lze využít jako podporu pro další plánované sanace a rekonstrukce.

Klíčová slova: zdivo, nelineární analýza, klimatické podmínky, přenos tepla, numerická analýza, MKP, termomechanická analýza, rekonstrukce, prognóza vývoje trhlin

This page is left blank on purpose

TABLE OF CONTENTS

LIST OF FIGURES

LIST OF TABLES

1. INTRODUCTION

The St. Ann Church, built in the early 18th century, belongs to the Broumov group of churches constructed in Baroque style. The history and defining features of the Broumov group of churches and St. Ann Church make it rich in cultural heritage. Due to its remote location and lack of maintenance over the decades, the church is presently found in a damaged state.

The effect of climate, especially large temperature variations, can have a significant impact on deterioration processes and can subject the building to a high range of loading due to climatic conditions. These loads act on the building, and can cause long term damage to the construction, not only in the form of high temperature loading , but also frost induced damage. Durability of constructions, in terms of their resistance to environmental and climatic loads, is essential in allowing the longevity of the monument. When considering the many variables at play in historical constructions, the addition of a thermo-mechanical analysis could provide valuable insight into damages and their causes.

The objective of this thesis is to simulate the behaviour of the church caused by climatic loadings, mainly temperature changes during a one-year cycle, and their effect on the stress state and a possible damage evolution of the church. The thesis includes the simulation of temperature distributions, and the computation of thermal dilation movements and impact to current stress states.

The one-way coupled 3D thermo-mechanical analysis is focused only on church walls. A detailed condition assessment is performed to understand the current state of the structure. A finite element computer simulation of heat transfer using in situ temperature measurements and available climatic data is performed. Subsequently, a mechanical analysis is followed as a prognosis of a current stress state and possible crack nucleation. Results of the computation is analyzed in cooperation with the results of previous analyses of the structure. The thermo-mechanical analysis is used as support for further structure reconstruction and rehabilitation.

This page is left blank on purpose.

2. HISTORY

The St. Ann Church stands as a symbol rich in history and is a part of the Broumov Group of Churches built in Baroque style. The churches have several defining features making them unique for their architecture and cultural heritage. The following sections will explore the history and features of the region, providing an overview of the area where the St. Ann Church was built.

2.1 Overview of the Broumov Region

The Broumov Region is in the north east part of Bohemia, in the Hradec Kralove district and bordering with the region of Silesia in Poland [1]. The St. Ann Church is situated within the Broumov Highlands, surrounded by the Orlicke and Javori Mountains, as well as the Mirosov and Broumov Walls. The region is known for the unique sandstone rock formation landscape, formed during the early Mesozoic and Cretaceous period [2]. The area is also known for its cultural legacy consisting of traditional Baroque-influenced religious architecture. There are also ridges and moorlands, assembling the varied mountain elevations of the area spanning from 350 to 880m [1]. The large variability in the landscape and environment provides a large diversity of habitats, vegetation and animal life. The typical feature shared by the small Broumov villages is that they are relatively hidden, and remain hidden from a moderately short distance of a several hundred meters. However, the bell towers of the churches, usually constructed on elevated places are more easily spotted and reveal villages easily. Often, the churches are not on the highest terrace, and thus respect the natural conditions of a given site so that the individual buildings could be appropriately incorporated into the landscape [3].

2.2 Baroque Architecture in Czech Republic

The Baroque style in the Czech Republic developed in the period of the 17th and 18th centuries and flourished with the Catholic Church's victory of the Thirty Years War [4]. This religious war took place from 1618 to 1648 and although it started as a religious war between the Catholic and Protestant states that were part of the Roman Empire, the war became more a matter of which group would govern Europe. In the end, the conflict changed the geopolitical face of Europe and the role of religion and nation-states in society [4].

The Thirty-Year war triumph put the Catholic Church in a dominant position, encouraging Baroque architecture as a new style promoting Catholicism, while it tried to counteract Protestant's rejection of monuments and images. This created a divide in artistic approaches, leaving aside Renaissance styles and instead developing dynamic Baroque designs.

The years 1700-1750 are associated with a supreme, dynamic, radical Baroque – a version of the Baroque style that Czech architects took further than most of Europe [5]. This new architectural vision, featuring loose shapes, curving of walls and oval-shaped spaces, was used by famous Bavarian

architects and master builders Christoph Dientzenhofer and his son Kilian Ignaz Dientzenhofer, who lived in Prague [6].

These innovative professionals raised the standard of local architecture and gave a distinctive style to the shapes applied to the Broumov Group of Churches, whose renovations were contracted in 1709 [6].

2.3 Broumov Group of Churches

The Broumov group of churches is a complex of ten baroque style country churches located in small villages of the Broumov Region. Built in the early 18th century, these wooden churches were at the end of their service life and therefore in need of constant repair. Benedictine abbots envisioned the renovation of these monuments and hired Bavarian father and son architects / master builders Christoph and Kilian Ignaz Dientzenhofer for this project. Besides the need for renovated structures, the Abbots' purpose was also to renew the economic potential that the churches would mean for the Broumov Monastery, that was affected by the Hussite wars, also called the Bohemian Wars (1419-1434) and the Thirty Years War (1618-1648).

2.4 Design Guideline for the Reconstruction of the Churches

The Dientzenhofers worked within certain parameters established for the reconstruction of the monuments. These guidelines included a limited budget, a restricted main area consisting of a single nave temple, a bell tower and the inclusion of enough sitting space for the population of the village. All this had to be implemented with a simple design, solid structure and robustness to withstand the effects of weather in the region. An important location requirement was that the churches had to be situated within range of each other, and that the design of the churches had to blend to the landscape of the village and the countryside they were part of.

Due to the limited financial resources and the scarceness of local masons, the churches were built with false wooden ceilings, allowing enclosure walls of reduced thickness with a continuous ring beam binding the construction [6]. This kept similar elevations of the connecting buildings and enabled arch falsework. Christoph Dientzenhofer used the time-proven design of centralized oval or octagon plan with embedded pillars, while Kilian Ignaz Dientzenhofer developed and tested the basic theme of a lengthwise oval ground plan in various creative concepts [6]. The Dientzenhofers excelled in this project, and applying their unique creative originality they finished the reconstruction of the churches in a relatively short time. The design of the St. Ann Church and Broumov group of churches blend Baroque style architecture with the rocky landscape, giving the region a special and unique character.

3. STRUCTURAL SURVEY/ PRELIMINARY INVESTIGATION

In the case of historical constructions, ongoing decay problems, lack of maintenance and structural damages can be complicated to identify. Often, symptoms can be misinterpreted and damaging, or ineffective conservation works can be employed that do not address the underlying causes of damage. The following chapter deals with the complete, holistic review of the building in order to properly categorize damages, identify damage mechanisms and present valuable conservation approaches.

3.1 Description of Geometry

The St. Ann Church is characterized by curved outer walls in a continuous line connecting the bell tower, antechapel, main nave, organ loft and sacristy (Figure 3.1, Figure 3.2). The church is positioned at the top of a slope, oriented north east.

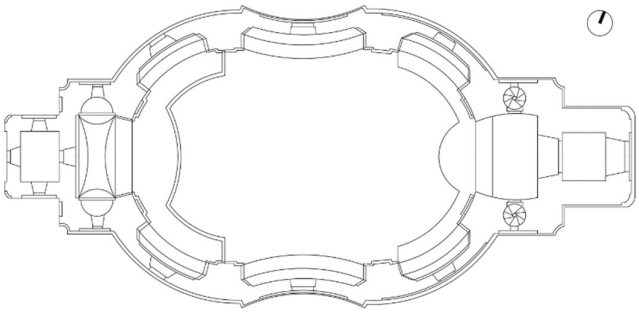

Figure 3.1 - St. Ann church plan

Figure 3.2 - Exterior view facing south

The unique rounded shape of the structure divides high and shallow niches set into the walls, enlarging the sensation of space inside the church (Figure 3.3). The small reliefs along the side of the oval main nave each have their own window approximately two thirds up the height of the wall allowing ample natural light. Two staircases leading to the upper floor balcony positioned at the front east section of the building where the organ and choir balconies are located can be seen in plan (Figure 3.1). The ceiling of the main nave is sail vaulted, with a false vault ceiling (Figure 3.4).

Figure 3.3 - Interior view facing west

Figure 3.4 Interior view facing east

The church is 20 m wide and 43 m long, including the bell tower and sacristy. The height of the main nave is 15.3 m while the tower height is 27 m. The main nave is 24 m by 15 m and the organ loft on the eastern end of the church is 6 m by 3 m. The wall thickness in the bell tower is approximately 1.7 m, while wall thickness ranges between 1 m -1.4 m in the main nave and sacristy. Pillars are approximately 2.6 m thick.

3.2 Materials

The materials used in the original construction and following reconstruction of the church play an impact in the deterioration mechanisms and stress states. These materials have different properties which have affected the damages incurred in the church throughout its history. The major building materials are outlined below.

3.2.1 Masonry Walls

The St. Ann Church walls are three leaf walls and are composed of a great variability in the stone arrangements with a rubble core. The thick walls are primarily composed of a variety of sandstones including red, grey and green sandstones as well as smaller percentages of siltstones and igneous stones [7]. The most abundant stone is the red and green sandstone, likely originating from local quarries in the nearby regions of Bozanov and Vernerovice [8].

The sandstones from neighbouring churches in the Broumov region were found to be very porous, with an average pore size of around 10e-5 m. The weathering of sandstones commonly includes the loss of the cementitious binder that can result in durability and deterioration issues. The porosity of the material can increase the risk of stone disintegration due to salt crystallization pressures and weathering from freeze thaw cycles. Since the durability of the stones is largely related to mineral composition, cementation type, rock texture and pore size distribution, these properties help to understand the high variability of differential deterioration seen in the structure.

In a lower percentage, ignimbrite and shale sandstones are present. In the interior of the building, the arches, domes and column capitals are composed of ceramic brick, observed in the areas where the render had detached completely exposing the structure underneath.

3.2.2 Timber Roof and Balconies

The roof is sail vaulted with a series of trusses and diagonal bracing composed of spruce timber. The false vault ceiling hanging from the sail vaulted roof is composed of timber boards, lathe and plaster. The roof tiling is ceramic, though conservation efforts employed the temporary use of steel sheathing to replace the ceramic tiling for water protection, as can be seen from Figure 3.2. The spiralled stairs, choir balconies and organ loft are also composed of spruce timber.

3.2.3 Mortar and Render

The render that at one point entirely covered the exterior facades is composed of a hydraulic lime mortar varying in thickness and sand additives [2]. The interior render is composed of a lime plaster with a more uniform thickness. The mortar is classified to be of medium to low porosity and density based on experimental testing performed on a nearby church belonging to the Broumov group of churches.

3.3 Structural Elements

The load bearing masonry walls are composed of a variety of stones with a rubble core (Figure 3.5). In the façades, relieving arches are observed from beneath the deteriorated render. The organized system of relieving arches are composed of larger blocks of stone, and exist throughout the structure directly above each door and window opening (Figure 3.6), as well as in the curved walls located above the larger openings, spanning the entirety of the wall section (Figure 3.7). The relieving arches serve to unload the delicate regions above the openings and control the force trajectories, allowing the masonry to act more effectively in compression using arch behaviour.

Figure 3.5 - Wall cross-section

Figure 3.6 - Relieving arch above opening, south wall

Figure 3.7 - Relieving arch in wall, south wall

In the interior of the structure it was noticed that beneath the deteriorated render the arches are composed of ceramic brick (Figure 3.8), significantly reducing the dead load and in turn the horizontal thrust from the arches. Although this was only directly observed for the arch under the main entrance, it is inferred to be consistent throughout the remainder of the structure.

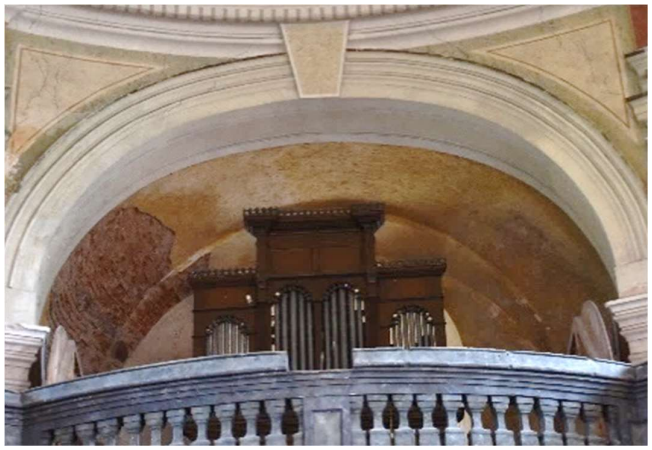

Figure 3.8 - Arch at east entrance exposing the brickwork underneath the deteriorated render

A few steel ties were seen in the masonry walls, beneath the deteriorated render in the west façade (Figure 3.9, Figure 3.10). The steel ties were only observed in the west façade, since the other façades are still covered in plaster. The ties serve to keep the three leaves of the masonry walls clamped to prevent bulging and detachment.

Figure 3.9 - East façade

Figure 3.10 - Steel tie on east façade

The structure rests on shallow foundations that have a depth of approximately 1.5 m, as determined from previous borehole investigations [7] [9].

The timber roof is composed of large trusses that appear to be overdesigned due to the large members in both the longitudinal and transverse directions (Figure 3.11) [10]. The timber roof allows for a shallow, light and wide ceiling that reduces the lateral thrust exerted on the masonry walls, as compared to a masonry vault ceiling. As well, the hanging false vault ceiling composed of timber boards and plaster is light and imposes small dead loads (Figure 3.12). Since the false vault ceiling is suspended on the sail vaulted trusses, the dead load is able to be applied directly to the walls and no additional horizontal loads are expected to be exerted on the masonry walls. Small holes can be seen at the top of the masonry walls that were a rudimentary technique employed by the Dientzenhofers to combat high humidity in roof areas [10]. These holes permit fresh dry air to circulate the roof as much as possible, though this did not prevent the development of moisture and fungus in the roof trusses.

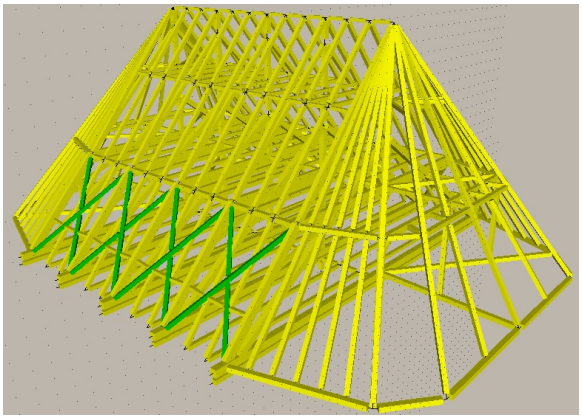

Figure 3.11 - Timber roof of the St. Ann Church [10]

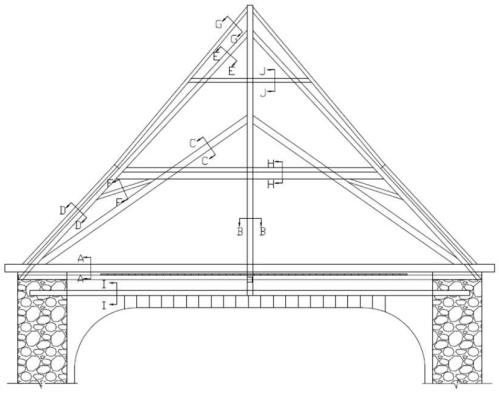

Figure 3.12 - Timber roof schematic showing false vault ceiling [10]

3.4 Previous Damages and Repairs

Previous works have been carried out on the St. Ann Church and include roof tile replacement, roof timber strengthening, repaired cornices, and miscellaneous stone replacement.

The roof has undergone several conservation works. In the past, destroyed sections of roof members due to fungi and moisture were strengthened by steel [10]. Two diagonal struts were also added in the main roof truss for additional reinforcement [2]. Furthermore, many of the ceramic roof tiles were replaced by steel plate sheets to patch the roof holes and leaks (Figure 3.2) [10]. Previously, the roof holes and leaks led to the destruction of the original sandstone cornices that contributed to issues in the roof system (Figure 3.13). These fallen cornices have since been repaired with brick (Figure 3.14). The high moisture content in the church and weathering led to additional issues and leaks in the timber roof that could have continued past the roof to affect the rest of the structure. Observing past damages, it becomes clear that weathering and lack of maintenance lead to an increase in the rate of deterioration.

Figure 3.13 - Fallen cornice [10]

Figure 3.14 - Repaired cornice

Other signs of reconstruction were observed by the presence of bricks in seemingly random locations that serve to patch the masonry wall in locations where original blocks appear detached (Figure 3.15 to 3.17). This was commonly seen surrounding the frames around doors, windows, cornices and close to foundations, where there was some separation noticed between the lower stones and foundations.

Figure 3.15 – Infill of bricks around window opening

Figure 3.16 - Infill of bricks above door opening

Figure 3.17 - Bricks located at separation of foundation stones

3.5 Current Damage State and Causes/ Condition Assessment

A visual inspection was conducted to observe the current condition of the building, identify damage patterns and establish possible causes. Damages have been classified under ICOMOS Guidelines following the visual inspection completed on April 17, 2019. The areas surveyed include the external and internal facades, bell tower and sacristy walls with a focus on the masonry elements. The mapping of the current damages and decay patterns was completed, as well as crack categorization in terms of location, pattern and type. Detailed damage maps are located in Appendix A.

3.5.1 Delamination of Render

The building plaster was partially or completely deteriorated and detached at some parts of the structure. The exterior of the building has severe plaster delamination, leading to large areas of exposed masonry and increasing the vulnerability of further stone weathering and deterioration.

The exterior render presents different rates of degradation. In the north-west, west and south-west oriented walls the render is washed away, popped out or completely delaminated. This results in practically absent plaster and exposed masonry (Figure 3.18). At other areas, the exterior plaster better resisted external actions and deterioration was superficially localized at the junction with the roof or at the bottom 1.5 m of the wall (Figure 3.19). Water penetration and weathering appears to be the main cause of plaster degradation. Freeze-thaw cycles, as well as soluble salt crystallization can generate a change in volume, leading to stone weathering and subsequent plaster bulging and detachment.

Figure 3.18 - Loss of render, south west wall

Figure 3.19 - Loss of render, east wall

In the interior of the building, the plaster deterioration and delamination was seen in areas of high moisture content, such as the bottom of walls and locations where roof leaks are present (Figure 3.20, 3.21). As well, due to the increase in moisture content and roof leaks, the partial delamination of plaster

from column capitals and complete plaster delamination from the arch barrel was seen (Figure 3.8, Figure 3.21).

Figure 3.20 – Plaster peeling due to moisture damage, interior north facade

Figure 3.21 - Render loss on column capitals, moisture staining

3.5.2 Stone Degradation

The exposed masonry presents different ranges of degradation, with the process triggered by environmental conditions such as rainwater, freeze-thaw cycles and salt crystallization, that can be accelerated by the detached plaster that otherwise provides a protective layer. The masonry walls are built using sandstones, igneous stones and bricks leading to differential degradation processes depending on the various material properties.

Differential weathering and alveolization can be observed primarily on the exposed red and grey sandstone on the exterior of the building. This is possibly due to inhomogeneities in the stone's chemical or physical properties, as well as the large variability in building stones (Figure 3.22). Differential erosion was commonly seen on most exposed masonry blocks, leading to a loss of the original surface and smoothed shapes. The weathering and erosion of the exposed masonry also led to a significant loss of the lime mortar matrix (Figure 3.23).

Figure 3.22 – Alveolization and erosion

Figure 3.23 - Erosion of stone and loss of mortar

3.5.3 Discolouration and Deposit

Black crust was most abundant on the front façade of the building and developed on areas that were protected against direct rainfall. The deposit of material resulting in soiling and surface staining that caused a dirty surface appearance was common on the exterior, and was particularly concentrated on the north façade (Figure 3.24, Figure 3.25).

Figure 3.24 – Deposit and soiling, north wall

Figure 3.25 - Deposit and soiling beneath opening, north wall

The darkening of surfaces due to moist areas and dampness was seen on both the exterior and interior of the building. The moist areas on the exterior of the structure are limited to the lower course on the north façade (Figure 3.26). On the other hand, the interior walls and floor are highly affected by moisture and have extensive signs of moist area staining and rising damp (Figure 3.27, Figure 3.28). This resulted in heavily damaged plaster with loss of cohesion at the bottom of the wall. The rising damp from the uninsulated foundations, a lack of ventilation and high air humidity are primary causes for the moisture damage in the building interior. More widespread damages were seen on the north and west walls that are not exposed to direct sunlight year-round and thus have wall drying delayed. Moist area staining was also noticed at several spot locations on the ceiling, serving as evidence of previous and ongoing roof leaks (Figure 3.29). It is unclear if the roof leaks are active, as the roof was previously repaired.

Figure 3.26 - Moist area on exterior north façade

Figure 3.27 – Moisture stains on interior walls, floor dampness

Figure 3.28 – Moisture damage on interior walls, floor dampness

Figure 3.29 – Moisture stains on ceiling plaster

3.5.4 Stone Biological Colonization

Biological growth was observed in the form of algae and lichens at the bottom of the walls throughout the church walls. At the exterior of the church, lichens and plants were seen on the bottom course of the north façade concentrated in the region where the detachment of foundation stone was found (Figure 3.30). In the church interior, biological growth on the south and north walls are limited to patches of algae, with few larger patches of algae and moss growth spread in the lower 1m portion of walls where the action of rising damp and high moisture was noticed (Figure 3.31).

Figure 3.30 - Biological growth on exterior, north

Figure 3.31 - Biological growth on interior, north

3.5.5 Cracks and Deformation

Several cracks throughout the structure were observed during the site inspection. These cracks are categorized by location and pattern and are described in detail below. On the exterior of the structure, cracks typically followed the bed and head joint in the masonry, and the presence of running water from a faulty gutter drainage system and subsequent weathering and loss of mortar could have aggravated crack propagation. More cracks were present in the interior of the building and were seen in the plaster.

Exterior

A series of cracks surrounding the opening on the south face of the bell tower were seen (Figure 3.32). These cracks could be due to the use of heavy church bells during the operational life of the bell tower.

Figure 3.32 – Cracks surrounding bell tower opening

Cracks on the exterior walls were noted in two other locations. A large crack with loss of mortar was seen on the west wall of the sacristy extending from the left corner of the opening to the top of the wall and follows the stair-like pattern of the stone units (Figure 3.33).

A crack was also observed above the boarded-up door opening on the north wall (Figure 3.34). This crack shows the formation of a false arch in the door lintel, as the lintel was heavily loaded by brick and stone units in a previous alteration. The brick and stone units are completely detached from the arch originally built into the wall, and they appear to pose no further cracking or deformations to the surrounding area.

Figure 3.33 - Cracks on sacristy wall above opening

Figure 3.34 - Crack and stone detachment above opening on north wall

At several locations throughout the perimeter of the structure, the lowest stone course was seen to begin to detach from the masonry wall and at some points has completely fallen from the wall. This detachment was most severe along the north perimeter of the structure (Figure 3.35). Varying degrees of stone detachment was seen along the west sacristy (Figure 3.36), and a spot location on the west wall (Figure 3.37). The stone detachment at ground level could be due to the presence of runoff water from the sloping nature of the site, as well as the location and poor condition of rainwater gutters that may have caused poor soil conditions.

Figure 3.35 – Stone detachment, north wall

Figure 3.36 – Stone detachment, north wall

Figure 3.37 – Stone detachment, south

Interior

Inside the building, it was common to observe vertical cracks in the plaster at the top of columns and surrounding column capitals as well as in the area above the column capitals in the ceiling render (Figure 3.38). The larger cracks can be evidence of stress concentrations or point loading applied from the roof structure. As well, several of these cracks appear to be aggravated by the delamination of plaster and water ingress from previous roof leaking that can be seen from the stained ceiling and holes in the ceiling exposing the delamination of plaster.

Figure 3.38 - Vertical cracks at column capitals and ceiling plaster detachment

Cracks with varying degrees of thickness and length were seen on the plaster of the transverse section of several arches that are situated above openings. The cracks in the arches were typically small in thickness and ran close to the keystone arch (Figure 3.39).

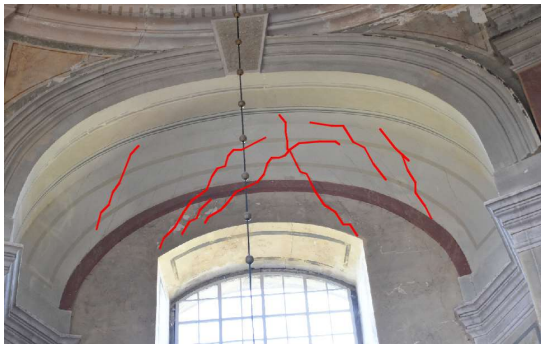

Figure 3.39 – Transverse crack in arch, north wall

A crack was observed in the longitudinal direction of the arch at the west side of the church, extending to the domes on either side, as well as towards the openings (Figure 3.40). The longitudinal crack extends towards the small domes on either side of the arch and intersects the window frame (Figure 3.41).

Figure 3.40 - Longitudinal crack in arch barrel, extending towards opening

Figure 3.41 - Extension of longitudinal crack into openings

A series of thin vertical cracks can be observed throughout the main nave. Vertical cracks were commonly seen beneath the window openings (Figure 3.42) and in the plaster of walls on the north and south facades below balconies (Figure 3.43).

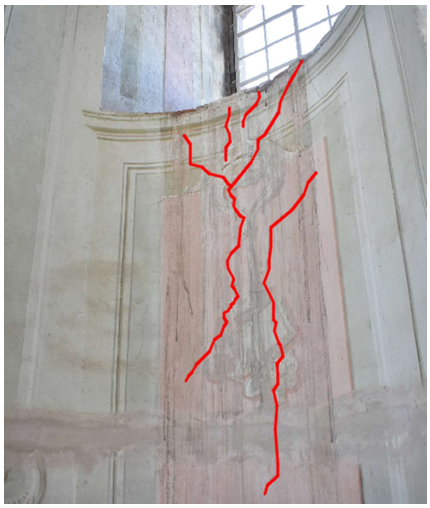

Figure 3.42 - Cracks below window openings

Figure 3.43 - Vertical cracks below balconies

The St. Ann church presents a series of damages which are likely to be largely related to the lack of maintenance, problems of water penetration and high moisture content in the walls. After the second World War, religion was prohibited by the communist regime and churches closed. This lack of use of churches in the countryside caused the rapid degradation of the St. Ann church. High air humidity at low temperatures increase the likelihood of condensation and subsequent damage. Masonry structures such as churches are highly affected by condensation as it is common to observe high moisture contents and constant cool temperatures, due to temperature fluctuations prevented from large walls and a lack of heating and air ventilation. Climatic conditions can significantly impact deterioration processes. Climatic loading can act on the building causing long term damage to the construction, for example from temperature loading or freeze thaw cycles. The thermo-mechanical analysis will serve to understand the current stress state and determine whether some of the above mentioned damages can be explained from the effects of climatic temperature loads.

3.6 Thermography

A thermographic camera was used during the visual inspection completed on April 17, 2019 to gain an understanding of the temperature variations that can exist on the structure during a given time period. The weather during the time of inspection was sunny with high winds and a temperature high of 13°C and a low of 1°C [11]. Temperature readings were taken at several locations for each wall orientation in both the interior and exterior.

Measurements on the exterior of the structure were taken at 10 locations up the height of the structure, approximately every 1.5m. In this way an understanding of the distribution of temperatures was attained. A summary of the measured temperatures using the thermographic camera are presented in Table 3.1. Depending on the wall orientation, temperatures varied significantly. The highest temperature readings

(32 ºC) were observed on the south wall due to the continuous sun exposure during the day, while the lowest temperature was recorded on the north wall (1 ºC) as could be expected due to the lack of direct sunlight. Temperature differences along the height of one wall from the foundation to the roof level of the structure would vary from 4 ºC (east wall) to 18.5 ºC (south). The east wall had regions of shadowing that brought the average temperature measurements down.

Table 3.1 – Thermography camera results

Exterior Building Orientation	North	East	West	South
T Avg (ºC)	3.4	12.4	5.6	26.6
T Max (ºC)	5.3	14.5	10.6	32.1
T Min (ºC)	1	10.5	3	13.6
ΔT (ºC)	4.3	4	7.6	18.5

Temperatures on the exterior of the structure varied significantly not only due to wall orientation and shadowing, but also due to nonhomogeneous material characteristics and the presence of plaster (Figure 3.46). The effect of the large variability in materials can be seen in Figures 3.44 to Figure 3.46.

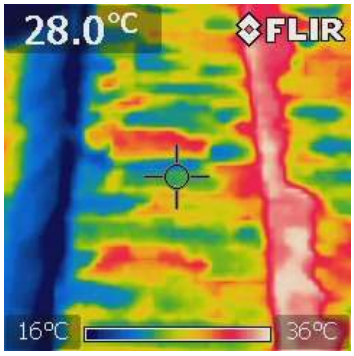

Figure 3.44 - Thermography camera, south wall

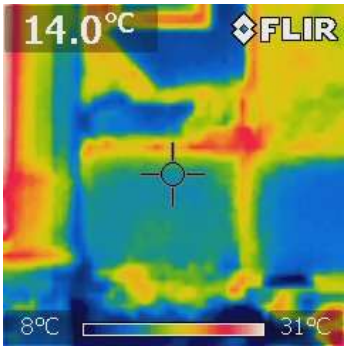

Figure 3.45 - Thermography camera, east wall

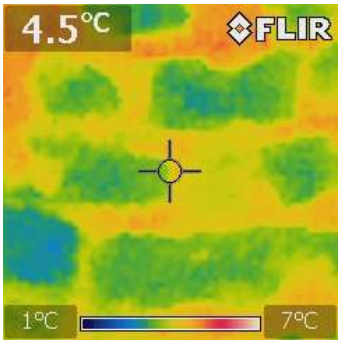

Figure 3.46 -Thermography camera, west wall

The differences in surface temperatures were much greater on the exterior of the structure than the interior. Temperatures in the interior of the structure remained relatively consistent and did not vary more than 1 ºC throughout the height of each wall. The maximum temperature measured in the interior of the structure was 6.3 ºC, while the minimum temperature was 2.9 ºC.

The interior surface temperatures change at a much slower rate than the exterior. In the interior it was possible to observe decreased temperatures for the lowest 1m of wall likely due to the effect of the uninsulated foundations and high moisture content as can be observed in the colour differences in Figures 3.47 to Figure 3.49.

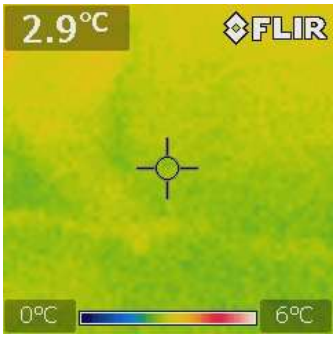

Figure 3.47 - Thermography camera, east wall

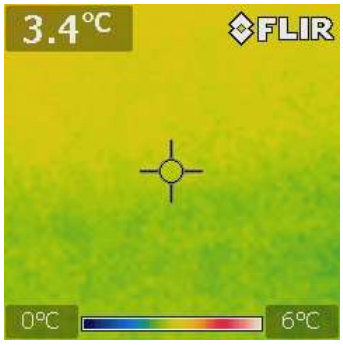

Figure 3.48 - Thermography camera, west wall

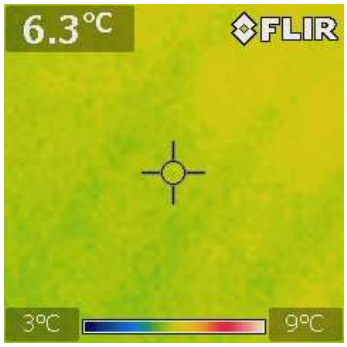

Figure 3.49 - Thermography camera, south wall

3.7 Climate of Broumov Region

To better understand the current damage state and evolution of damages, the microclimate was assessed. The climate of the region can have a significant impact on deterioration processes and can subject the building to a high range of loading due to temperature changes. Durability of constructions in terms of their resistance to environmental and climatic load are essential in allowing the longevity of the structure. These loads act on the building, and can cause long term damage to the construction, for example due to temperature loading or frost induced damage [12].

Climatic conditions are typically not uniform, and will vary significantly depending on the locality and elevation of the building. Therefore, an overview of the local climate in the Broumov region is detailed below, providing basic information on the type of climate experienced in this region.

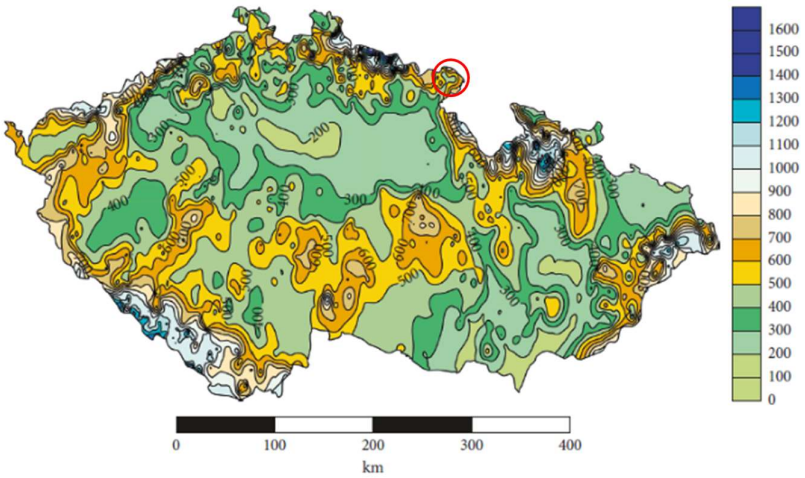

Figure 3.50 - Czech Republic elevation map with Broumov region highlighted in red circle [12]

The Broumov region can be classified geographically according to the Koppen-Geiger Climate Classification as a zone with full humidity experiencing snowy winters and warm summers [13] . The St. Ann Church is located at an elevation of 400m (Figure 3.50).

During the summer months, temperatures can reach a high of 34 ºC. The warm temperatures can help dry walls, and decreasing the humidity level inside the church. On the other hand, during the winter months temperatures can reach a low of -15 ºC.

Large snowfalls can also be observed in the Broumov region according to the Region IV classification from the Czech Annexes of Eurocode 5. These snowfalls can lead to higher roof loads, roof leaks and roof and wall dampness problems if the snow accumulates on the ground level. In Middle Europe, one of the most common long-term damages to building enclosures is frost-induced damage [12]. Sandstone masonry provides the highest resistivity to severe environmental actions, while clay bricks are extremely susceptible to frost-induced damage [12]. Since the St. Ann Church is composed of both materials, it can be at risk of frost induced damage. As well, the low winter and high summer temperatures can cause damage due to the thermal loading and repetitive freeze thaw cycles.

The structure can experience vulnerability to wind due to its exposed location on the highest part of the terrain, and the lack of surrounding obstructions such as trees and other buildings. Wind velocity and direction can have a significant influence on temperature distribution and wall dampness.

All detailed weather data was obtained from the Czech Hydrometeorological Institute. The readings obtained for the purpose of this thesis included the hourly values of temperature, relative humidity, precipitation, wind direction, wind velocity, diffuse and direct shortwave radiation, sky longwave emission radiation, and longwave emission radiation provided in the form of statistically averaged data from the past 10 years.

Ignoring the climatic conditions of a building due to its locality and environment can lead to the incorrect selection of construction materials, design and subsequent lack of durability and functionality. Environmental and climatic loading affects most buildings, and can be manifested by various types of damages ranging from structural damage to superficial cracks [12]. The structural behaviour and potential damages caused by climatic conditions, external actions and temperature loading will be evaluated in detail in the following chapters.

3.8 Data Monitoring

A multidisciplinary thesis assessing water transport in the soil masonry system of the St. Ann Church collected data readings on temperature, pressure head, and the water contents of the soil and masonry for over one year [12]. The long-term monitoring system was installed in the north masonry wall of the church (Figure 3.51) and in the neighbouring soil (Figure 3.52). The temperature readings from the masonry wall were taken at several locations along the bottom portion of wall, and the readings from

the soil directly adjacent the masonry wall were also taken at various depths [9]. The temperature readings from this research work will be used as input values for the thermal analysis.

Figure 3.51 – Monitoring system location in church [9]

Figure 3.52 – Monitoring system in neighbouring soil (site A) [9]

Measurements from this research work found that the direct contact of the highly saturated soil and masonry foundations and walls leads to a high moisture content in the walls, noticed through temperature changes and further verified through the pressure potential and humidity readings [9]. The temperature of the masonry foundations and bottom 30cm of wall were observed to be comparable to soil temperatures [9].

The temperatures measured by the sensors (CS 650, T8) in the soil adjacent the north masonry wall correspond to readings taken from the neighbouring soil directly adjacent to the church wall (Figure 3.53). The temperatures measured in the soil and inside the church are included in Appendix B.

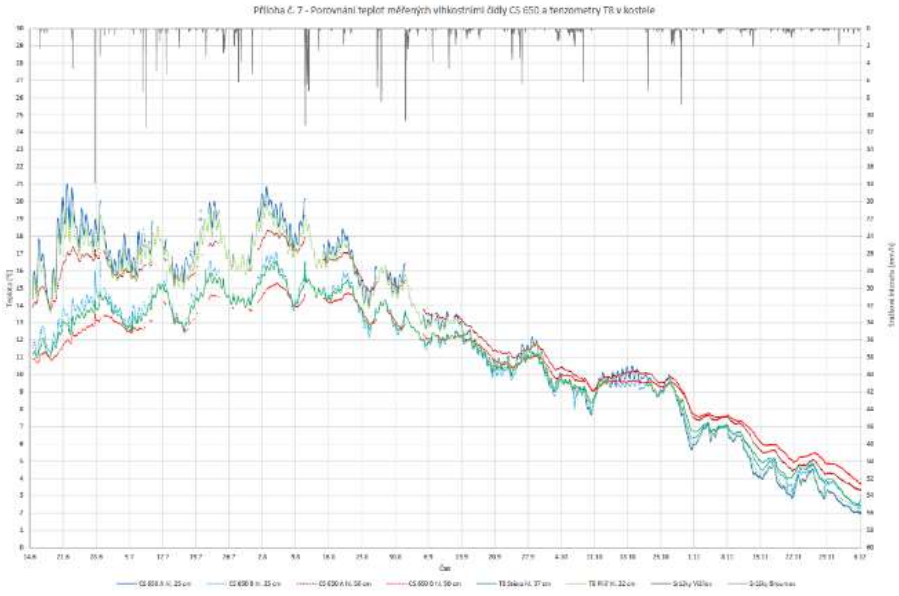

Figure 3.53 - Temperature readings inside church [9]

The location of the temperature and humidity sensors are shown in Figure 3.54. The temperatures measured and averaged at P1 and S1 will be used for input temperatures in the thermal analysis for the internal surfaces. While the temperatures measured and averaged at P5 and S5 will be used for input temperatures in the thermal analysis for the foundation level.

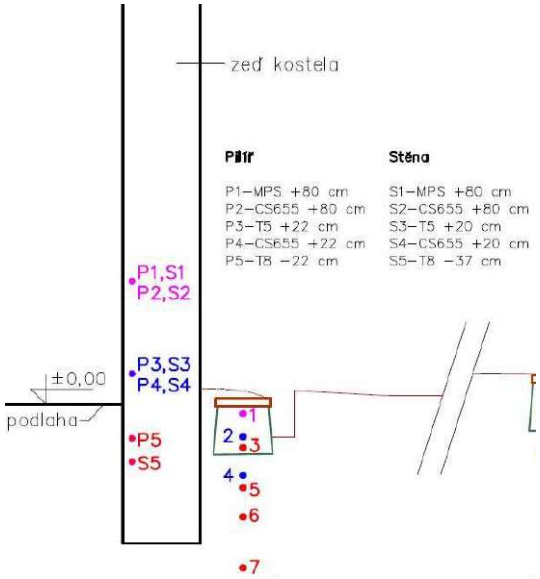

Figure 3.54 – Schematic of temperature gauge locations(zed kos= wall of church) [9]

4. MODELLING

4.1 Modelling Approach

The 3D thermo-mechanical analysis focuses only on the masonry walls and is approached as a one-way coupled analysis to manage model complexity. The one-way coupled engineering approach means that the heat transport problem is solved independently from the mechanical analysis and other transport mechanisms like moisture.

The results from the heat transport problem is used as a load for the mechanical analysis. The definition of constant material properties, and a finite element computer simulation of heat transfer is completed using in situ temperature measurements and available climatic data.

Then, using the computed thermal field fluctuations from the heat transport problem as input, a static mechanical analysis is completed. The static analysis is performed first using an elastic model, followed by a non-linear numerical analysis of the structure to determine a prognosis of the current stress state and possible crack nucleation. The thermo-mechanical analysis considers self-weight and roof dead loads, and linearizes the following temperature differences as loading:

- Combination A: Average temperature state to highest temperature state (summer)
- Combination B: Average temperature state to lowest temperature state (winter)

Combinations A and B are selected in order to simulate a one-year temperature cycle, since the application of the full range of temperatures during this period is unrealistic due to computational limitations.

The simplified coupled analysis is performed using the open source package SIFEL (Simple Finite Elements) and programs ATENA and GiD. SIFEL is used for the thermal analysis, ATENA Studio is used for the static analysis, and GiD is used for data preparation and mesh generation.

Since ATENA Studio and SIFEL do not support the definition of the geometrical model, and operate directly on the numerical model, the input files must be created from the geometric model using the pre-processor, GiD [14]. GiD is also used for post-processing the SIFEL results, while ATENA Studio has a built-in post-processor for viewing the results.

4.2 FEM Model

4.2.1 Geometrical Model

The AutoCAD geometrical model was provided from previous studies by P. Gajjar at the Czech Technical University in Prague, and was used as the base file for the final model shown in Figure 4.1 [7].

For the purposes of this study, it is necessary to use a model that closely simulated site geometry therefore modifications were made to the original file. These modifications included the addition of door openings and miscellaneous window openings on the north and south walls, the addition of the east and west arch and dome system and removing the foundation depth that was originally added to the wall height.

Geometrical modelling assumptions include the simplification of the arch window openings that were modelled as rectangular. The arches on the interior of the structure were not filled to the top of the exterior wall, due to the hanging false vault ceiling that extends into this area.

The interface between adjacent elements is considered to be rigid, suggesting that connections between pillars, walls, tower and arches were properly connected to one another and the structure behaves monolithically, as a single unit. This implies that sliding between adjacent elements is not possible. Although this is an idealization, it is believed that it does not deviate greatly from the real behaviour of masonry as the stones used in the construction of the church were typically rough, increasing friction. The masonry walls were also likely built homogenously, so the stones create an interlocking pattern, connecting different elements. The building is imported into GiD as a single volume, so that the building is modelled as a monolithic structure with rigid connections

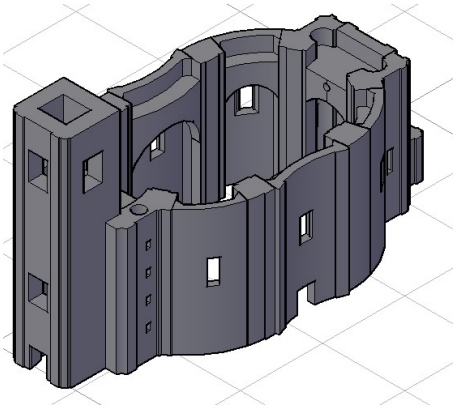

Figure 4.1 - Autocad model of St. Ann's Church

4.2.2 Mesh and Elements

Meshing is done using the pre and post processor GiD V.14.0.2. Due to the complex geometry, tetrahedral elements (Figure 4.2) were required for the analysis since they were the only element capable of meshing the structure. The mesh for both the thermal and mechanical analysis were kept consistent, and consisted of 3D solid, 4 noded, tetrahedral elements with linear shape functions. These are isoparametric elements defined by one Gauss integration point. The mesh is kept consistent for the heat transfer analysis and the subsequent static analysis to allow for temperature fields to be input as loading for the static model, regardless of the use of different softwares (SIFEL and ATENA).

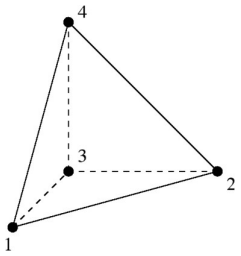

Figure 4.2 - Tetrahedron elements [36]

The tetrahedral elements are not often used for stress analysis due to its poor performance modelling bending and stress and strain prediction [15]. Linear tetrahedrons tend to stiffen the structure when subjected to bending [16]. To overcome this problem, a refined mesh is used and special attention is given to the results considering this element type is used. To model bending more accurately, higher order elements of the tetrahedral family could have been used, though the use of 8 noded tetrahedral elements with quadratic shape functions are not possible due to computational limits from the large number of degrees of freedom. In thermal analyses the linear tetrahedral element is acceptable since the objective of the analysis is to obtain only the primary variable, temperature [17]. The refined mesh is ensured to have a minimum of 5 elements across wall thickness to ensure the heat transfer and stress states were adequately modelled.

Due to complexities in the geometrical model, meshing errors were prevalent. The mesh is created using a slow size transition for the unstructured mesh generation. This controlled the transition between different element sizes, generating a more uniform size transition throughout the mesh. To further refine the mesh, the surface mesher used in GiD is RSurf. Contrary to the default surface mesher that works in the 2D space, first meshing surfaces and mapping those surfaces into the 3D space, RSurf works directly in the 3D space, which is a slower process but provides a better quality mesh [14]. Using the slow size transition and RSurf mesher a better quality mesh is able to be produced.

The final mesh has size 0.3 m elements that formed 323 261 nodes and 1 725 758 elements for the thermal and static analysis (Figure 4.3).

Figure 4.3 – Final mesh

4.3 Material Properties

The thermal and mechanical material properties were found using homogenization techniques of the masonry components properties. The thermal and mechanical material characteristics could not be determined from tests as no interventions into the structure were permitted, therefore past studies and literature were consulted.

4.3.1 Thermal Material Properties

The thermal material properties were homogenized based on the volumetric ratio of stone units and mortar in a square unit of masonry wall. It was assumed that the inner rubble core was composed of a similar ratio of materials as the outer leaves, therefore the ratio of areas was found for the units and mortar that composed a 1 m x 1 m section of masonry wall on the exterior of the structure (Figure 4.4). The areas of each material were found and multiplied with their respective thermal material properties. The thermal material properties of the masonry wall and its constitutive components are summarized in Table 4.1 [18]. Homogenization of the thermal material properties based on volume was used for this study since it was assumed that the thermal behaviour of the structure will depend mostly on the applied temperatures and boundary conditions, rather than the individual thermal material parameters.

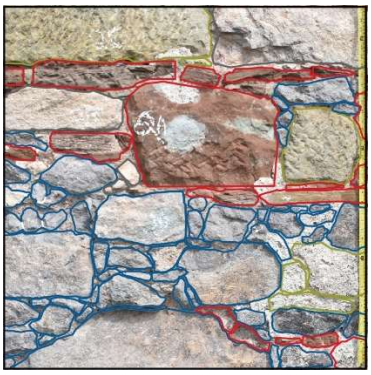

Figure 4.4 - Square 1 m x 1 m wall with stones marked

Table 4.1 – Thermal material properties

Material	Colour of Stone Outline	% Area	Density, ρ (kg/m^3)	Specific heat, c ($Jkg^{-1}K^{-1}$)	Coefficient of heat conduction, λ ($Wm^{-1}K^{-1}$)
Coarse Grained Arkose Sandstone	Yellow	16.0%	2047.29	674.06	2.255
Red Grey Sandstone	Red	20.4%	2433.64	646.49	3.665
Ignimbrite/ Blue Sandstone	Blue	38.5%	2182.99	672.62	2.348
Grey Limestone	Grey	10.6%	2223.94	759.91	3.227
Mortar	-	14.5%	1756	905	0.726
Final Properties			2154.8	710.4	2.459

4.3.2 Mechanical Material Properties

The mechanical material properties were defined in a previous study using a 2D numerical analysis to homogenize the material properties of transversal and longitudinal wall sections of the St. Ann Church [7]. This study determined the material parameters by modelling several longitudinal and transversal sections of walls until post peak behaviour was reached. From here, a homogenization technique was used to convert the 2D longitudinal and transversal models' peak compressive strength into an equivalent parameter for use in a 3D model [7]. The tensile strength was chosen as 10% of the compressive strength [7] [19]. The compressive fracture energy was determined using Model Code 90 with a ductility index (d) equal to 1.6 mm [7]. A summary of the mechanical material properties used for this analysis are presented in Table 4.2. The selected material model is discussed in Chapter 6.4.

Table 4.2 – Mechanical material properties

Youngs Modulus	E	2 GPa
Poissons Ratio	v	0.2
Density	ρ	2154.8 kgm^{-3}
Coefficient of Thermal Expansion	α	7*10-6 K^{-1}
Tensile Strength	f_t	0.2 MPa
Tensile Fracture Energy	G_t	70 Nm^{-1}
Compressive Strength	f_c	2.9 MPa
Onset of Crushing	f_{c0}	0.45 MPa
Plastic Strain at compressive strength	ε_{cp}	-0.00145
Critical compressive displacement	w_d	-0.0005 m

5. THERMAL ANALYSIS

5.1 Formulating the Problem

This thesis sets out to determine if the deformations and damage mechanisms observed in the structure are caused by thermal volumetric changes. For this reason, the distribution of temperatures throughout the structure were modelled numerically over a period of one year using the open source finite element computer code SIFEL [20]. Specifically, the TRFEL code is used to simulate the heat transport process for the climatic boundary conditions (temperature, relative humidity, driving rain, wind speed, wind direction, shortwave radiation) [21].

In order to understand the numerical solution of the heat transfer analysis completed in SIFEL, a brief formulation of the heat transfer problem will be described below. A more detailed description of the heat transfer problem formulation can be found in [22].

The heat flux, proportional to the thermal conductivity can be described by Fourier's Law [22] (Eq. 1):

$$q = -\lambda \nabla T, \tag{1}$$

where q is the heat flux [Wm^{-2}], λ is the coefficient of heat conduction [$Wm^{-1}K^{-1}$], ∇ is the gradient operator and T is temperature [K]. The negative sign is a consequence of heat transferred in the direction of decreasing temperatures. The temperature T is a scalar temperature field and heat flux q is the amount of energy being transferred per unit time.

Given the case of no temperature sources, the energy balance equation for steady state heat transfer can be written as (Eq. 2):

$$\nabla \cdot (q) = 0,$$

$$\nabla \cdot (-\lambda \nabla T) = 0, \tag{2}$$

where $\nabla \cdot$ is the divergence operator. Eq. b shows that there are no temperature sinks or sources and indicate that heat transfer is in a steady state.

In the case of non-stationary heat transfer, the energy balance equation can be rewritten as (Eq. 3):

$$\rho C \frac{\partial T}{\partial t} = -\nabla \cdot (q), \tag{3}$$

where ρ is the volume weight [kgm^{-3}] and C is the specific heat capacity [$Jkg^{-1}K^{-1}$]. Combining Eq. 1 and rewriting Eq. 3 results in (Eq. 4):

$$\nabla \cdot (\lambda \nabla T) - \rho C \frac{\partial T}{\partial t} = 0 \tag{4}$$

The modelling of transient transport processes leads to the solution of a system of non-linear partial differential equations (Eq. 4), solved by SIFEL by numerical integration with respect to time [21].

Moisture can influence the material characteristics in Eq. d. For this analysis, the problem is simplified and constant material characteristics (as described in Chapter 4.3.1), independent of moisture and temperature fluctuations, were used. As well, water freezing is not accounted for. These assumptions may cause the modeled temperatures to differ from the real values slightly.

5.2 Climatic Conditions

The time dependent temperature loads that correspond to the boundary conditions are termed climatic conditions. For this analysis, the following climatic conditions were used with the following notation [21]:

- Temper [K]: Environmental temperature
- VerRain [$kgm^{-2}s^{-1}$]: Vertical rain flow density, normal to the ground
- RelHum [-]: Environmental relative humidity
- WindDir [rad]: Wind direction (0 o denotes north, 90 o east, 180 o south and 270 o west)
- WindVel [ms^{-1}]: Wind speed
- DifRad [Wm^{-2}]: Diffuse short wave radiation on a horizontal surface
- DirRad [Wm^{-2}]: Direct short wave radiation on a horizontal surface

The climatic data records listed above were assigned to the boundary conditions that will be further described below.

The input temperatures (Temper) for the heat transfer analysis used were three sets of temperature data described in Chapter 3.7 and 3.8 and can be found in Appendix C. The remainder of the climatic conditions of the computational model are defined by statistically averaged weather data characterizing the environmental conditions in the Czech Republic in the Broumov region, taken from Czech Hydrometeorological Institute [23].

5.3 Boundary Conditions

Several factors can influence the temperature of the structure, including: the velocity and temperature of surrounding air flow, intensity of absorbed solar radiation and the presence of water in varying forms including evaporation from surfaces and pores, absorption and desorption, and condensation [24].

Due to the complexity of the external factors and the large number of degrees of freedom of the structure, the model included only the effects of the air temperature around the structure, the velocity and direction of surrounding air flow and the intensity of the absorbed solar radiation.

The boundary conditions describe the surface properties when exposed to external climatic loads [21]. The following sets of boundary conditions are assigned to the system of equations (Eq. 4) in the spatial domain of the problem.

Constant Temperature Increment

The constant temperature increment defined by the Dirichlet boundary condition (Eq. 5) was assigned to the interior of the structure:

$$T(x,t) = \bar{T}(x,t), \tag{5}$$

where $\bar{T}(x,t)$ is the prescribed temperature [K].

The Dirichlet boundary condition was assigned to two separate regions. These regions include the inside of the structure and the bottom surfaces where there is soil interaction.

The interior of the structure faces were assigned the *internal temperature climatic data* as previously defined from averaged in-situ measurements located in the church interior (refer to Chapter 3.8, data located in Appendix C, Figure C.1).

The bottom surfaces of the structure were assigned the *bottom temperature climatic data* as previously defined from averaged in-situ measurements located at the foundation level (refer to Chapter 3.8, data located in Appendix C, Figure C.2).

Heat Conduction

The heat transfer from the surrounding air temperature to the structure was described by the Cauchy boundary condition (Eq. 6) [22].

$$q(x,t) = \alpha\big(T(x,t) - T_{\infty}(x,t)\big), \tag{6}$$

where α is the heat transfer coefficient [$Wm^{-2}K^{-1}$], T is the surface temperature [K], T_{∞} is the ambient temperature [K] and q is the heat flux [Wm^{-2}].

The heat conduction boundary condition was assigned to two regions: the exterior surfaces of the structure, and the top surfaces where the masonry walls are in contact with the roof. The climatic conditions required for the heat conduction boundary condition are the *environmental temperature* as described by the statistical data provided from the Czech Hydrological Institute (refer to Chapter 3.7, data located in Appendix C, Figure C.3). The top surfaces where the masonry walls are in contact with the roof were assigned a transfer coefficient equal to 1.5, to simulate the effect of insulation provided by the timber roof structure.

The extended model in SIFEL was used which determined an exchange coefficient to account for the influence of wall direction, wind direction and wind speed on temperature [21].

For model simplification the effect of insulation provided by windows and doors was not accounted for, and no boundary conditions were assigned to these regions.

Shortwave Radiation

The last effect included in the model is solar radiation and comes in the form of shortwave and long wave radiation. These effects include: direct and diffused shortwave radiation, longwave radiation emitted by the surface of an object and longwave radiation reflected by the atmosphere [25]. Shortwave radiation is emitted from the sun and is not converted into heat until it hits an object [26], while longwave radiation is emitted from an object that has received shortwave energy [26].

The radiation boundary condition is modelled based on the following equation (Eq. 7):

$$q(x,t) = \varepsilon\sigma\left(T^4(x,1) - T_s^{\infty}(x,t)\right), \tag{7}$$

where ε is the emissivity of the surface and σ is the Stefan Boltzmann constant, 5.67x10^{8} Wm^{-2}K^{-4}. The shortwave radiation boundary condition is based on (Eq. 7), however the extended model was used in SIFEL. This boundary condition describes the difference between the thermal energy that is released due to radiation emission and gained through radiation absorption [27].

Due to the available data and problem simplification, the influence of solar radiation was calculated in the form of shortwave radiation using the extended SIFEL model. The radiation flux was calculated from the direct and diffuse radiation taking into account the wall inclination and direction [21].

5.4 Initial Conditions

The temperature at the beginning of the analysis was unknown, and therefore set to be 10°C since the climatic data appeared to trend towards this temperature during the spring months (when the analysis was started). The structure was simulated for a one-year period, so it can be assumed that the temperature distribution throughout the structure is independent from the influence of the initial temperature assumption.

5.5 Results

The numerical model for heat transfer was run in SIFEL and using a time step of one hour the temperature distribution of the structure was simulated for a period of one year. The maximum temperatures experienced by the structure was 40.9°C in summer, and -17.2°C in winter, both located at nodes on the exterior surfaces of the structure.

The temperature evolution of the structure for the one-year period can be seen graphically represented in Appendix D. The internal temperature of the structure was seen to oscillate at a slower rate than the external temperatures. The temperature transitions inside the structure are slow and gradual when changing from summer to winter extremes. While on the exterior of the structure, the structure experiences sudden changes in temperature that vary significantly depending on the season and time of day. During one day, a single node on the exterior wall can experience a temperature difference of ΔT= 22.2°C in summer, and ΔT= 8.73°C in winter. On the other hand, during one day a node on the interior surface can experience a temperature difference of ΔT= 0.41°C in summer, and ΔT= 0.18°C in

winter. The temperatures for the inside to outside monitored nodes are summarized in Tables 5.1 and 5.2.

Table 5.1 – Temperature distribution along wall cross section, summer

Summer	Inside	Outside
Node	120777	121112
T Max (°C)	15.94	22.20
T Min (°C)	15.53	4.30
ΔT (°C)	0.41	22.20

Table 5.2 - Temperature distribution along wall cross section, winter

Winter	Inside	Outside
Node	120777	121112
T Max (°C)	2.41	-5.90
T Min (°C)	2.23	-14.63
ΔT (°C)	0.18	8.73

It was observed that temperatures on the exterior surface of the walls fluctuated significantly depending on wall orientation due to radiation effects. This effect can be seen illustrated when comparing the structures at the same time step in Figure 5.1 and Figure 5.2 (summer) and Figure 5.3 and Figure 5.4 (winter). The temperature difference seen at a single time step between the exterior north and south walls were observed to be approximately 6°C in summer months and 2.5°C in winter months. The temperature difference between the exterior surfaces during the winter months was much less due to the reduced amount of sun radiation.

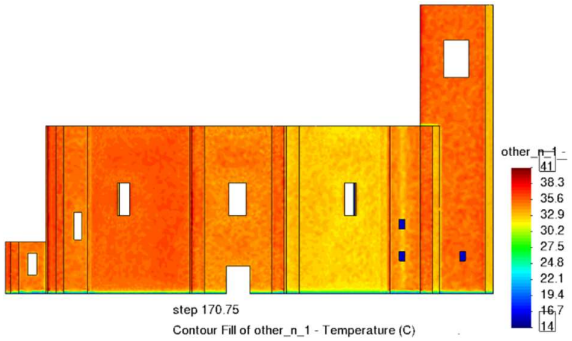

Figure 5.1 – Temperature field, time step 170.75 (summer)

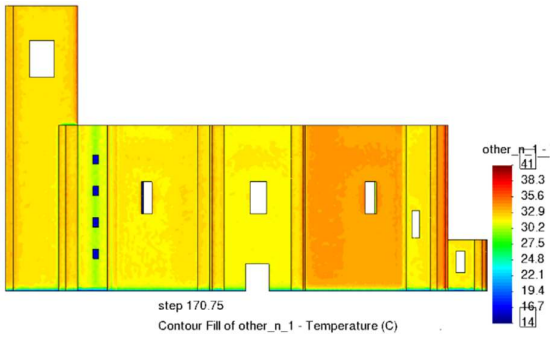

Figure 5.2 - Temperature field, time step 170.75 (summer)

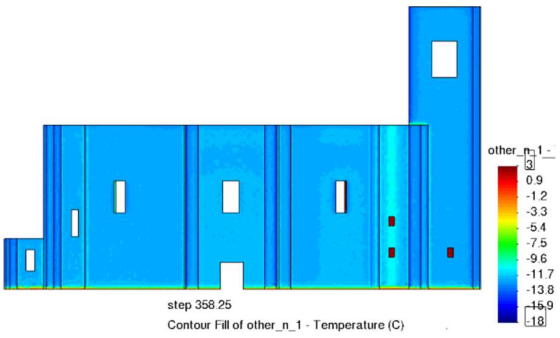

Figure 5.3 - Temperature field, time step 358.25 (winter)

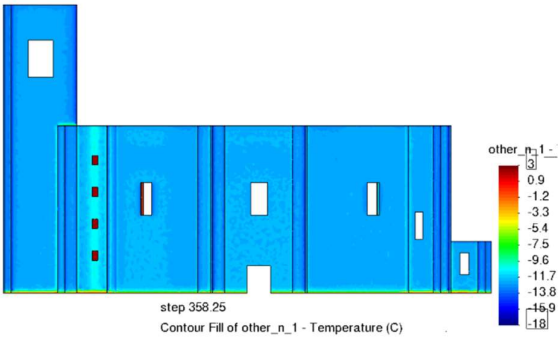

Figure 5.4 - Temperature field, time step 358.25 (winter)

The temperature distribution over the one-year cycle was monitored using seven nodes throughout the base of the windowsill on the south side of the building (Figure 5.5, Figure 5.6). Using these monitoring points, the evolution of temperatures can be tracked, and the maximum, minimum and average building states were identified.

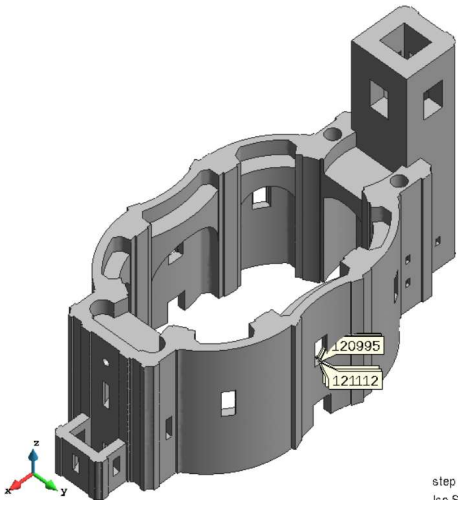

Figure 5.5 – Monitored nodes for temperature fields

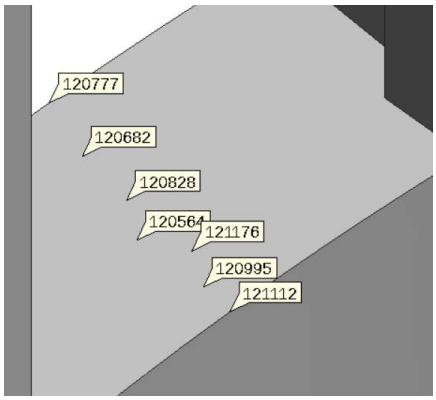

Figure 5.6 - Monitored nodes for temperature fields, close up

The results of the monitoring points are displayed in Figure 5.7, and show from results measured at the inside of the structure (node 120777) to the exterior (node 121112). In Figure 5.7, the exterior node (node 121112, dark blue) is seen to fluctuate in temperatures drastically, while the interior node (node 120777, light blue) has a slower transition of temperatures and does not experience the same degree of temperature difference in a single day.

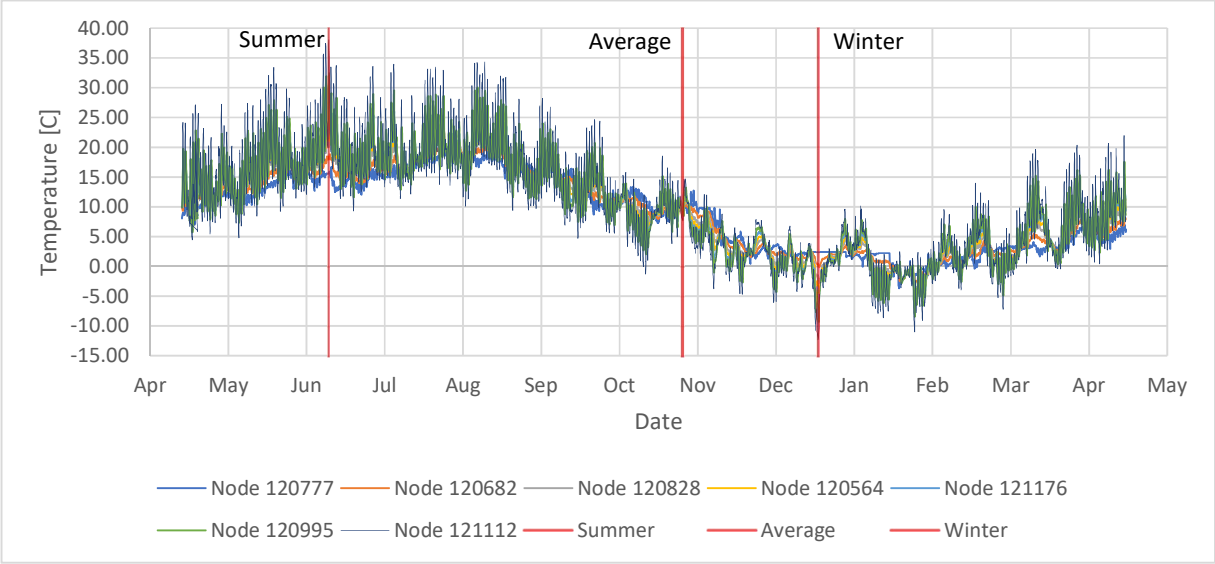

Figure 5.7 – Temperature distribution over one year cycle

Monitoring these nodes, the summer (Figure 5.8, 17/07/17, step 170.75), average (Figure 5.9, 30/10/17, step 305.25) and winter (Figure 5.10, 22/12/17, step 358.25) time steps were identified. These time steps will be used to determine the temperature differences in a one-year cycle. Temperature differences will be linearized for use in the static model to determine stress states, omitting daily temperature variations. This increase and decrease in daily temperature fluctuations can impact thermal loads on the static model, however this method was employed due to computational limits and to gain a holistic view of the yearly temperature loading on the structure.

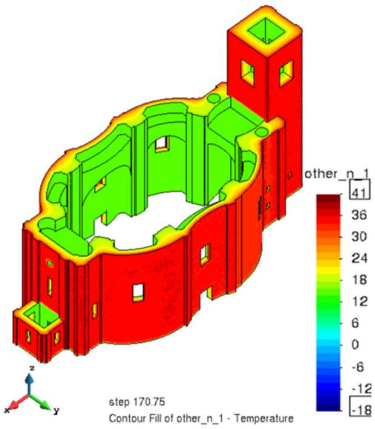

Figure 5.8 - Temperature fields on 17/07/18, step 170.75

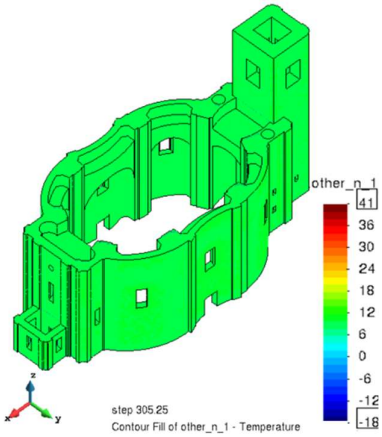

Figure 5.9 - Temperature fields on 30/10/18, step 305.25

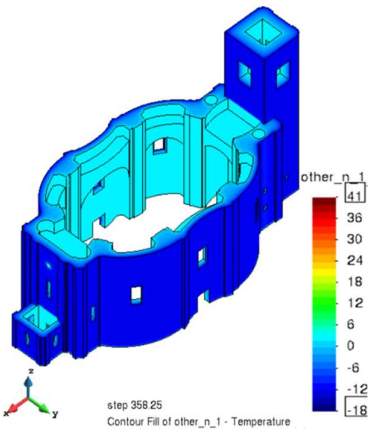

Figure 5.10 - Temperature fields on 22/12/18, step 358.25

5.5.1 Validations of Simulations against Monitoring

The results obtained from the computational model correspond well for the expected average temperatures in the Broumov region as defined by the Czech Hydrometeorological Institute (Figure 5.11). The average temperature in the Broumov region is approximately 8 °C without sun radiation effect. The average temperature found from the heat transfer analysis was 9.65 °C, as could be expected due to problem configuration and the inclusion of sun radiation effect. The temperature model from the heat transfer analysis is adequate for determining the thermal displacements of the structure.

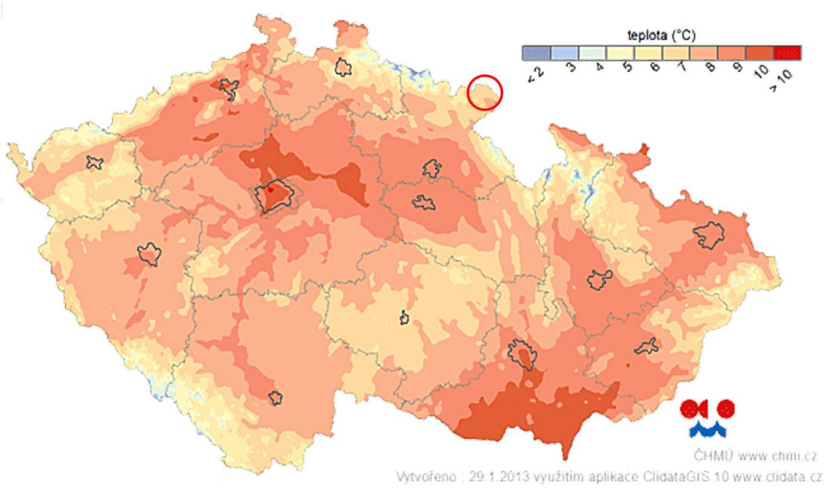

Figure 5.11 - Average temperatures in Czech Republic, Broumov Region highlighted in red circle [23]

6. THERMO-MECHANICAL ANALYSIS/ STATIC ANALYSIS

6.1 Introduction

In order to determine if the deformations and damage mechanisms observed in the structure are caused by the thermal volumetric change, the temperature loading was applied to the static model to simulate the behaviour of a one year temperature cycle. The distribution of temperatures throughout the structure that were modelled numerically over the one year period (Chapter 5) will be used as a load input for the static analysis. In this way, the 3D thermo-mechanical analysis focuses only on the masonry walls and is approached as an one-way analysis.

The static analysis was first performed using an elastic model to give a prediction of the structures behaviour, understand the current stress state and determine when the structure tends into the nonlinear range. This was followed by a non-linear numerical analysis to determine the extent of damages due to thermal strains . The non-linear analysis results were compared against site conditions and a prognosis and understanding of the possible crack nucleation was made.

6.2 Actions

The actions on the structure consist of self weight, dead load, wind load, snow load, roof live load and thermal loads.

In the analysis of historical constructions it is important not to exaggerate the loads beyond reason, as this could lead to over strengthening and an inaccurate analysis of the structure. This paper will focus on the permanent and thermal loading to predict possible damage evolutions and deformations, therefore minimal attention was paid to the statistical loading as determined by the Eurocode for variable actions such as snow, wind and live loads.

The primary actions for the mechanical analysis of the church will include only the self-weight from the masonry structure, roof live load timber roof dead loads and the thermal loading due to the temperature changes determined in the heat transfer analysis as detailed in Chapter 5.

Self-Weight

The self-weight of the masonry structure is the dominant permanent action and was applied as a body load over the entire volume, with magnitude equal to the density of the homogenized material (21.1 kN/m^3).

Roof Dead Load

The roof dead loads were applied as a pressure load distributed along the perimeter of the structure. The roof loads were taken from the previous thesis on the St. Ann Church's timber roof [10] and on similar churches in the Broumov region [8].

To determine the line load acting on the perimeter of the structure, the roof was approximated to have a constant roof pitch of 50°, and the roof dead load was assumed to be evenly distributed throughout the structure walls.

The false vault ceiling weight from the timber planks and plaster was determined to be 0.5 kN/m² acting on the projected roof area [10]. Converting the load into an equivalent pressure load acting per meter length on the perimeter of the structure was found to be 1.32kN/m².

The roof weight due to the ceramic roof tiling and timber planks was found to be 0.93 kN/m² acting as distributed load on the roof area pitched at 50° [10]. Converting the load into an equivalent pressure load acting per meter length on the perimeter of the structure was found to be 5.34kN/m².

The dead load due to self-weight of the timber trusses composed of the primary trusses, platform and beams, and is 1.45 kN/m², 1 kN/m² and 0.5 kN/m² respectively, all acting as a distributed load on the 50° roof area [8]. Converting the load into an equivalent pressure load acting per meter length on the perimeter of the structure was found to be 17kN/m².

The total pressure load acting per meter length on the perimeter of the structure due to roof dead loads was found to be 23.61kN/m. Table 6.1 includes a summary of the applied loads.

Table 6.1 - Summary of applied loads

	Weight	Applied	Equivalent load per unit length of wall
False Vault Ceiling	0.93 kN/m²	Projected	1.3 kN/m²
Roof Tile	0.5 kN/m²	Distributed	5.3 kN/m²
Timber Trusses	2.95 kN/m²	Distributed	17.0 kN/m²
Total			23.62 kN/m²

Thermal Load

The temperature fields calculated in Chapter 5 were used as the loading for the static model. Few specifics are be mentioned here, and a focus is placed on the input of temperatures as a thermal load for the static analysis.

Since the geometry and mesh were kept consistent for the heat transfer analysis and the subsequent static model, it was possible to input the temperatures into the static model regardless of the use of different software's, SIFEL and ATENA Science.

The temperature loading was applied as the temperature difference in elements between the average state and summer and winter extremes. In this way, the temperature differences were linearized and applied to the finite elements in the static model using two combinations:

- Combination A: Average temperature state to highest temperature state (summer) (Figure 6.1)
- Combination B: Average temperature state to lowest temperature state (winter) (Figure 6.2)

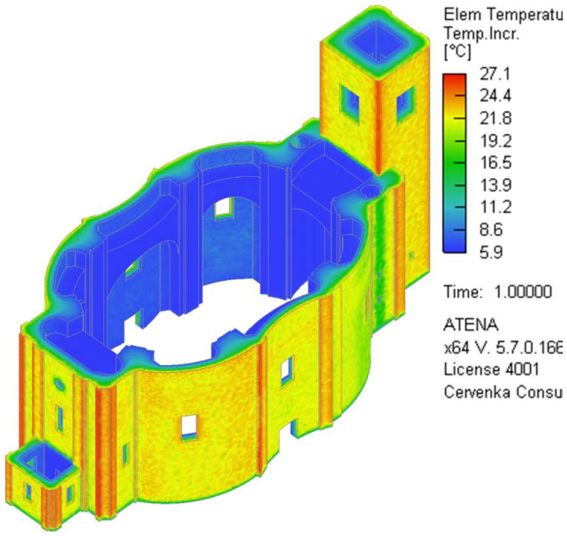

Figure 6.1 – Temp. difference, Combination A

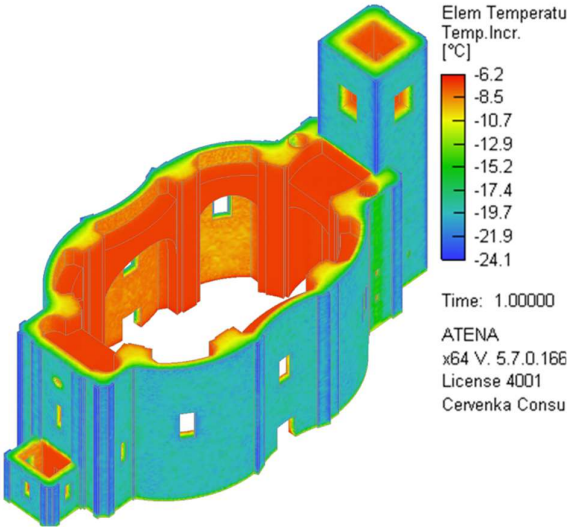

Figure 6.2 – Temp. difference, Combination B

The maximum, minimum and average temperature differences at elements for each combination were compared (Table 6.2). The regions of highest temperature difference included areas near the corners where there can be an increase in sharp elements, as well as the southern portions of the building where the structure is most influenced by sun radiation effects. The maximum temperature difference during the summer to average state (Comb. A) was 3°C higher than the winter to average state (Comb. B), the average temperature differences were similar with only a 0.3°C temperature difference. Refer to Appendix E for detailed graphical representation of applied temperature fields.

Table 6.2 - Temperature results for Combination A & B

Temperature (°C)	Combination A	Combination B
ΔT max	27.1	-24.1
ΔT min	5.89	-6.15
ΔT avg	10.7	-10.4

6.3 Boundary Conditions

For the static analysis, the structure was clamped at the base, restraining movement in x, y and z directions. All nodes were restrained to simulate fixed foundations that are capable of resisting rotation in all directions. This likely does not deviate greatly from reality, since the walls are thick (approximately 1.4 m thick for walls, 2.6 m thick for pillars) it is likely that bending at the base of the structure will be restrained from the geometrical configuration. As well, for the purposes of this paper the soil is assumed

to be stiff. Although site conditions suggest there may be areas of softer soil due to broken gutters and lack of site drainage, its effects are not considered in this thesis so that the extent of deformations and stresses from temperature loading can be determined.

6.4 Material Model

A simple elastic material model was used for the initial evaluation of the structure. This material model is simple to execute in ATENA, and is described by Young's modulus (E), and Poisson's ratio (μ), density (ρ) and thermal expansion (α) with a linear stress-strain relation.

A fracture-plastic material model with a rotating crack model was used for the nonlinear analysis. This fracture-plastic model is typically used for quasi-brittle materials (concrete, brick, etc.) and was developed in ATENA for use in concrete. The model Cementitious2 will be used for this analysis using the homogenized material parameters for masonry.

The model combines constitutive models for plastic behaviour in compression, and fracturing behaviour in tension [28]. Before cracking, it is assumed that the masonry behaves isotropically, and the principal directions of stress and strains are identical [28]. Once cracked, due to the rotating crack model, the direction of the principal stress coincides with the direction of principal strain and only two normal stress components are defined on the fracture plane [28]. This allows the principal strain axes to rotate during the analysis.

The uniaxial stress-strain law for the Cementicious2 material model is shown in Figure 6.3, with biaxial stress failure law shown in Figure 6.4.

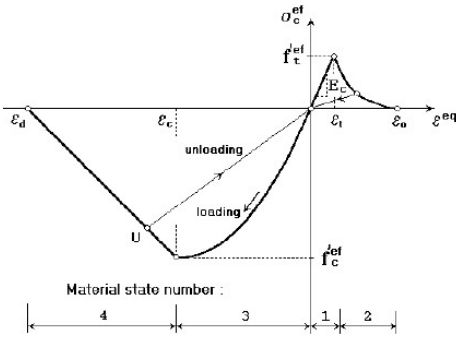

Figure 6.3 - Uniaxial stress-strain law for concrete [28]

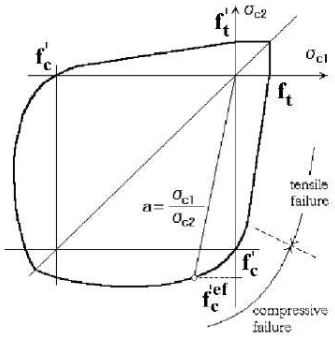

Figure 6.4 - Biaxial failure function for concrete [28]

In tension, the material is assumed to behave linearly elastic before cracking until the ultimate tensile strength is reached and cracking is initiated. The material model uses exponential softening (Figure 6.3) and is defined by the fracture energy G_f and effective tensile strength is derived from the Rankine failure

criterion (Figure 6.4). The Rankine fracture model is based on the orthotropic smeared crack formulation and crack band model [28].

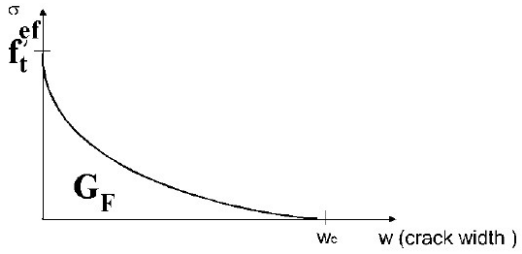

Figure 6.5 - Exponential crack opening law [28]

The material stress-strain law in compression is shown in Figure 6.6. The plasticity model uses a Menetrey-Willian failure surface shown in Figure 6.4.

Since the ascending branch of the material model in compression can range from linear to curved, distributed damage can occur before the peak stress is reached [28]. For this analysis, the onset of nonlinear behaviour, crushing, was defined as the recommended lower limit of $-f_t*2$ [28]. The localized damage after peak stress is reached is described by a linearly descending softening law (Figure 6.7). The softening curve is defined by the plastic displacement, w_d, and was left as the default 0.5 mm due to lack of experimental testing to define this parameter.

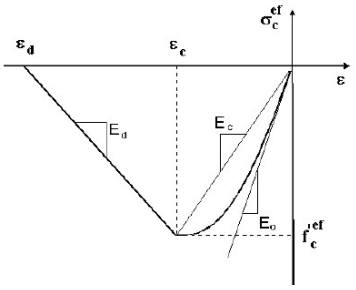

Figure 6.6 - Compressive stress-strain diagram [28]

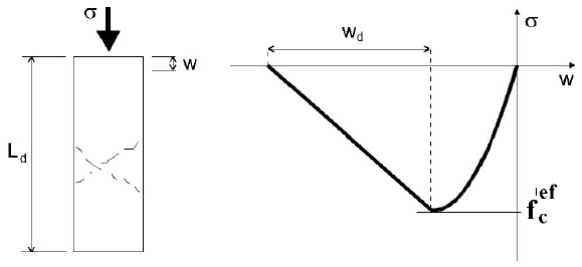

Figure 6.7 - Softening displacement law in compression [28]

6.5 Solution Methods

The method for the solution of the system of nonlinear equations implemented by ATENA is described below. The solution of the system of equations was implemented using the iterative solver, DCG and Newton-Raphson method with line search with iterations.

The iterative solver, DCG (diagonally preconditioned solution), was used for the solution of the system of equations for both the linear elastic and nonlinear analyses. An iterative solver was used since it was more efficient at solving large, well posed, 3D analyses [28].

A direct and iterative solver differ in the storage of matrices. The iterative solver stores only true non-zero elements in matrices while the direct solver also stores non-zero values below the skyline. However, when entries in matrices were originally zero, and become nonzero during factorization (Cholesky decomposition), these values are ignored due to the iterative solver [28]. The inaccuracy of the iterative solver is a trade-off for memory saving. For this problem, the use of DCG was more economical in terms of memory, RAM, and CPU time per iteration requirements compared to other solvers offered by ATENA and due to computer limitations was used.

The Newton-Raphson method was used for the solution of the nonlinear equations, with the stiffness matrix updated after each iteration. This method was used for both the elastic and nonlinear analyses. This led to fast convergence but higher iteration memory requirements. A summary of the criteria used to execute the solution of the system of nonlinear equations are shown in Table 6.3.

Table 6.3 - Summary of solution criteria for system of non-linear equations

Criteria	Elastic Analyses	Nonlinear Analyses
Relative Displacement Error	0.01	0.1
Relative Residual Error	0.01	0.1
Absolute Residual Error	0.01	0.1
Relative Energy Error	0.0001	0.001
Relative Negligible Size	0.00001	0.0001
Iteration Limit	30	30

6.6 Linear Elastic Analysis Results

The elastic analysis will be used to understand the current stress state and give a prediction of damage to determine when the structure tends into the nonlinear range. Note that the following images have different colour scales for the results. This was due to the loss of particular results that are not visible between the various results combinations when a single legend is used. Various models were prepared under the different loading conditions, and are summarized in Table 6.4.

Table 6.4 – Summary of load cases for linear elastic analysis

Load Case	Material Property	Self Weight	Roof Dead +Live Load	Thermal Load
1	Linear elastic	1		
2	Linear elastic		1	
3	Linear elastic	1	1	
4	Linear elastic			Comb. A
5	Linear elastic			Comb. B
6	Linear elastic	1	1	Comb. A
7	Linear elastic	1	1	Comb. B

Load combinations 1 and 2 were used to verify the reactions at the base of the structure against hand calculations to ensure loads were applied correctly while load combinations 3-7 will be discussed below.

6.6.1 Deformed Shape

To understand the behaviour of the structure under the combined effect of self-weight with roof dead loads and temperature loading, it is useful to first view the structure when subjected only to temperature loading (Load Case 4, 5) and compare against self weight and dead loads (Load Case 3). The maximum vertical deflection due to only self-weight and dead loads was determined to be 4.62mm, as could be expected from the structure under the given tetrahedral meshing (Figure 6.8). In Combination A (summer-average) positive temperature differences cause the structure to expand as displacements increase in x, y and z directions (Figure 6.9). On the other hand, in Combination B (winter-average), negative temperature differences cause the structure to contract and displacements reduce in all directions (Figure 6.10). When comparing Combination A and Combination B, the structure can be seen to "breathe", as it progresses through the one-year temperature cycle, expanding during summer months and contracting during winter months. In general, Load Case 4 (Comb. A) had larger displacements than in Load Case 5 (Comb. B) due to the higher difference in temperatures in Combination A (ΔT max = 27.1°C) to Combination B (ΔT max = -24.1°C).

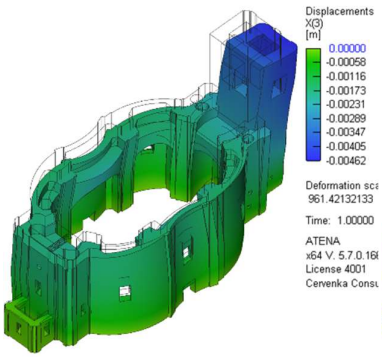

Figure 6.8 – Vertical deflection, Load Case 3

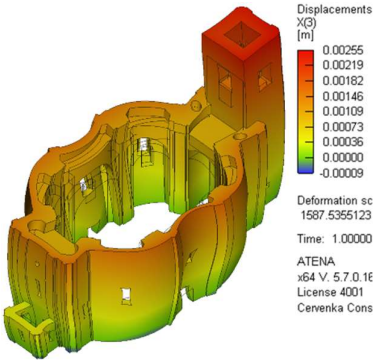

Figure 6.9 - Vertical deflection, Load Case 4

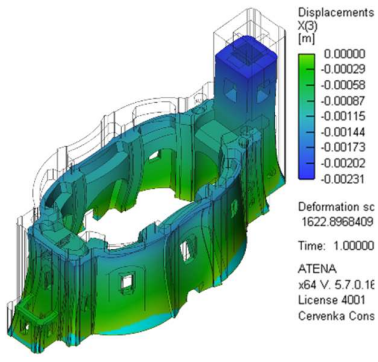

Figure 6.10 - Vertical deflection, Load Case 5

When the structure was loaded combining the effect of temperature loading with self-weight and dead loads (Load Case 6, 7), the temperature loading would in some cases counteract the displacements due to self-weight (Load Case 3). This can be observed graphically when comparing Figure 6.8 to Figure 6.11 (combined summer load) and Figure 6.12 (combined winter load). The deformed shape of the structure is seen to be restrained by the arches, which appear to add a stiffening effect to the structure and restrain horizontal movements at the top of the main nave. The roof dead loads are also able to act as a boundary condition, essentially clamping the structure, that can prevent large horizontal displacements.

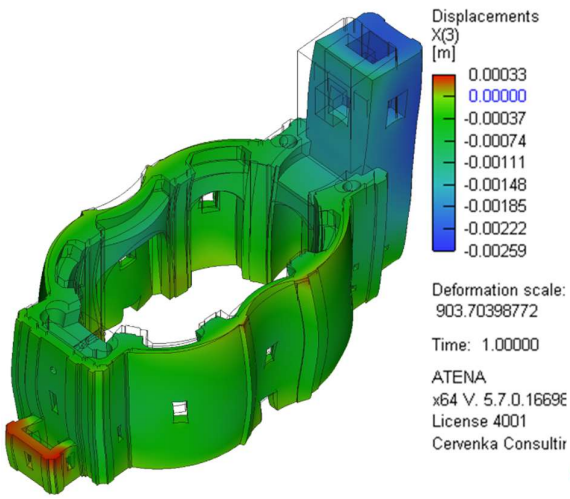

Figure 6.11 - Vertical deflection, Load Case 6

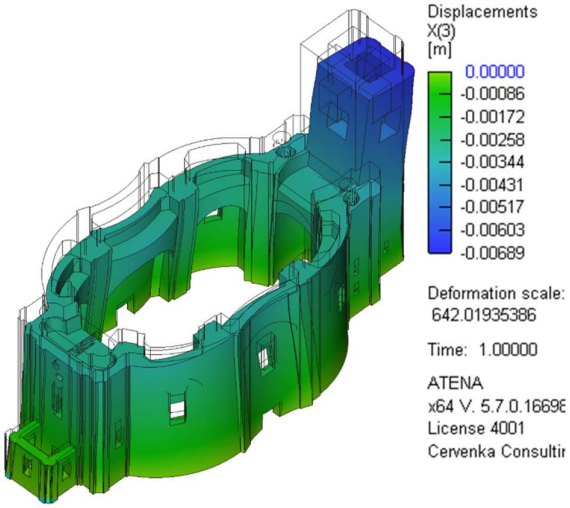

Figure 6.12 - Vertical deflection, Load Case 7

Maximum displacements in the vertical direction were 6.89 mm and occurred for Load Case 7 when dead loads were combined with winter temperature loading (Comb. B). Here, the movement caused by the contraction of the structure during the winter temperatures was in the same direction as the body load in Load Case 3 and resulted in the highest vertical displacement. On the other hand, when summer loads are combined with self-weight, the maximum vertical deflection in the structure is reduced, since the summer temperatures are counteracting the downward forces from the self-weight.

The maximum horizontal displacements are located at the top of the tower (in the negative x-axis direction). The cases when large horizontal displacements occurred in the main nave were when the curvature of the walls during self-weight and dead loads (Load Case 3) coincided with the curvature and deformed shape under Combination A and B loading (Load Cases 4 and 5).

The maximum displacement in the x-direction was 3.6 mm, located at the top of the bell tower and occurred in Load Case 6 when self-weight, dead loads and summer temperature loading (Comb. A) was applied. Here, the displacements are mostly influenced by the effect of the self-weight and roof dead loads that cause the tower to sway north since the horizontal displacement is 3.11 mm in Load Case 3. Though, it is in the combined effect with summer temperature loading that the largest displacement is seen in the tower. On the other hand, the maximum displacement in the y-direction was 2.28 mm and occurs in Load Case 7 when winter temperature loading (Comb. B) was present and caused the bulging seen at the center height of the wall on the north and south faces.

Due to the differential heating and cooling of the structure, it can be seen that displacements in the positive and negative y-directions were not equal for loading that included summer temperatures (Comb. A) (Table 6.5). This effect was not observed when winter temperatures (Comb. B) were present, due to the reduced number of active sun hours during winter days, and the reduced effect of sun radiation. A summary of the displacements under the given loading conditions are presented in Table 6.5, with

maximum and minimum values bolded. Results for y and z displacements of the structure are presented graphically in Appendix F.

Table 6.5 – Maximum and minimum displacements

Load Case	Displacement		
	x (mm)	y (mm)	z (mm)
3: SW+Roof DL	0.32	1.43	0
	-3.11	-1.42	-4.62
4: Comb. A	1.06	1.43	2.55
	-0.99	-1.37	0
5: Comb. B	0.97	1.37	0
	-0.99	-1.37	-2.31
6: SW+Roof DL+Comb.A	**1.32**	1.35	0
	-3.6	-1.3	-2.59
7: SW+Roof DL+Comb.B	0.46	**2.28**	**0**
	-2.93	**-2.28**	**-6.89**

6.6.2 Stresses

The principal stresses were compared for the different load combinations, and are summarized in Table 6.6. Understanding the current stress state in the linear elastic analysis will give a prediction of damage and will help determine when the structure tends into the nonlinear range. The sign convention in ATENA for principal stresses uses positive values to indicate tensile stress and negative values for compression.

The stress state when loaded only by self-weight and roof dead load exceeds the ultimate tensile strength (ft = 0.2 MPa), with a maximum stress of 0.307 MPa (Figure 6.13). The areas where this occurs are at the top of the staircase where the effect of the tilting tower increases tensile stresses in the thin walls and surrounding arches, as well as in the lintels of the east wall tower (Figure 6.14). The minimum principal stress, corresponding to compressive stress, in the structure under self-weight and roof dead loads was found to be -1.33 MPa, which is within an acceptable range given the building height and material. The ultimate tensile stress exceeded the tensile strength (ft = 0.2 MPa) of the material in each load case, while the compressive strength (fc= -2.9 MPa) was never exceeded.

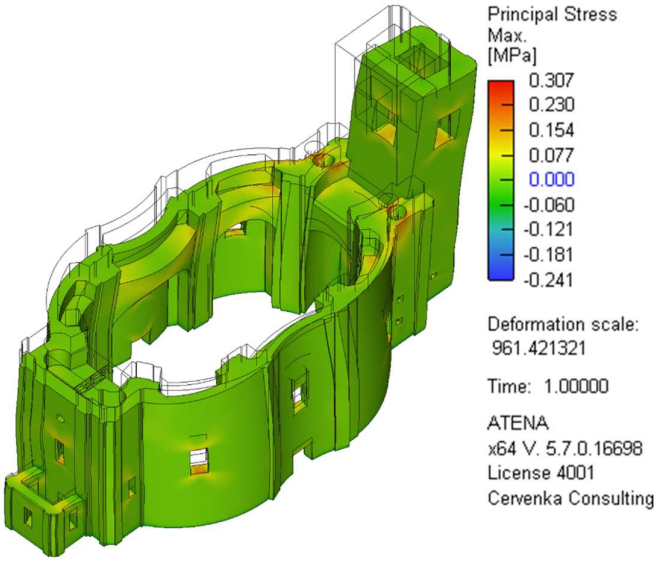

Figure 6.13 – Max. principle stress, Load Case 3

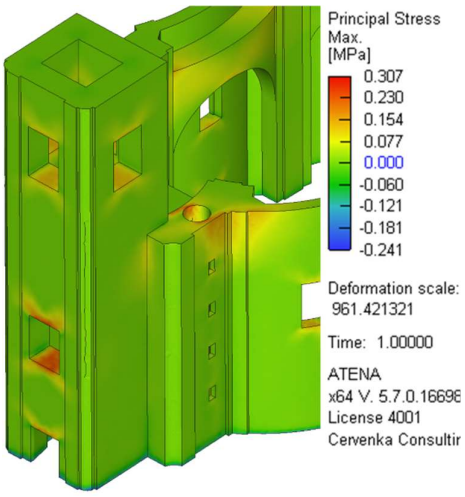

Figure 6.14 – Max. principle stress, exterior east view, Load Case 3

In Load Cases 4 and 5 (only temperature loading), the maximum tensile stresses occurred at the base of the structure, where foundations resisted uplift due to the deformed shape from temperature loading. As well, when temperature loading was present, the walls experienced a mostly uniform tensile stress along the interior (Combination A, Figure 6.15) or exterior (Combination B, Figure 6.16) surfaces due to the bending of the walls.

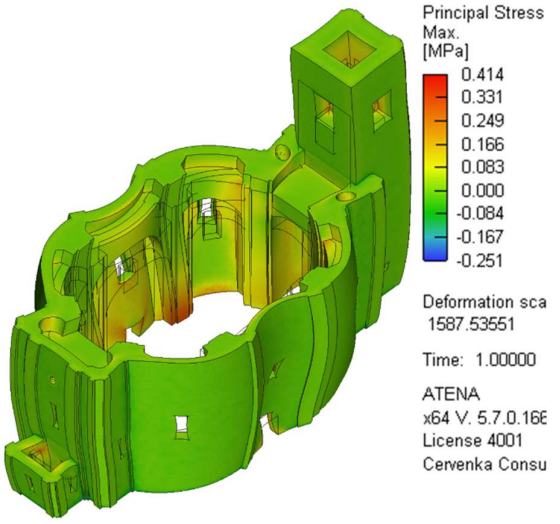

Figure 6.15 – Max. principle stress, Load Case 4

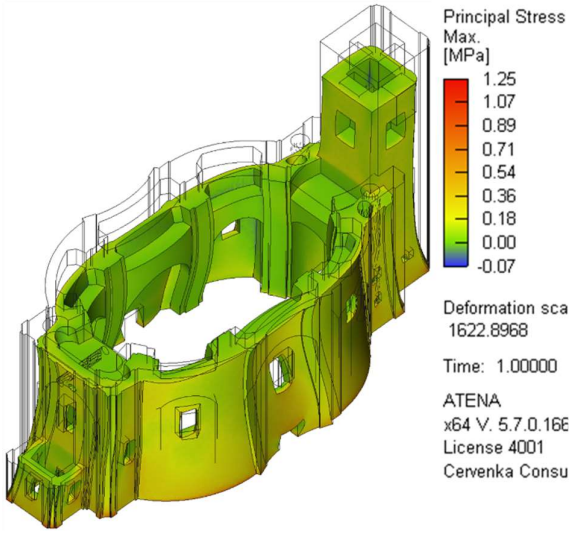

Figure 6.16 – Max. principle stress, Load Case 5

The maximum stresses were higher in Load Case 6 when the effects of summer loading (Comb. A) was combined with self-weight (Figure 6.17). This is due to the similarities in the deformed shape and curvature of the walls in bending in Load Cases 3 and 4. On the other hand, the maximum stresses decreased from Load Case 5 (winter temperatures) to Load Case 7 when the structure was loaded with winter temperatures and self-weight (Figure 6.18). This is due to the boundary effect that the roof dead load places on the structure, as well as the difference in curvature of the walls (that begin to cancel out stresses).

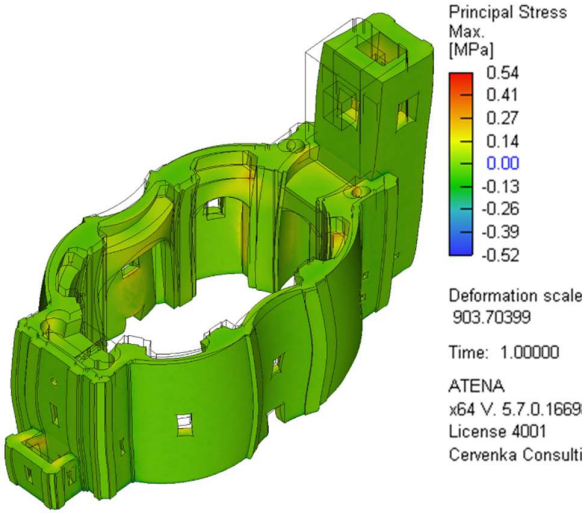

Figure 6.17 – Max. principle stress, Load Case 6

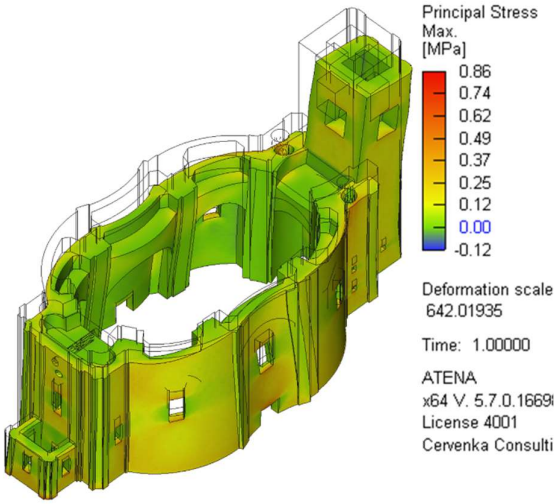

Figure 6.18 – Max. principle stress, Load Case 7

Table 6.6 – Maximum and minimum principal stresses

Load Case	Principal Stress	
	σ 1 max (MPa)	σ 2 min (MPa)
3: SW+Roof DL	0.307	0
	-0.247	-1.33
4: Comb. A	0.414	0.09
	-0.251	-1.31
5: Comb. B	1.249	0.245
	-0.07	-0.359
6: SW+Roof DL+Comb.A	0.54	0
	-0.52	-2.59
7: SW+Roof DL+Comb.B	0.86	0.11
	-0.12	-1.417

6.6.3 Strains

The sign convention in ATENA for principal strains, similar to stresses, uses positive values to indicate expansion, and negative values for contraction.

The strains in the structure were low, as could be expected for this structure due to the tetrahedral meshing that is not able to model bending well. The maximum and minimums strains measured in the structure are summarized in Table 6.7, and will be used more extensively for the comparison of the nonlinear models to the elastic models. Strain plots on the structure are not shown graphically, as the distribution pattern matches that of the stresses.

Table 6.7 – Maximum and minimum principal strains

Load Case	Principal Strain		
	Max (‰)	Mid (‰)	Min (‰)
3: SW+Roof DL	0.151	0.095	0.000
	-0.002	-0.048	-0.648
4: Comb. A	0.200	0.044	0.000
	-0.030	-0.141	-0.581
5: Comb. B	0.554	0.129	0.025
	-0.012	-0.041	-0.174
6: SW+Roof DL+Comb.A	0.269	0.094	0.010
	-0.052	-0.211	-1.160
7: SW+Roof DL+Comb.B	0.385	0.100	0.001
	-0.016	-0.058	-0.694

6.7 Non-Linear Analysis Results

The nonlinear analysis was run for Load Cases 6 and 7 of the elastic analysis, evaluating the structure's behaviour when subjected to self-weight, roof dead loads and Combination A and B temperature loading. The nonlinear analysis was only run for the two load cases due to long computation times (approximately 3 hours).

The loading was applied in steps for the nonlinear analysis. This application of thermal loads linearized the temperature differences as it was applied to the model. The models for the different loading conditions for the nonlinear analysis is summarized in Table 6.8.

Table 6.8 - Summary of load cases for nonlinear analysis

Load Case	Material Property	Self Weight	Roof Dead +Live Load	Thermal Load
8	Cementitious2	1	1	Comb. A
9	Cementitious2	1	1	Comb. B

6.7.1 Deformed Shape

The deformed shape of the structure for the nonlinear analysis behaved similarly to the elastic analysis for both load cases. A summary of the measured displacements and a comparison to the results from the elastic analysis is presented in Table 6.9. Results for x , y and z displacements of the structure are presented graphically in Appendix G.

Displacements for the nonlinear analysis for Load Case 8 under self-weight and summer loading (Comb. A) was very similar to the elastic analysis (Load Case 6). Displacements did not increase or decrease dramatically, as the largest difference was less than 1% and no difference in horizontal y-displacements were observed.

The differences in displacements were slightly larger when comparing the elastic to nonlinear analyses for Load Cases 7 and 9 with the self-weight and winter loading (Comb. B) were combined. Differences in displacements were typically below 1%, while the displacements in the horizontal x-direction increased more. Overall, the structure was seen to behave in the same manner when comparing the elastic and nonlinear analyses.

Table 6.9 – Comparison of maximum and minimum displacements

Load Case	Displacement		
	x (mm)	y (mm)	z (mm)
6: Elastic - SW+Roof DL+Comb.A	1.32	1.35	0.33
	-3.6	-1.3	-2.59
8: Nonlinear - SW+Roof DL+Comb.A	1.33	1.35	0.33
	-3.59	-1.3	-2.58
% Change	0.76%	0%	0%
% Change	0.28%	0%	0.39%
7: Elastic - SW+Roof DL+Comb.B	0.46	2.28	0
	-2.93	-2.28	-6.89
9: Nonlinear - SW+Roof DL+Comb.B	0.49	2.26	0
	-3.01	-2.28	-6.9
% Change	6.52%	0.88%	0%
% Change	2.73%	0%	0.15%

6.7.2 Comparison of Stress State (Linear to Nonlinear)

The stress distribution in the structure is very similar for the nonlinear analysis and the linear elastic analysis. A summary and comparison of stresses in the linear elastic and nonlinear analyses is presented in Table 6.10.

The minimum principal stresses, that correspond to the compressive stresses, remained the same for the elastic and nonlinear models due to the low compressive stresses that did not approach the

nonlinear range of the material. The maximum principal tensile stresses reduced as expected for both models (Figure 6.19, Figure 6.20). The maximum tensile stress was found to be 0.2 MPa, as was expected since the rotating crack model ensures the maximum principal stress does not exceed the tensile strength of the material due to additional stresses due to shear.

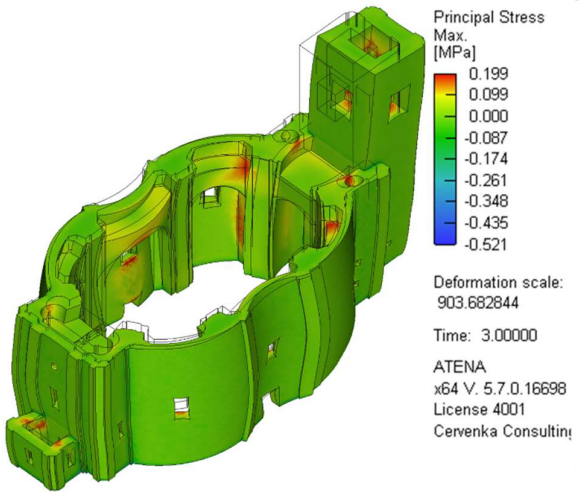

Figure 6.19 – Max. principle stress, Load Case 8

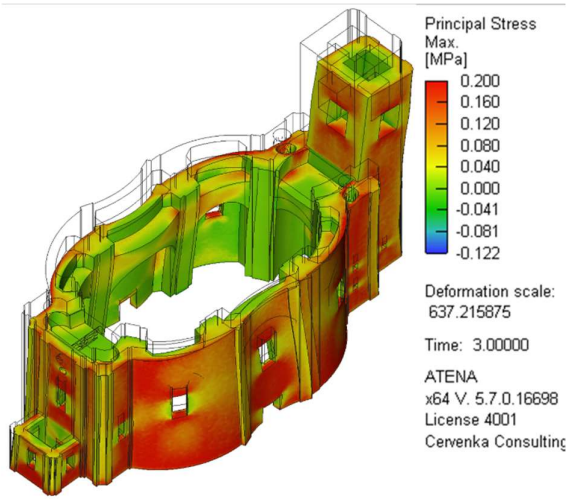

Figure 6.20 – Max. principle stress, Load Case 9

There was more of a variation in the principal stresses for the combined winter loading from the linear to nonlinear analysis due to the increase of damages from the large tensile stresses observed in the linear elastic model (0.86 MPa). The principal stresses follow the same stress pattern, though since the maximum tensile stress was reached and went from 0.86 MPa (elastic) to 0.2 MPa (nonlinear), stresses in the other principal directions varied more. Though, stresses remained comparable, as can be seen in Table 6.10.

Table 6.10 - Comparison of maximum and minimum principle stresses

Load Case	Principal Stress		
	Max (Mpa)	Mid (Mpa)	Min (Mpa)
6: Elastic - SW+Roof DL+Comb.A	0.54	0.1	0
	-0.52	-0.79	-2.59
8: Nonlinear - SW+Roof DL+Comb.A	0.199	0.09	0
	-0.521	-0.79	-2.59
% Change	63.15%	10.00%	0%
% Change	0.19%	0%	0%
7: Elastic - SW+Roof DL+Comb.B	0.86	0.35	0.11
	-0.12	-0.179	-1.417
9: Nonlinear - SW+Roof DL+Comb.B	0.2	0.194	0
	-0.122	-0.175	-1.43
% Change	76.74%	44.57%	100%
% Change	1.67%	2.23%	1%

6.7.3 Comparison of Strains (Linear to Nonlinear)

To verify the behaviour of the structure in the nonlinear range, strains were compared to the linear elastic analysis (Table 6.11). For both the summer and winter loading, principal stresses typically decreased while principal strains increased, as could be expected. This is due to the material reaching the post peak behaviour in tension once yielding occurred in select regions, and beginning to enter into the softening branch.

Though, the stress redistribution and therefore the increase in strains does not appear to affect the behaviour of the structure significantly on a global scale, since the measured displacements (Chapter 6.7.1) have no significant increase in displacements for either the summer or winter temperature loading. The behaviour of the structure in the nonlinear range was very similar to the elastic analysis. Displacements differed slightly from the linear elastic to the nonlinear analyses, and as expected stresses decreased while strains increased.

Table 6.11 - Comparison of maximum and minimum principle strains

Load Case	Principal Strain		
	Max (‰)	Mid (‰)	Min (‰)
6: Elastic - SW+Roof	0.269	0.0935	0.01
DL+Comb.A	-0.052	-0.2105	-1.16
8: Nonlinear - SW+Roof	0.484	0.093	0
DL+Comb.A	-0.052	-0.21	-1.16
% Change	79.93%	0.53%	100.00%
% Change	0%	0.24%	0%
7: Elastic - SW+Roof	0.385	0.1	0.001
DL+Comb.B	-0.016	-0.058	-0.694
9: Nonlinear - SW+Roof	0.624	0.101	0
DL+Comb.B	-0.016	-0.057	-0.698
% Change	62.08%	1.00%	100.00%
% Change	0%	1.72%	0.58%

6.7.4 Damages

To understand the extent of damages, crack width, quantity and location were evaluated and displayed graphically on the structure and compared with the tensile stress state. In the following figures, cracks are denoted in black.

Load Case 8 with self weight and summer temperature loading (Comb. A) had fewer damages than Load Case 9 with winter temperature loading (Comb. B). This was expected due to the higher tensile stresses observed during the linear elastic winter temperature loading.

The high concentrations of stress above window openings in both cases (Figure 6.28, Figure 6.35) are an overestimation, since in reality these windows are arched. It can be expected that the arches above

the openings would act mostly in compression, and thus these tensile stresses would be reduced and cracks would be avoided, or of little concern. As well, high concentrations of stresses and subsequent cracks in lintels above door frames are typically not a cause for concern, since a cracked lintel can act as a jack arch, and an alternate load path can be formed, creating a relieving arch without causing further damage or cracking.

6.7.4.1 Damages for Load Case 8 (Combined Summer Loading)

Damages during the summer temperature loading were found exclusively on the interior faces of the structure due to the deformed shape and stress pattern as shown in Figure 6.21. The location and magnitude of cracks corresponded with the peak tensile stresses. An overview of the crack localization can be seen in Figure 6.22. The maximum crack width for this load case was found to be 0.066 mm.

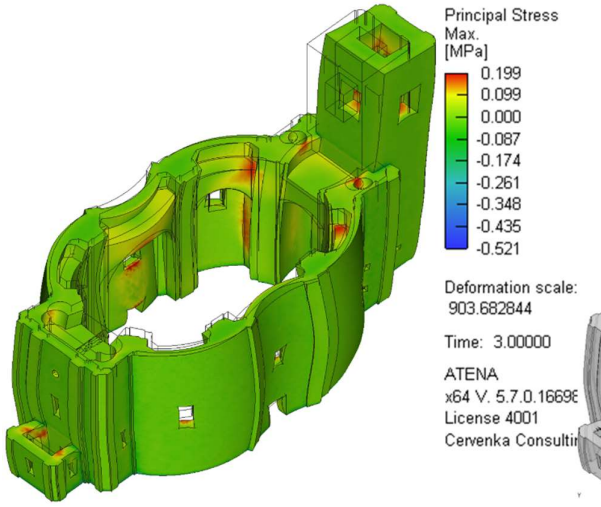

Figure 6.21 – Max. principle stress, Load Case 8

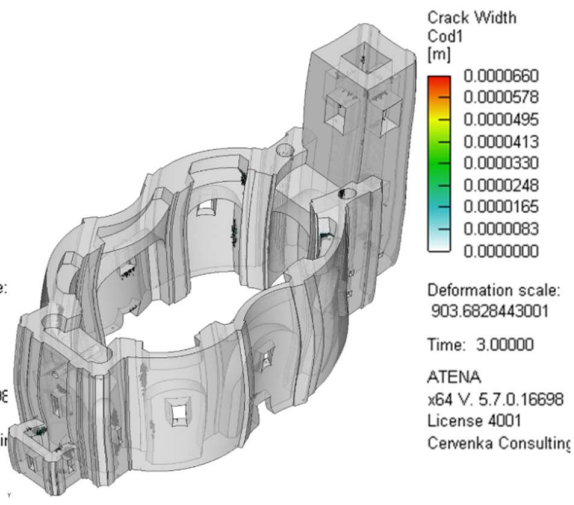

Figure 6.22 – Crack width, Load Case 8

The outward movement of the tower causes stresses (Figure 6.23) and subsequent cracking to concentrate at the top of the thinly walled staircase on the inside wall (Figure 6.24, A) and at the intersection of the arch and main nave (Figure 6.24, B). This movement combined with the effect of the summer temperature loading and the bulging walls causes stresses and cracks to concentrate along the side of the pillar (Figure 6.24, B). The effect of the bulging walls and crack concentration can also be observed graphically in Figures 6.25 and 6.26. Crack width varies from 0.03 mm to 0.05 mm in this area.

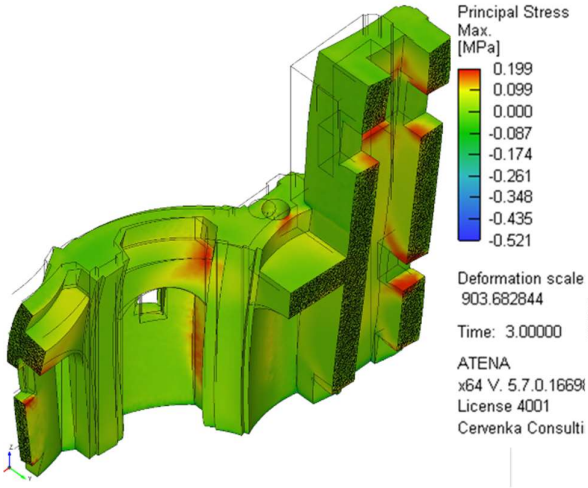

Figure 6.23 – Max. principle stress, NE section, Load Case 8

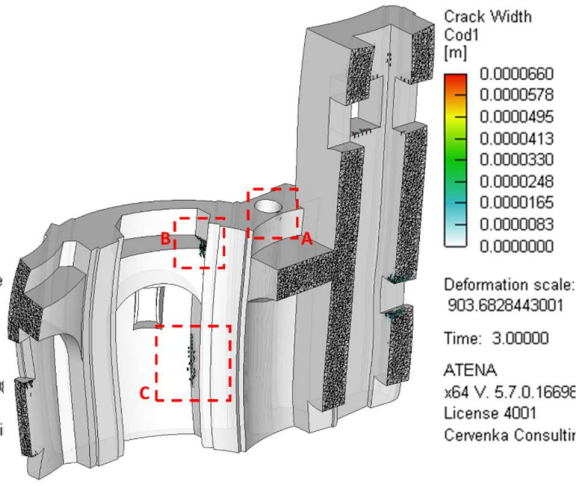

Figure 6.24 - Crack width, NE section, Load Case 8

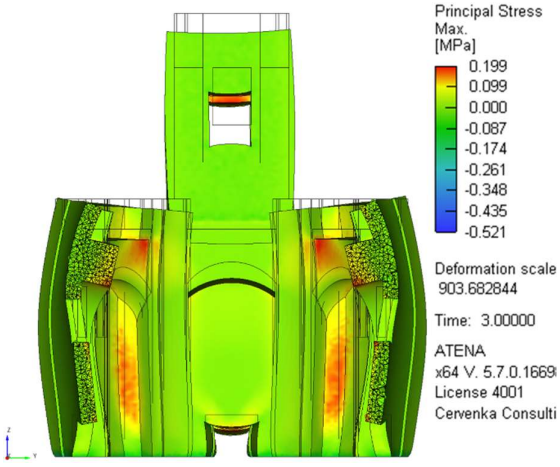

Figure 6.25 – Max. principle stress, east section, Load Case 8

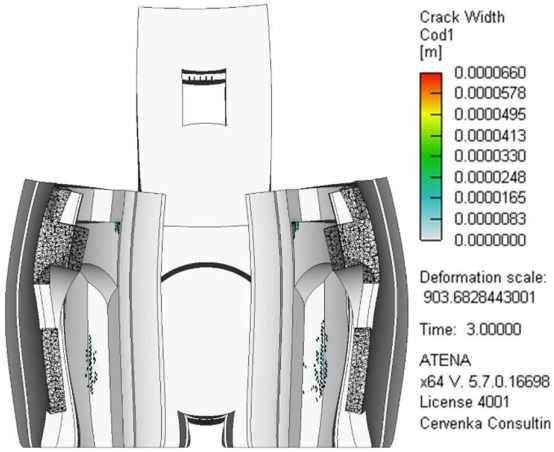

Figure 6.26 - Crack width, east section, Load Case 8

The church cross-section (east-west) is depicted in Figures 6.78 and 6.28 for the maximum stresses and crack locations where the un-deformed shape (black outline) to the deformed shape can be compared. The increased curvature of the walls due to the self-weight and summer temperature loading caused the concentration of tensile stresses in areas that experienced increased bending. It was common to observe an increase in tensile stresses and subsequently cracks surrounding openings as previously discussed.

The stresses and cracks seen in the middle bay of the main nave between both openings and west end of the church between both openings is due to the walls that bulge inwards (Figure 6.27, Figure 6.28, A). As the temperature loading causes the pillars to deform, the arches can be seen to distort, and an

increase in tensile stress is seen in the arch crown (Figure 6.27). The confining effect that the arches provide on the structure can also be seen in Figure 6.27, as the deformed structure appears restrained at the elevation of the arches, and since the arches appear to resist additional tensile loading.

The deformed shape of the walls also contributes to the high stresses surrounding the opening at the west end of the church. The differential movement of the outer wall compared to the interior surface of the pillar caused an increase in shear stresses that caused the formation and high concentration of cracks in the area surrounding the window opening (Figure 6.28, B). The cracks concentrated in this area range in width from 0.0165 mm to 0.066 mm.

Areas of high tensile stress and subsequent crack formation were also noticed near the corners of the openings of the sacristy, closest to the main nave (Figure 6.27). These areas experienced high tensile stress due to the sacristy expanding (summer loading), while the main nave of the church restrained the movement of the sacristy through the increase of vertical forces (-z) from self weight (Figure 6.28,C). The cracks in this area range in width from 0.033 mm to 0.066 mm.

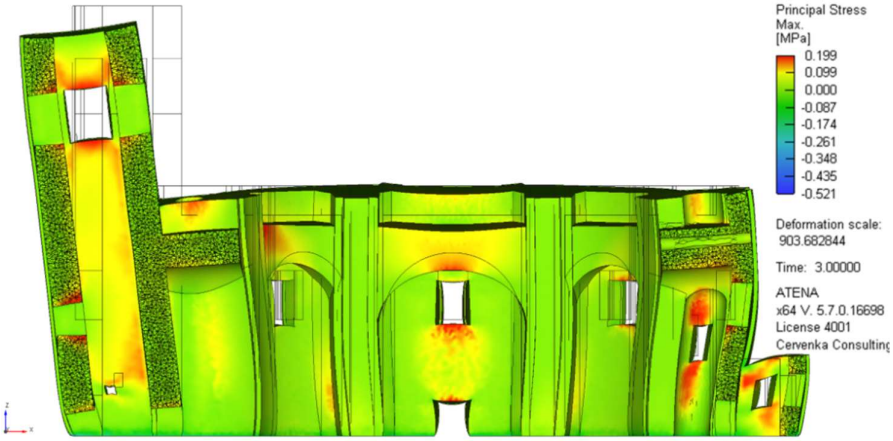

Figure 6.27 – Max. principle stress, south section, Load Case 8

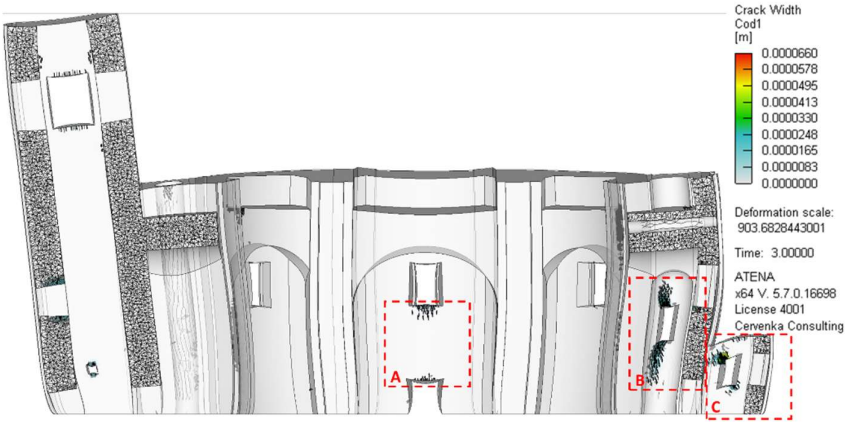

Figure 6.28 - Crack width, south section, Load Case 8

6.7.4.2 Damages for Load Case 9 (Combined Winter Loading)

The combined self weight with winter temperature loading caused more areas to reach the peak tensile stress and caused more damages on the structure. These damages are concentrated on the exterior of the structure, though small regions with hairline cracks can be seen on the interior. The stresses and damages for the deformed structure are shown in Figures 6.29 and 6.30 respectively. The maximum crack width for this load case was found to be 0.142 mm.

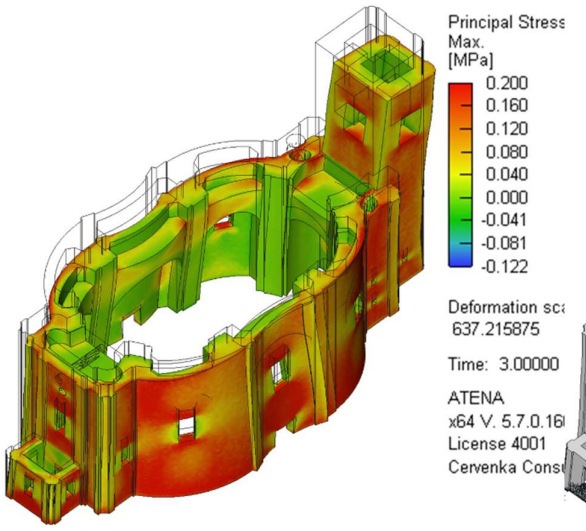

Figure 6.29 – Max. principle stress, Load Case 9

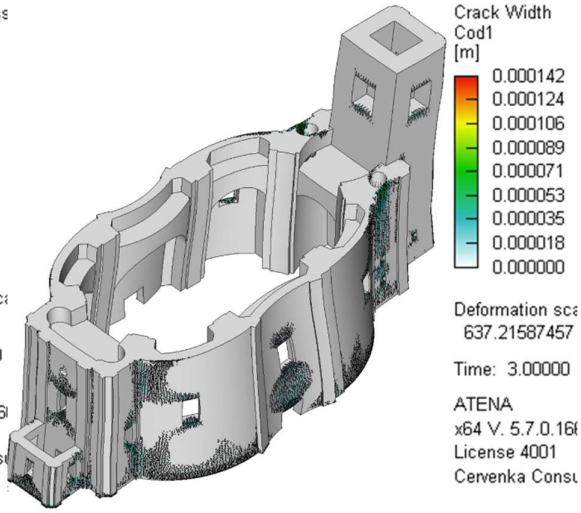

Figure 6.30 - Crack width, Load Case 9

Similarly, to Load Case 8, an area of high tensile stress is at the top of the structure where the main nave meets the staircase in the exterior wall of the staircase (Figure 6.31, Figure 6.32, A). The stresses in this area are likely due to the combination of the outwards movement of the bell tower and the increase in stress due to temperature. Crack width reaches a maximum in this area, ranging in width from 0.035 mm to 0.142 mm.

The areas where the maximum tensile strength was reached for the combined self weight and winter temperature loading were commonly observed surrounding the openings on the exterior surfaces of the structure (Figure 6.31). This is due to the inward movement of the walls that cause stresses to concentrate around the openings, with a particularly high concentration of cracks at the middle of the main nave between the window and door openings (Figure 6.32, B).

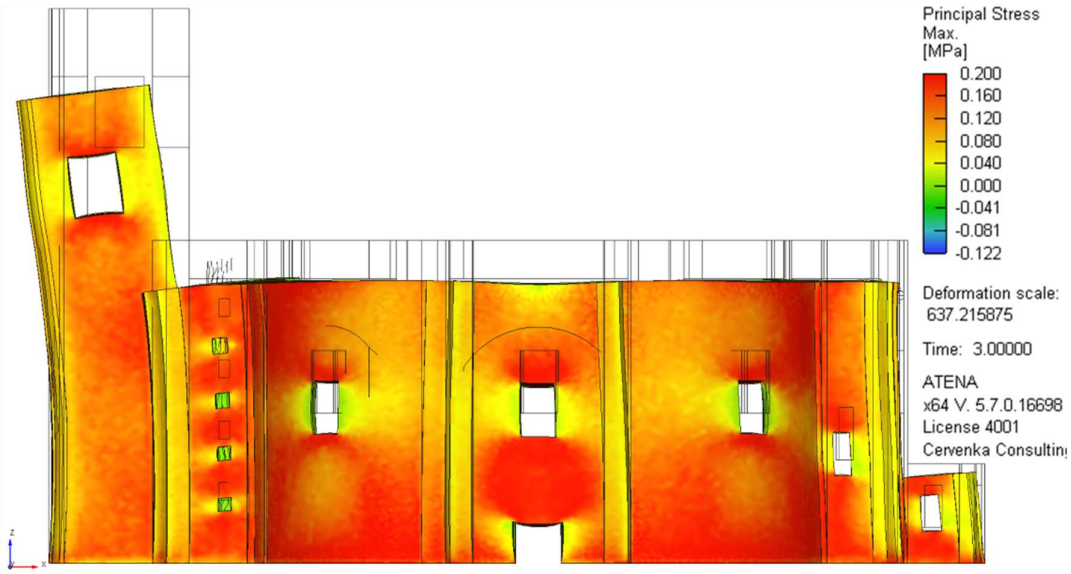

Figure 6.31 – Max. principle stress, north elevation, Load Case 9

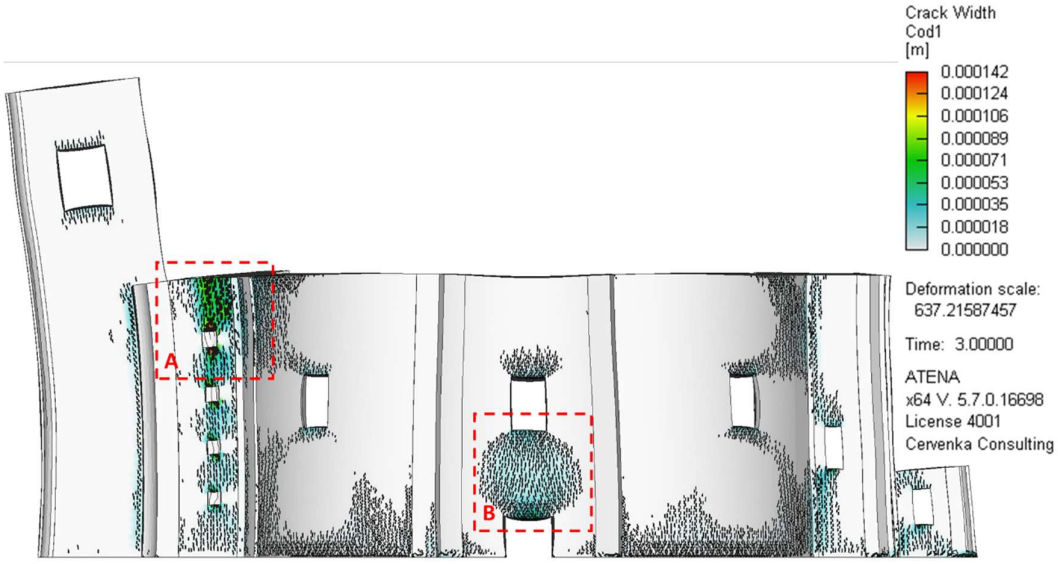

Figure 6.32 - Crack width, north elevation, Load Case 9

The area of highest tensile stress for Load Case 9 with winter temperature loads was at the foundation level of the sacristy, located along the outside perimeter (Figure 6.33). The winter loading causes the structure to contract, and in turn the foundations experience uplift. This effect is most dramatic at the sacristy, since the vertical loads (self weight, roof dead loads) are not enough to counteract the uplift in the foundations (Figure 6.34, A). Cracks in this region vary from 0.053 mm to 0.142 mm.

Uplift in the foundations can also be observed along the perimeter of the main, but with lower magnitude since it is able to be counteracted by the higher self weight. The effect of uplift through the main nave

contributes to the high concentration of cracks on the exterior of the structure near the ground level (Figure 6.34, B). Cracks in this region typically vary around 0.018 mm.

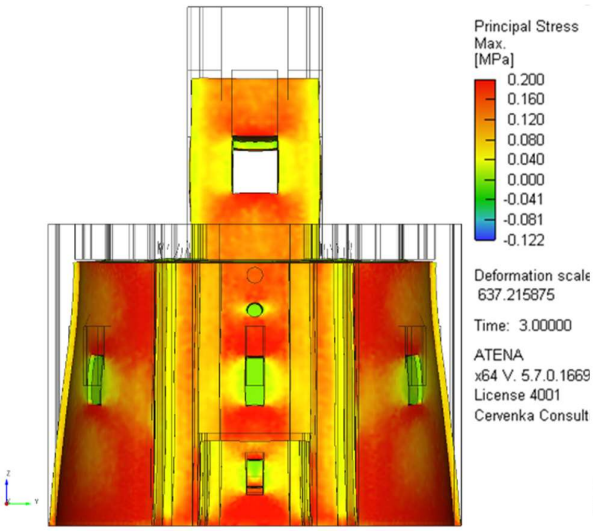

Figure 6.33 – Max. principle stress, west elevation, Load Case 9

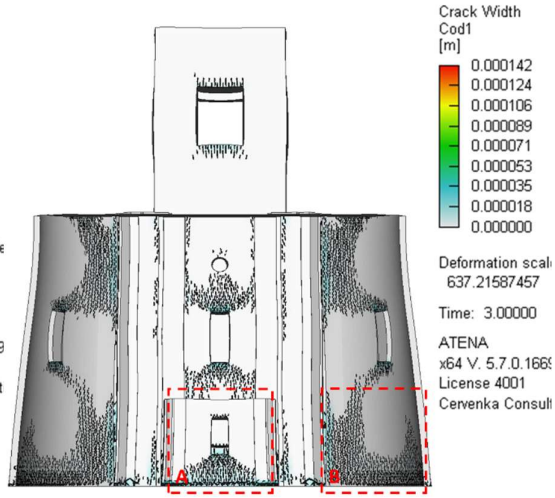

Figure 6.34 - Crack width, west elevation, Load Case 9

Areas of high stress and crack concentrations can be seen clearly in the lintels of the tower (Figure 6.35, Figure 6.36). The effect of the higher temperature differences localized on the exterior layer of the structure are a large contributor for the increase in tensile stresses and thus crack propagation. This can be seen more clearly in Figure 6.37, (inside facing east towards tower) where there is a clear boundary along the height of the tower between the interior and exterior of the structure. The contraction of the outer layer of the building, combined with the curvature of the walls, is enough to increase the number of cracks when compared to the summer loading model.

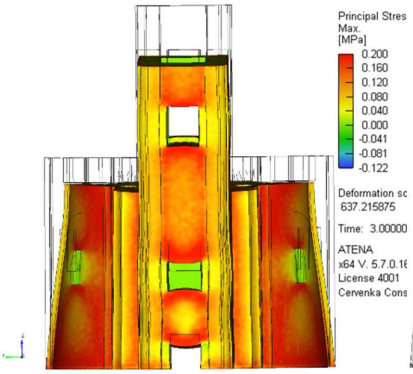

Figure 6.35 – Max. principle stress, east elevation, Load Case 9

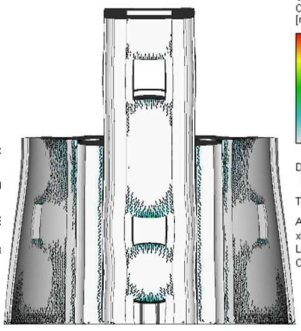

Figure 6.36 - Crack width Load, east elevation, Case 9

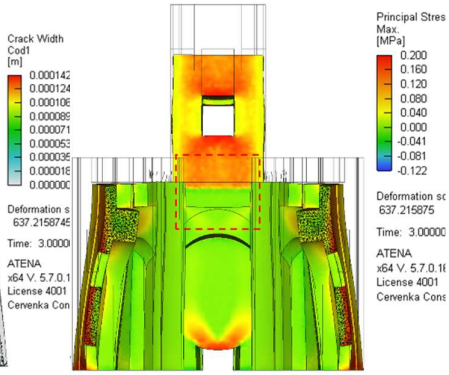

Figure 6.37 – Max. principle stress, east section,Load Case 9

6.7.5 Comparison with Current Damage State

To better understand the damages seen in the numerical analyses, and to correlate the computed damages to observed results, a crack filter was applied to remove microscopic cracks and to display cracks greater than 0.05 mm, since it is the smallest crack a person can see with their naked eyes. The damages found can be compared to those observed directly on the structure (refer to Appendix A for detailed damage maps).

Minimal cracks remained after filtering was applied for Load Case 8, (self weight with summer temperature loading) as can be seen in Figures 6.38 and Figure 6.39. The largest cracks were 0.066 mm and were located above the openings at the west end of the structure near the dome openings (Figure 6.39, A) and in the sacristy windows (Figure 6.39, B). Cracks surrounding this opening were also seen in the real structure (Figure 6.40) with the cracks extending from the openings on either side of the nave, going through the small dome and connecting at the top (Figure 6.41). It is possible that these damages in the real structure are related to the temperature loading, though differential settlement can also have contributed to the movement of the outer west wall relative to the pillars and thus formed these damages.

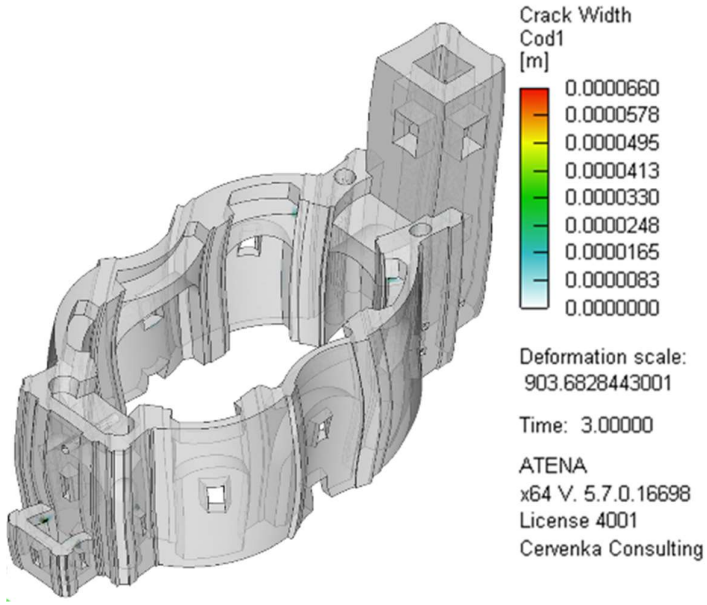

Figure 6.38 – Filtered crack width, Load Case 8

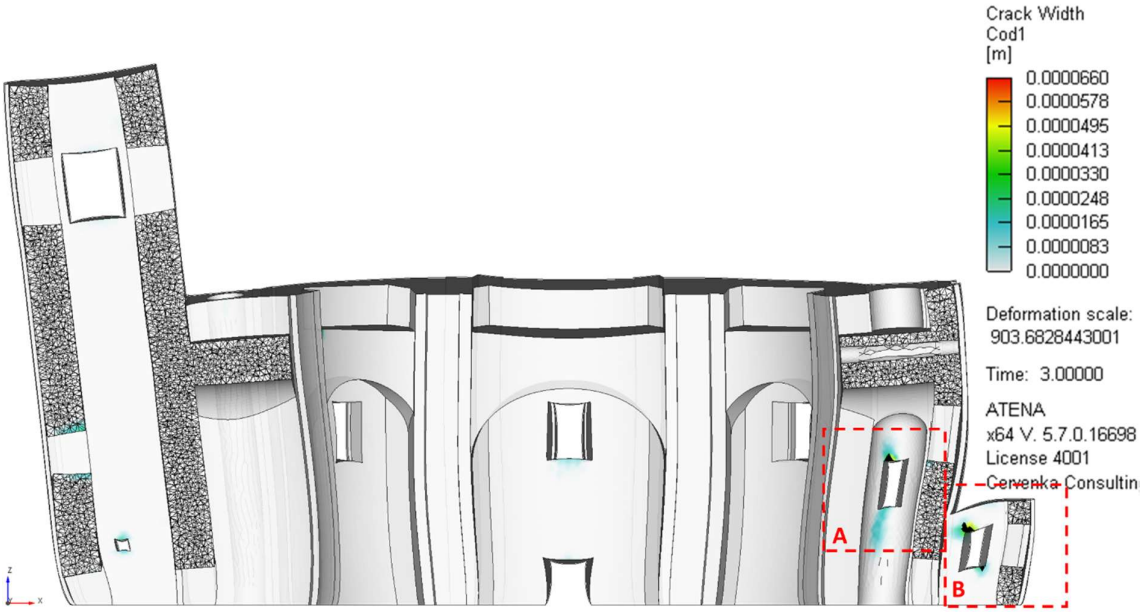

Figure 6.39 – Filtered crack width, south section, Load Case 8

Figure 6.40 - Longitudinal crack in arch barrel, extending towards opening

Figure 6.41 - Extension of longitudinal crack into openings

A larger number of cracks remained after filtering was applied for Load Case 9 (self weight with winter temperature loading) when compared to Load Case 8 (summer temperature loads), as can be seen in Figure 6.42 and Figure 6.43. A location where cracks remain in the winter model once filtering was applied are concentrated at the thin exterior wall of the staircase that restrains the outer movement of the bell tower (Figure 6.43, A). However, cracks in this region were not observed on the real structure but rather on the bell tower (Figure 6.44). These cracks are assumed to be from the use of the church bells or the movement of the tower under self weight, however results suggest that temperature loading, and weathering may have exacerbated this movement.

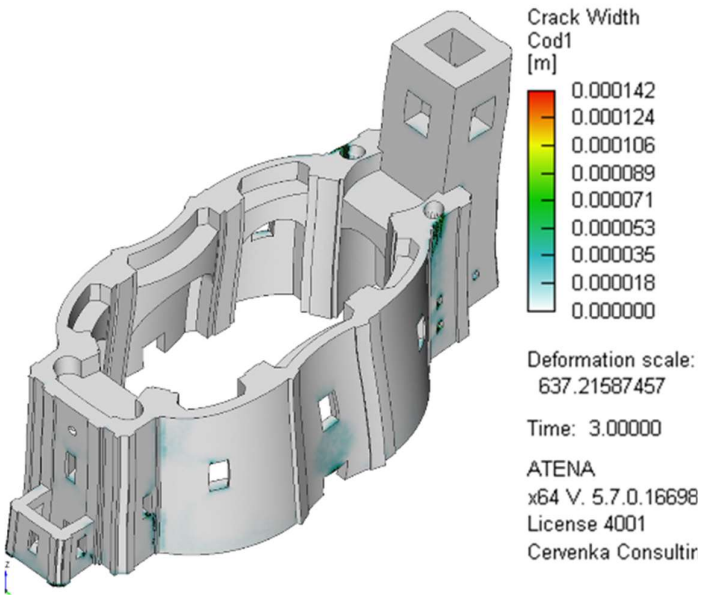

Figure 6.42 – Filtered crack width, Load Case 9

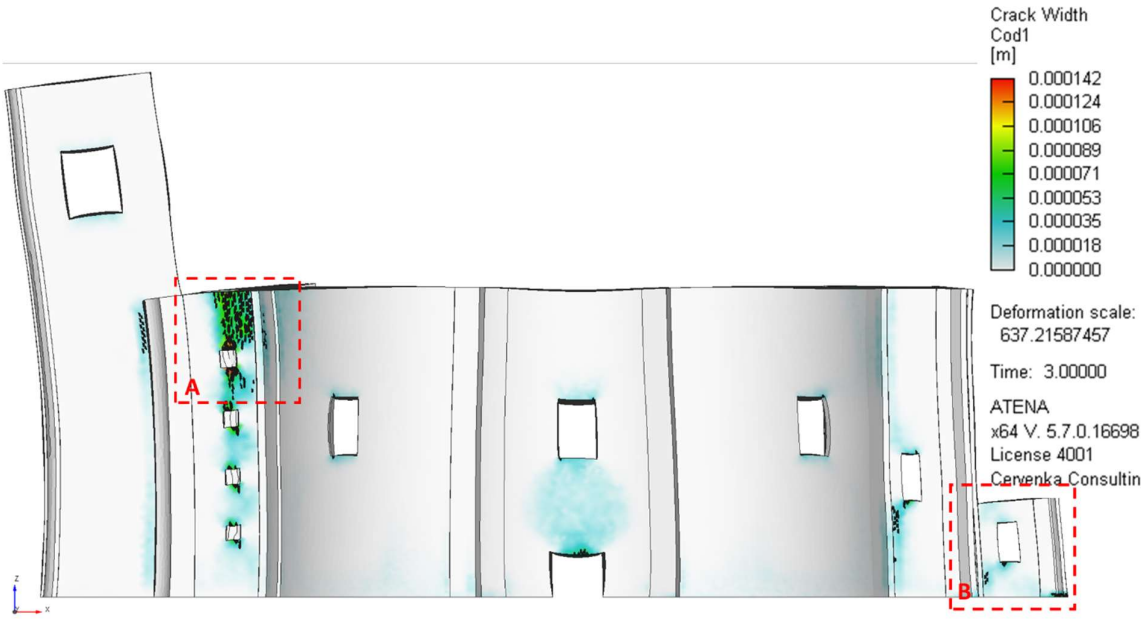

Figure 6.43 – Filtered crack width, north elevation, Load Case 9

Figure 6.44 - Cracks surrounding bell tower opening

In the numerical model, a concentration of cracks was observed at the foundation level of the sacristy where the foundations experienced the most uplift (Figure 6.43, B, C). In the present situation, along the exterior of the main nave (Figure 6.45) and sacristy (Figure 6.46) it was common to see the lowest course of foundation blocks detached from the structure with a sequence of cracks forming a relieving arch extending from the foundation to window opening (Figure 6.47). As previously discussed this area has issues in drainage problems that could have affected neighbouring soil and caused differential settlements, however the detachment could have been worsened from winter temperature loading that added uplift to the foundations.

Figure 6.45 - Stone detachment, north wall

Figure 6.46 – Stone detachment in found., sacristy

Figure 6.47 - Cracks on sacristy wall above opening

This page is left blank on purpose.

7. CONCLUSIONS

The uncoupled thermo-mechanical analysis of the St. Ann Church carried out using the 3D numerical model in SIFEL and ATENA has shown that the structure is periodically under temperature strain.

The distribution of temperatures throughout the structure were modelled for a one year period. The temperature extremes for summer, winter and average states were identified. This allowed the application of temperature differences from the average state to summer and winter extremes to be input as a load into the static model to simulate the effect of climatic loading impact.

The behaviour of the structure in the nonlinear range was very similar to the elastic analysis. Displacements differed slightly from the linear elastic to the nonlinear analyses, and as expected stresses decreased while strains increased. The additional movement from the increased temperature strains and nonlinear material behaviour did not cause significant deformations to the structure. Since the structure reached its tensile strength in localized areas, cracks formed. These cracks were very thin, and did not cause any significant stress redistribution or alternate load paths. The damages presented in the structure did not cause global nor local collapse in the numerical model. The results from the numerical model were compared to observations made on the current state of the structure. The majority of damages on the structure appear to be a result of improper maintenance and weathering. Climatic temperature loading appears to exacerbate deterioration mechanisms and damages on the real structure. Crack widths determined from the numerical model were relatively small, and should not be a cause for concern due to the highly robust nature of the structure. The impact of climatic temperature loading is low, and poses minimal risk to the structural integrity.

Simplifications in the modelling approaches may have caused results to differ slightly from the behaviour of the real structure. To improve results in the thermal analysis, the boundary conditions imposed by the insulation provided by the glass windows could be accounted for. As well, the effect of daily temperature fluctuations could be evaluated due to the high temperature variations observed in a 24hr period which could increase temperature loads. The thermal material properties were assumed to be constant, regardless of varying properties due to temperature or moisture fluctuations. Since there was a high moisture content observed in the church interior and exterior north walls, considering the effects of moisture on material properties could help to refine the results. Nonetheless, the thermal analysis behaved as predicted under the microclimate of the Broumov region and adequately modelled a one-year temperature cycle to be used for the subsequent static analysis.

To improve the results from the static analyses, instead of linearizing the application of the temperature fields, the loading could be input as a sequence of temperature steps more closely representing the real nature of the climate for the analysed time period. Since this was not possible due to software and computer limitations it was not implemented for this model. However, for the purposes of this study the numerical model appears to accurately model the structure, gaining an understanding of the current

stress state. The damage mechanisms due to temperature loading were able to be identified and compared to the real behaviour of the structure.

7.1 Recommendations

To reduce the risk of damages due to climatic temperature loading, and to control the present damages, the following recommendations are made.

Installation of monitoring system

To better understand the behaviour of the structure, a monitoring system including the installation of inclinometers, temperature and humidity monitors is recommended. These should be installed in the bell tower, where the biaxial tilting of the tower can be observed to determine if movements are active, and to what extent this is from climatic loading. A monitoring system is also recommended to be installed in the west end of the main nave and in the sacristy where the largest amounts of damages are detected, and the largest impact of temperature loads are seen. To determine if cracks are active, crack monitors are recommended for the transversal and longitudinal cracks in the arch at the west end, and in the cracks that extend from the arch into the domes to either side. This would reduce any levels of uncertainty due damages, and the severity of deformations can be further evaluated.

To have a clearer understanding of the thermal fluctuations per season and areas of high vulnerability due to large temperature loads, thermal photography is recommended to be included in a periodic monitoring and maintenance plan.

Control of high moisture levels

It is recommended to control high moisture levels in the walls that not only lead to deterioration issues but can negatively affect climatic loading. This could be accomplished through adequate natural ventilation periodically that can be done with opening windows and fan arrangement to help dry the masonry from the interior. The building would also benefit from a proper gutter drainage system and flashings to deter water from the masonry structure, which would reduce the amount of water infiltration, reducing the risk of freeze-thaw cycles. Furthermore, reducing the amount of water runoff on the structure diminishes the amount of erosion, lessens mortar loss and avoids any issues in differential soil settlements.

Repointing masonry and restoring façades

It is recommended to repoint the masonry walls with a compatible lime mortar and to restore the plaster of the façades to ensure a more tight envelope. The lime mortar and plaster should be compatible with the visual and physical material properties. The flexibility and low strength of the lime mortar will ensure compatibility with the structure when the wall undergoes contraction and expansion (breathing of the wall) due to the cyclic temperature changes. Re-sealing the building with the lime plaster would provide a better building envelope and ensure a more gradual transition of temperatures by reducing air

infiltration/exfiltration to control moisture and heat. This would also restore the mechanical properties of the wall and provide additional resistance to weathering actions. This should be done in combination with a periodic maintenance plan to avoid the degraded state the church is in today and to avoid preventable damages due to weathering and climatic loads.

This page is left blank on purpose.

8. REFERENCES

[1] Nature Conservation Agency of the Czech Republic, “Protected Landscape Areas of the Czech Republic,” Nature Conservation Agency of the Czech Republic, Prague, 2015.

[2] G. Facelli. E Burgetovà, “Structural survey of St. Jacob's Church and comparison with St. Ann's Church (Broumov group of Churches),” Czech Technical University in Prague, Prague, 2014.

[3] E. Semotanová, R. Šimùnek. E Chodějovská, Historical Landscapes in Bohemia - Regions of Třeboň, Broumov and Praha, vol. 61, P. Martin Holý, Ed., Prague: Opera Instituti Historici Pragae, 2015.

[4] History, “Thirty Years' War,” 2009. [Online]. Available: https://www.history.com/topics/reformation/thirty-years-war. [Accessed 2019].

[5] Czech Ministry of Foreign Affairs, “The history of architecture,” 01 01 2010. [Online]. Available: http://www.czech.cz/en/66608-the-history-of-architecture.

[6] J. T. Kotalik, P. Sùva, B. Prokop, Broumovská Skupina Kostelů, Modrý Anděl, 2007.

[7] P. Kuklik. P Gajjar, “Nonlinear numerical evaluation of the wall bearing capacity and the structure stability of the St. Ann Church from the Broumov Group of Churches,” Czech Technical University in Prague, Prague, 2018.

[8] P. Kuklik, J. Scacco, “Nonlinear numerical evaluation of the bearing capacity and the structure stability of the St. Jacob Church from the Broumov Group of Churches,” Czech Technical University in Prague, Prague, 2018.

[9] M. Snehota, O Peleška, “Assessment of the Water Transport in a Soil Masonry System of the Baroque Church of St. Anna in Vižňov,” Czech Technical University in Prague, Prague, 2018.

[10] P. Kuklik, P Duinker, “First and second order analysis of St. Ann’s church timber roof in Vižňov, CZR,” Czech Technical University in Prague, Prague, 2009.

[11] Yandex.Traffic LLC, “Weather forecast in Broumov in April,” 30 04 2019. [Online]. Available: https://yandex.com/weather/broumov/month/april.

[12] J. Maděra, V. Pommer, R. Černý, J Kočí, “Analysis of the Frost-Induced Damage of Building Enclosures on the Territory of the Czech Republic,” *Advances in Materials Science and Engineering,* vol. 2018, no. 1, p. 12, 2018.

[13] E. Holtanová, T. Halenka, J. Kalvová, M Belda, “Climate classification revisited: from Köppen to Trewartha,” *Climate Research,* vol. 59, pp. 1-13, 2014.

[14] GiD, “Reference Manual,” GiD, 2019.

[15] KJ. Bathe, D. J. Payen, “Improved stresses for the 4-node tetrahedral element,” *Computers and Structures,* vol. 89, no. 2011, 2011.

[16] T. Nelson, R. Rauch, E Wang, “Back to Elements - Tetrahedra vs. Hexahedra,” CAD-FEM GmbH, Munich, 2004.

[17] “Automatica - Department of Information Engineering,” 2007. [Online]. Available: http://automatica.dei.unipd.it/public/Schenato/PSC/2010_2011/gruppo4-Building_termo_identification/IdentificazioneTermodinamica20062007/eggpsc/Simulatore%20termico/AFEM.Ch15.pdf. [Accessed February 2019].

[18] E. Vejmelková, R. Černý, D Koňáková, “Thermal properties of selected sandstones,” *Advances in Modern Mechanical Engineering,* Vols. -, no. -, pp. 100-104, -.

[19] L. M Angelillo, “Masonry behaviour and modelling,” 2014.

[20] SIFEL Group, “Introduction,” 2015. [Online]. Available: http://mech.fsv.cvut.cz/~sifel/. [Accessed 2019].

[21] J. Grunewald, Documentation of the Numerical Simulation Program DIM3.1, J. G. Geert Houvenaghel, Ed., Dresden: Institute of Building Climatology, 2000.

[22] J. Kruis. M. Šejnoha, T. Koudelka, T Krejčí, “Numerical analysis of coupled heat and moisture transport in masonry,” *Computers & Mathematics with Applications,* vol. 74, no. 1, pp. 229-248, 2017.

[23] Czech Hydrometeorological Institute, “Historická data - meteorologie a klimatologie,” 2019. [Online]. Available: http://portal.chmi.cz/historicka-data/pocasi/zakladni-informace.

[24] J. Máca, P. Fajman, P Beran, “Temperature Effects on one bay of St. Vitus' Cathedral,” Czech Technical University in Prague, Prague, 2010.

[25] J. Máca, P Beran, “The influence of temperature on the deformation of columns in the nave of the Saint Vitus Cathedral at the Prague Castle,” *Journal of Building Appraisal,* vol. 2, no. 4, p. 10, 2007.

[26] Bendheim, “What is the difference between long wave and short wave radiation?,” 01 02 2019. [Online]. Available: https://bendheim.com/faq/long-short-wave-infrared-radiation/.

[27] A. Lavine, F. Incropera, D. Dewitt, T Bergman, Fundamentals of Heat and Mass Transfer, L. Ratts, Ed., Jefferson City: John Wiley & Sons, Inc., 2011.

[28] L. Jendele, J. Červenka, V Červenka, “ATENA Program Documentation Part 1 - Theory,” Červenka Consulting s.r.o., Prague, 2018.

[29] International Council on Monuments and Sites (ICOMOS) - International Scientific Committee for Stone (ISCS), Illustrated Glossary on Stone Deterioration Patterns, ICOMOS, Ed., Paris: Monuments and Sites, 2008.

[30] W. Brekelmans, M. Geers, I Özdemir, “Computational homogenization for heat conduction in heterogeneous solids,” *Internation Journal for Numerical Methods in Engineering,* vol. 73, no. -, pp. 185-204, 2007.

[31] J. Vorel, T. Krejčí, M. Sejnoha, J. Sejnoha, J Sykora, “Analysis of coupled heat and moisture transfer in masonry structure,” *Materials and Structures,* vol. Materials and Structures, no. -, p. 24, October 2008.

[32] T. Krejčí, M Toesca, “Thermo-Mechanical Analysis of Charles Bridge in Prague,” Czech Technical University in Prague, Prague, 2014.

[33] P. Beran, J. Máca, P Fajman, “Influence of Temperature Changes on the Vladislav Hall Vault,” *Acta Geodynamica et Geomaterialia,* vol. 7, no. 2, p. 6, 2010.

[34] E. Susanti, P Kuklik, “Numerical bearing capacity of the All Saints' Church walls in Broumov, CR,” Czech Technical University in Prague, Prague, 2017.

[35] J. Mikolášková, T. Altman, Š Beneš, “ATENA Program Documentation Part 12 - User's Manual for ATENA Studio (Version 5.6.0),” Červenka Consulting s.r.o., Prague, 2018.

[36] J. Červenka, Z. Janda, D. Pryl, V Červenka, “ATENA Program Documentation Part 8 - User's Manual for ATENA-GiD Interface,” Červenka Consulting, s.r.o, Prague, 2019.

APPENDIX A – DAMAGE MAPS

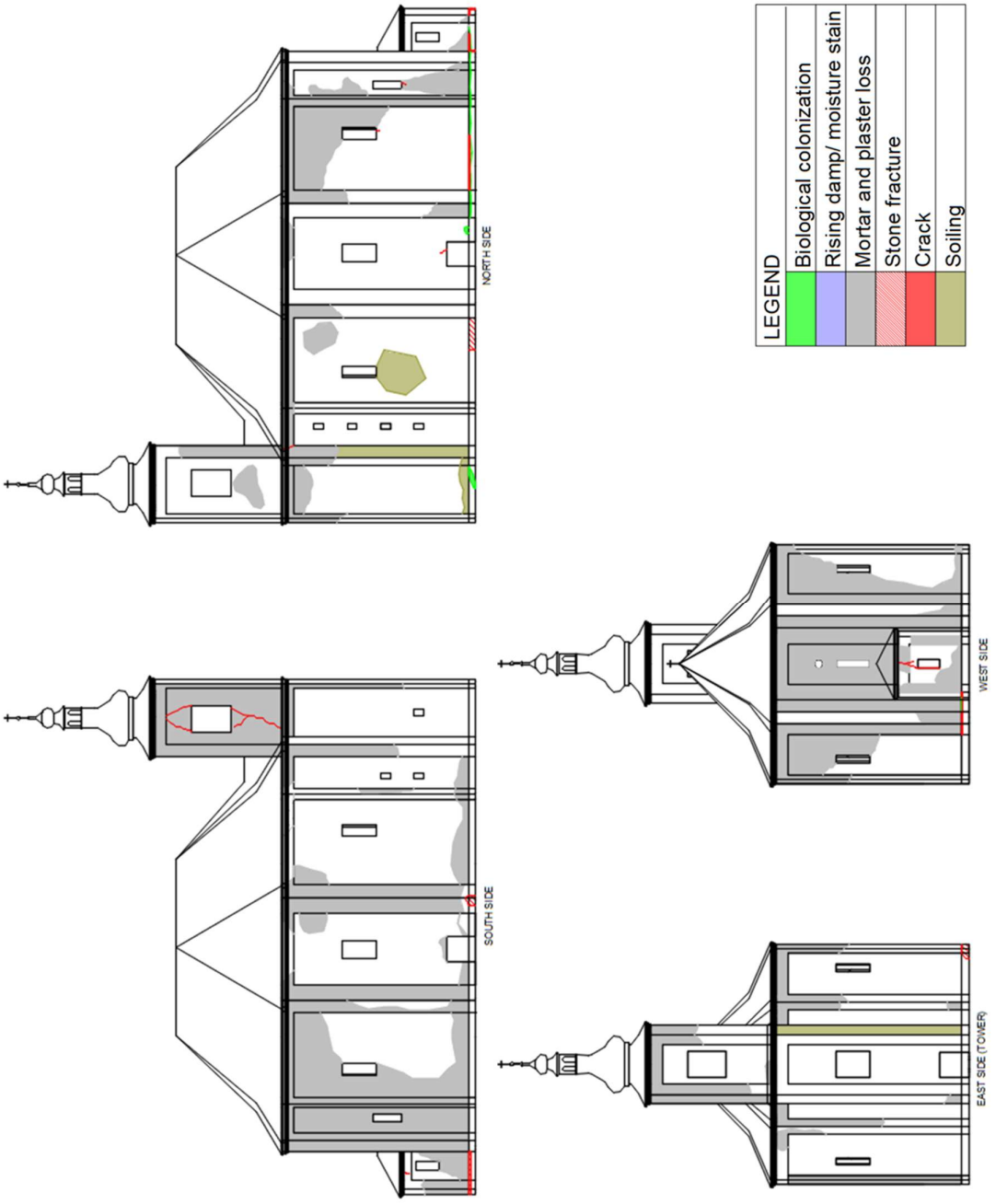

Figure A.1 - Damage map, exterior

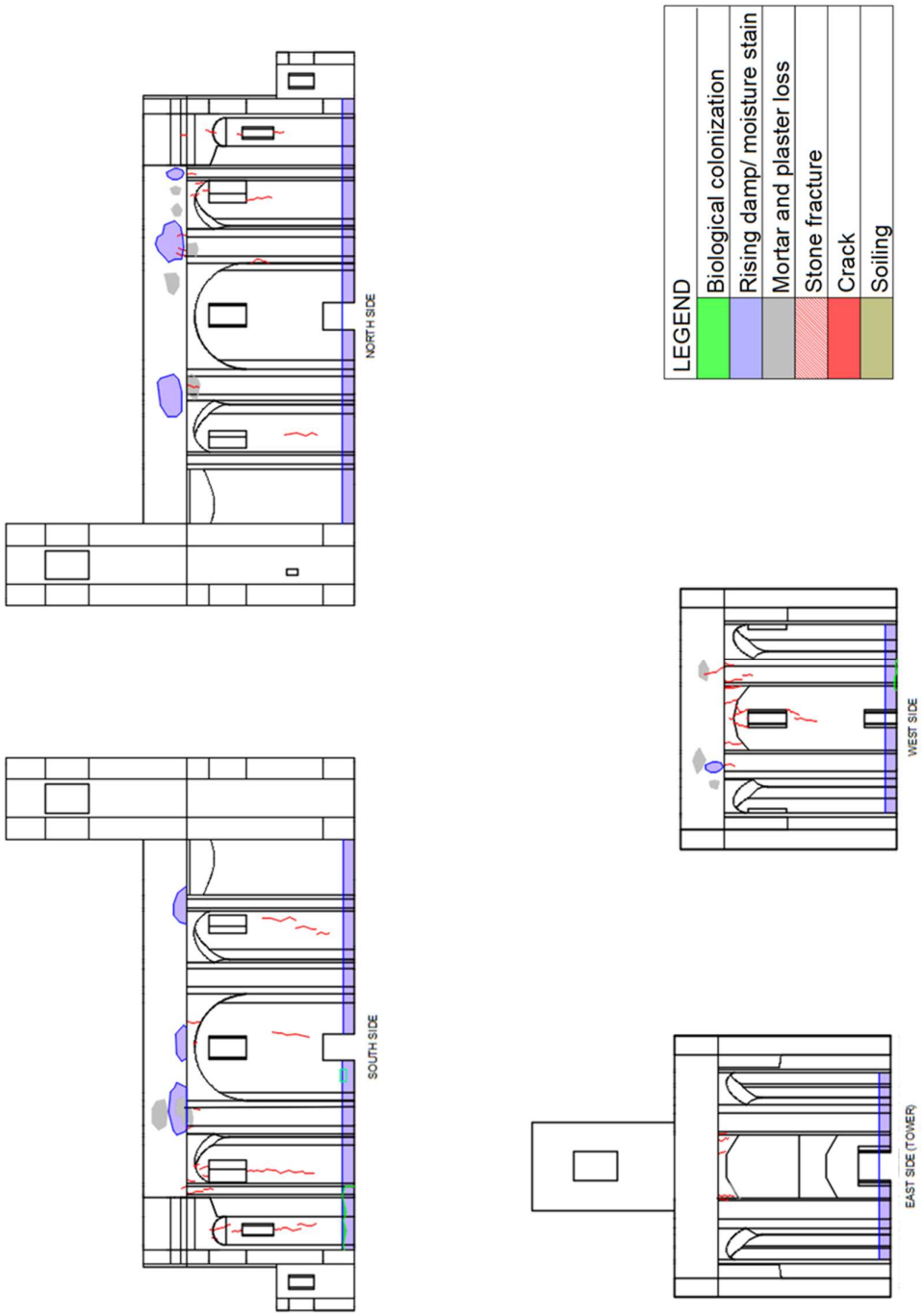

Figure A.2 - Damage map, interior

APPENDIX B – DATA MONITORING

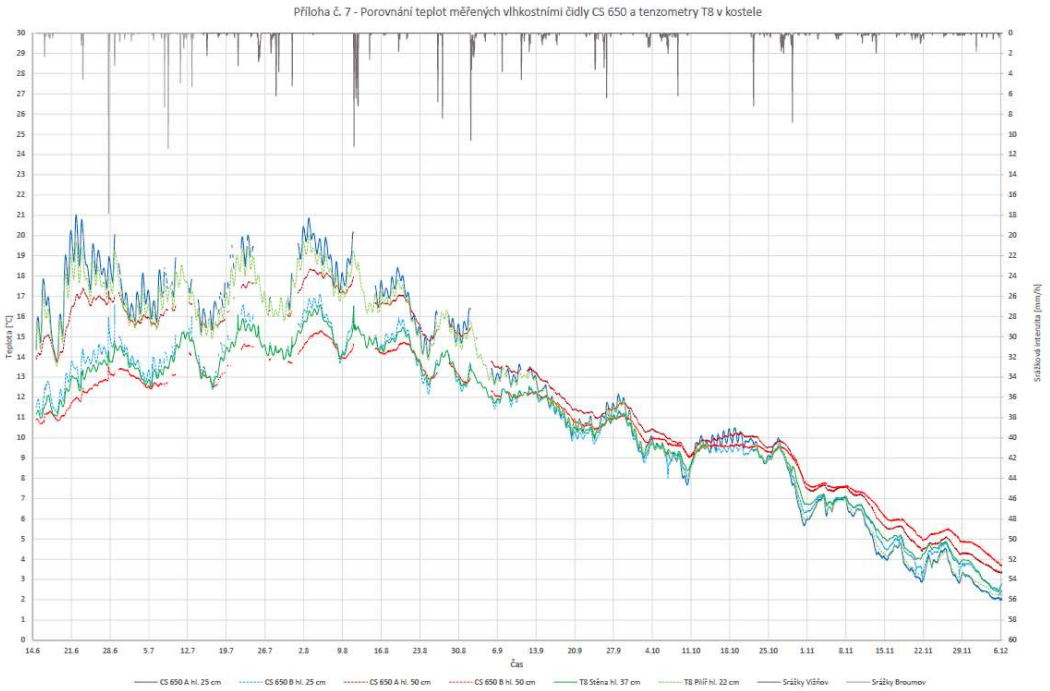

Figure B.1 - Temperature readings at strain gauges in soil [9]

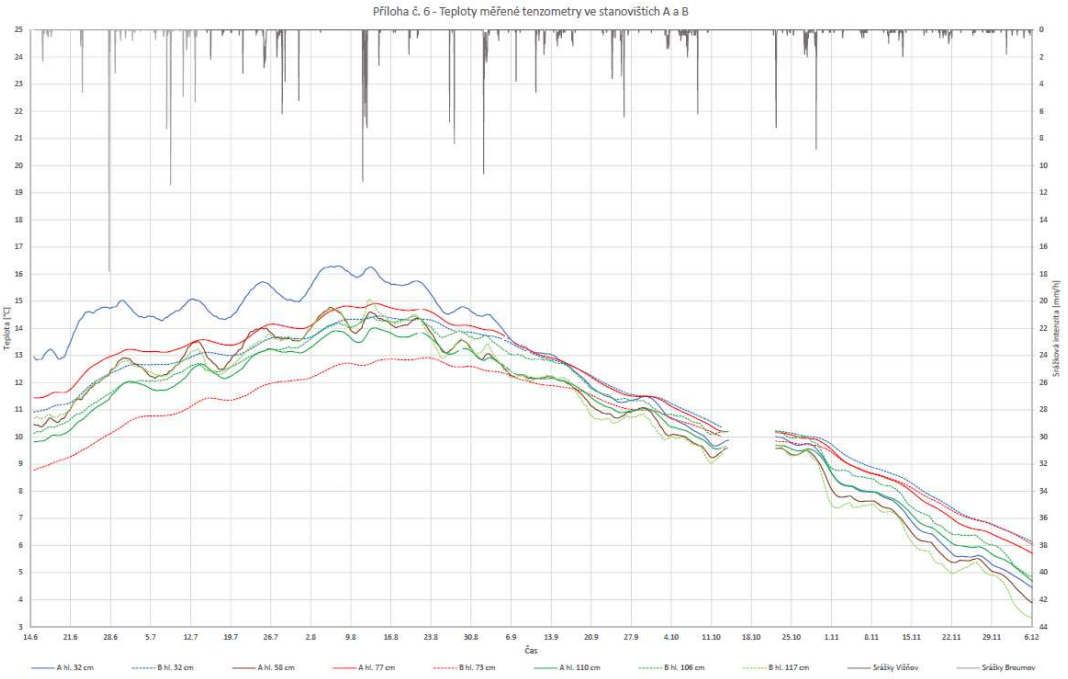

Figure B.2 - Temperature readings at strain gauges inside church, north wall [9]

APPENDIX C – INPUT TEMPERATURE GRAPHS

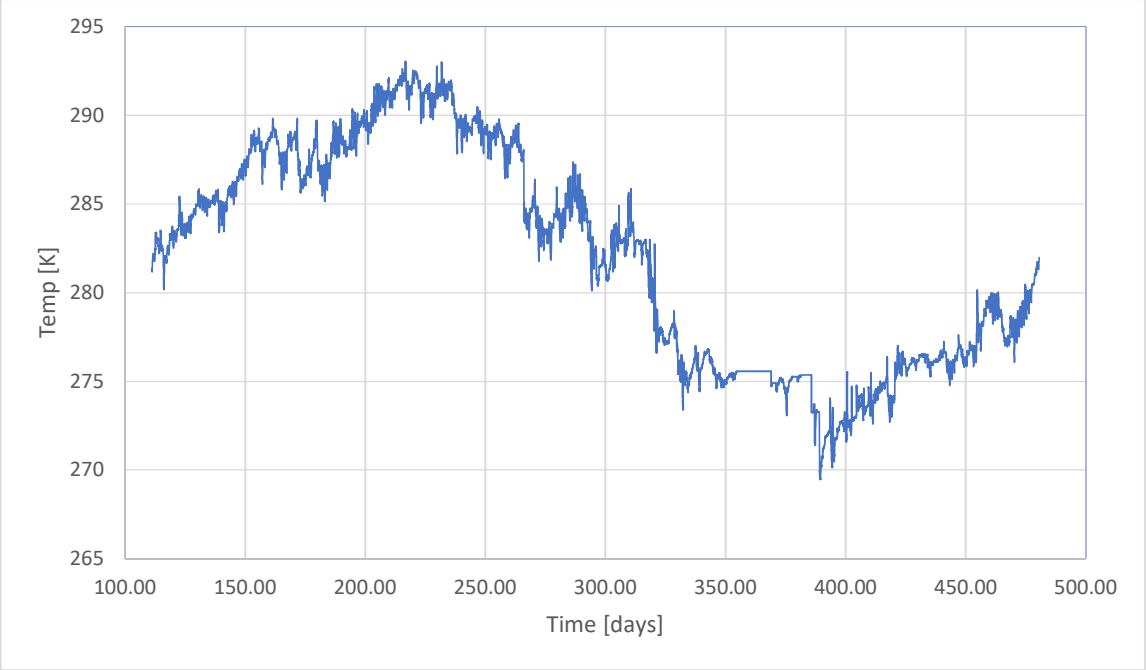

Figure C.1 - Internal temperature (avg. P5, S5 monitors) [9]

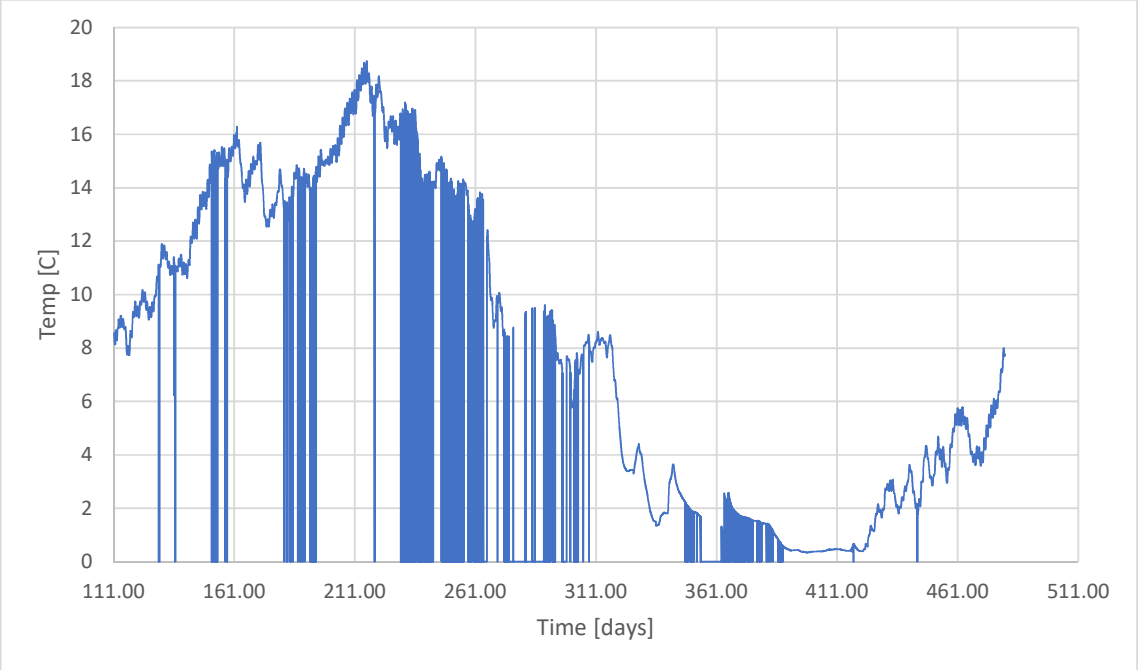

Figure C.2 - Bottom temperature (avg. P2, S2 monitors) [9]

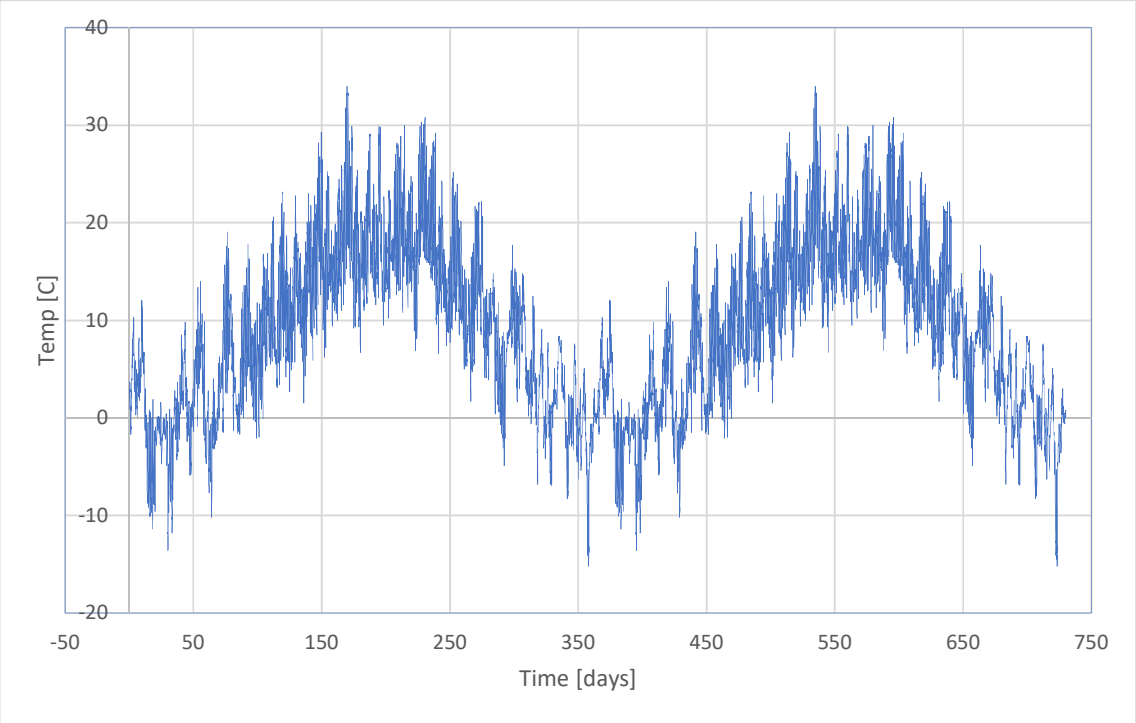

Figure C.3 - Environmental temperature climatic data [23]

APPENDIX D – TEMPERATURE DISTRIBUTION ONE YEAR CYCLE

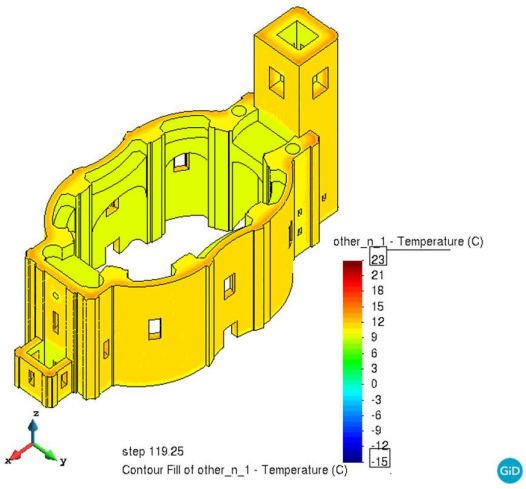

Figure D.1 - Temperature fields on 30/04/18

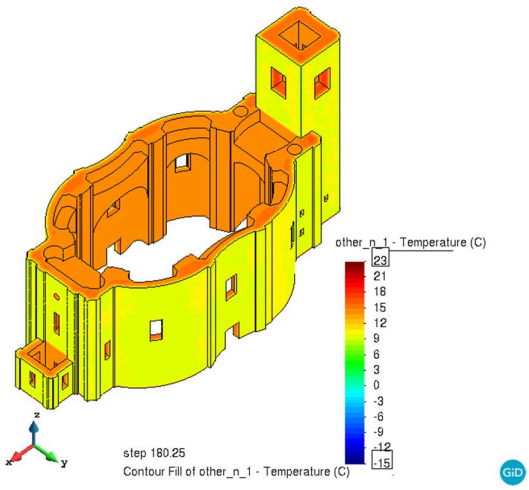

Figure D.2 - Temperature fields at 30/06/18

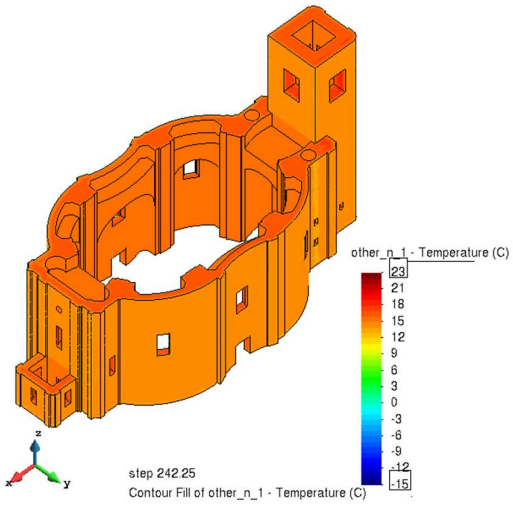

Figure D.3 - Temperature fields at 30/08/18

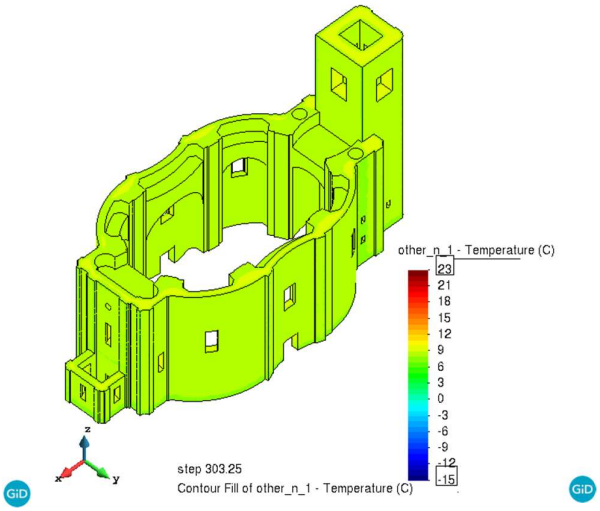

Figure D.4 - Temperature fields at 30/10/18

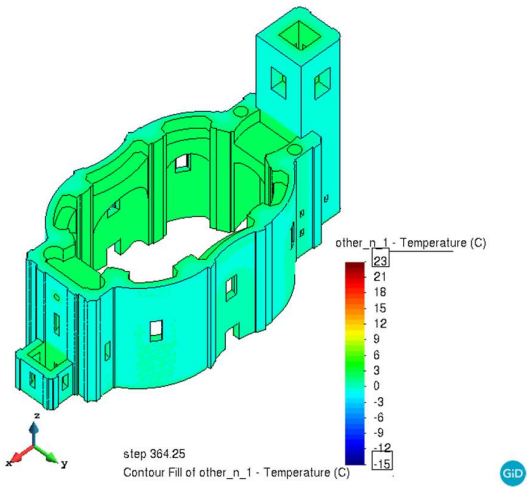

Figure D.5 - Temperature fields at 30/12/18

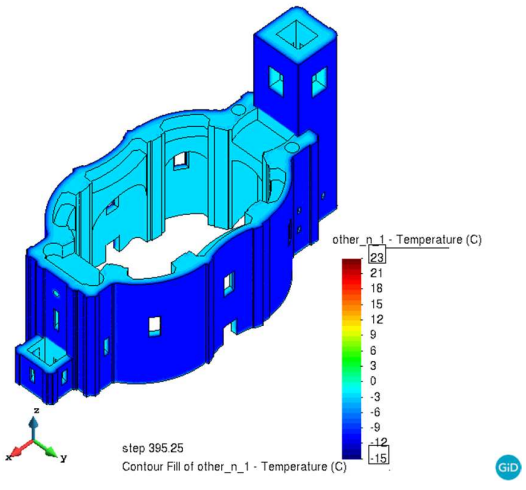

Figure D.6 - Temperature fields at 28/02/19

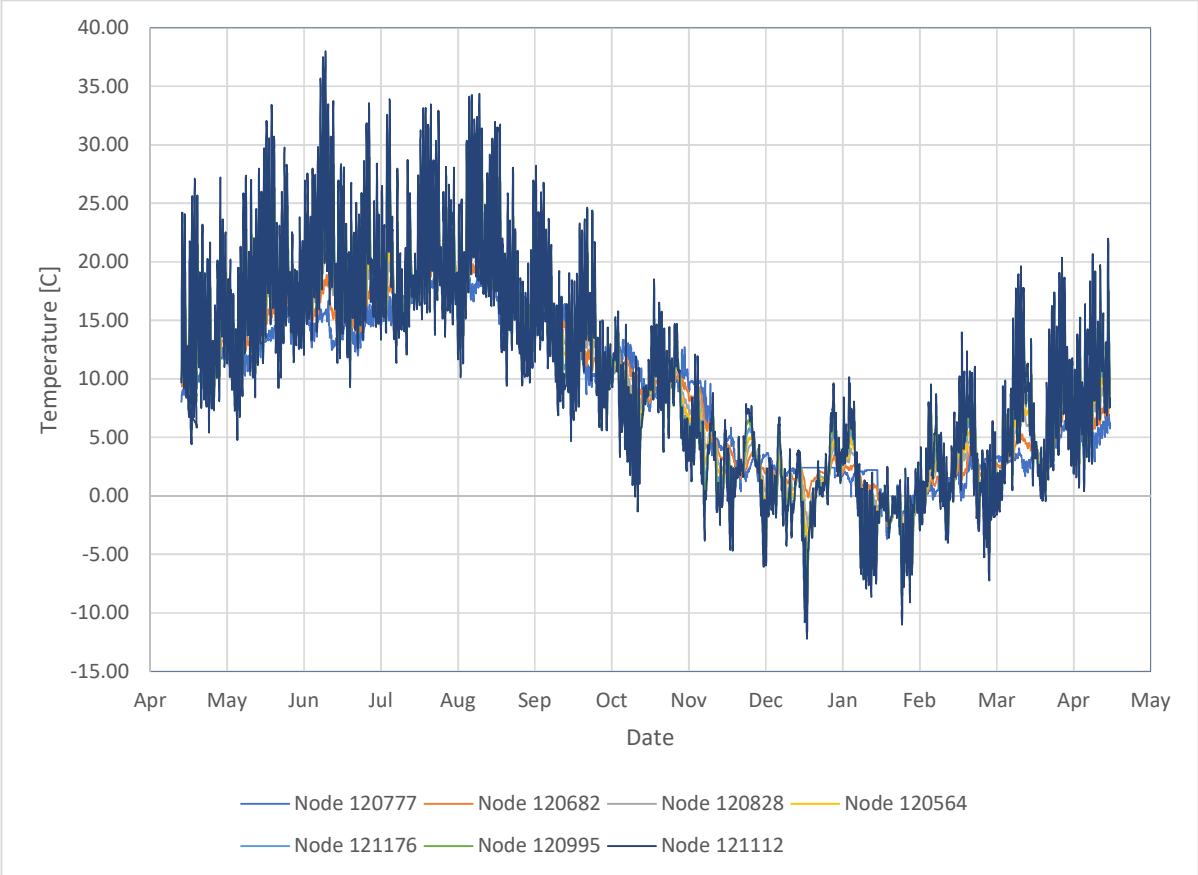

Figure D.7 - Temperature distribution measured at nodes for one year cycle

APPENDIX E – TEMPERATURE FIELDS, COMBINATION A & B

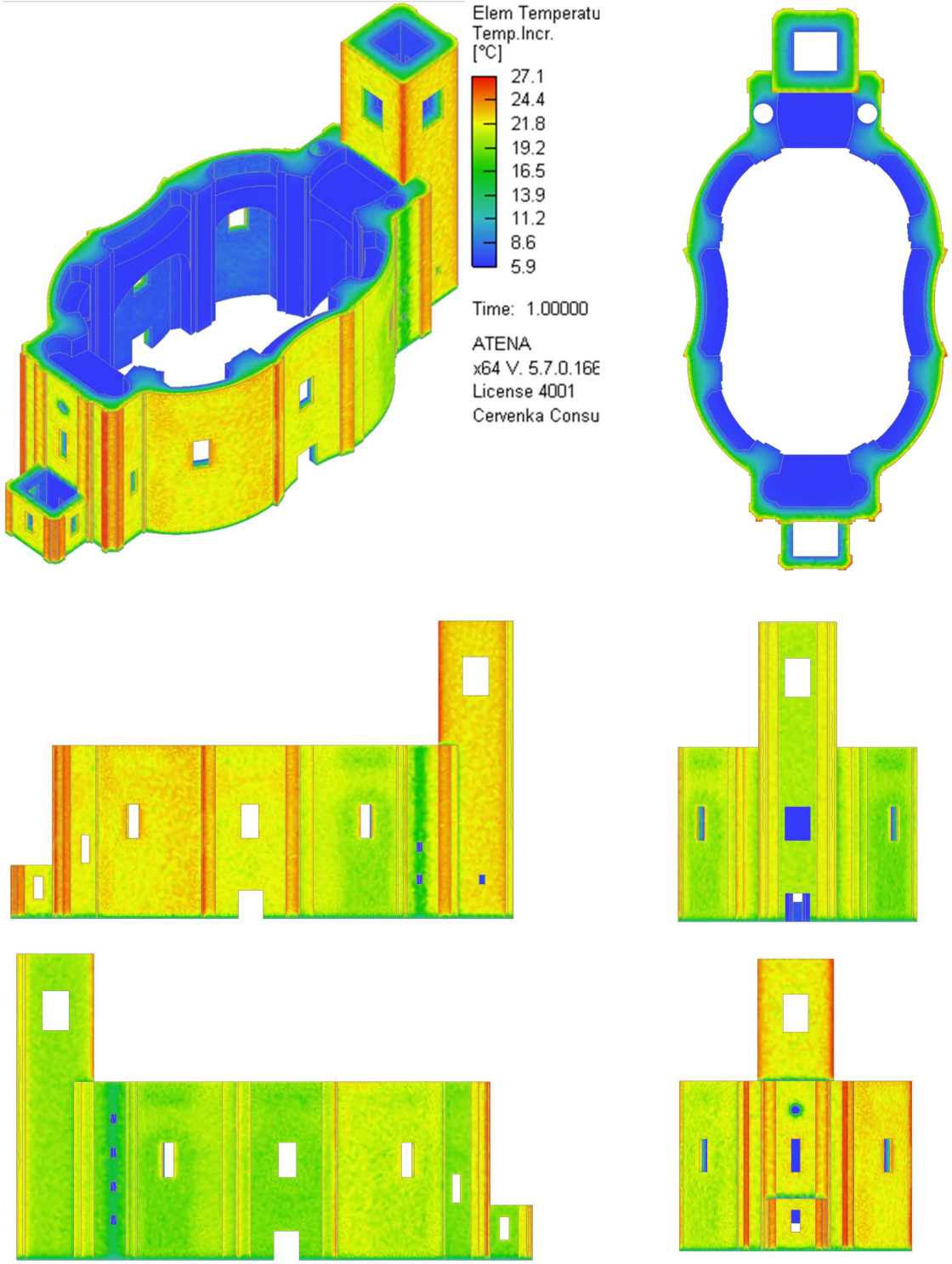

Figure E.1 - Temperature fields, Combination A

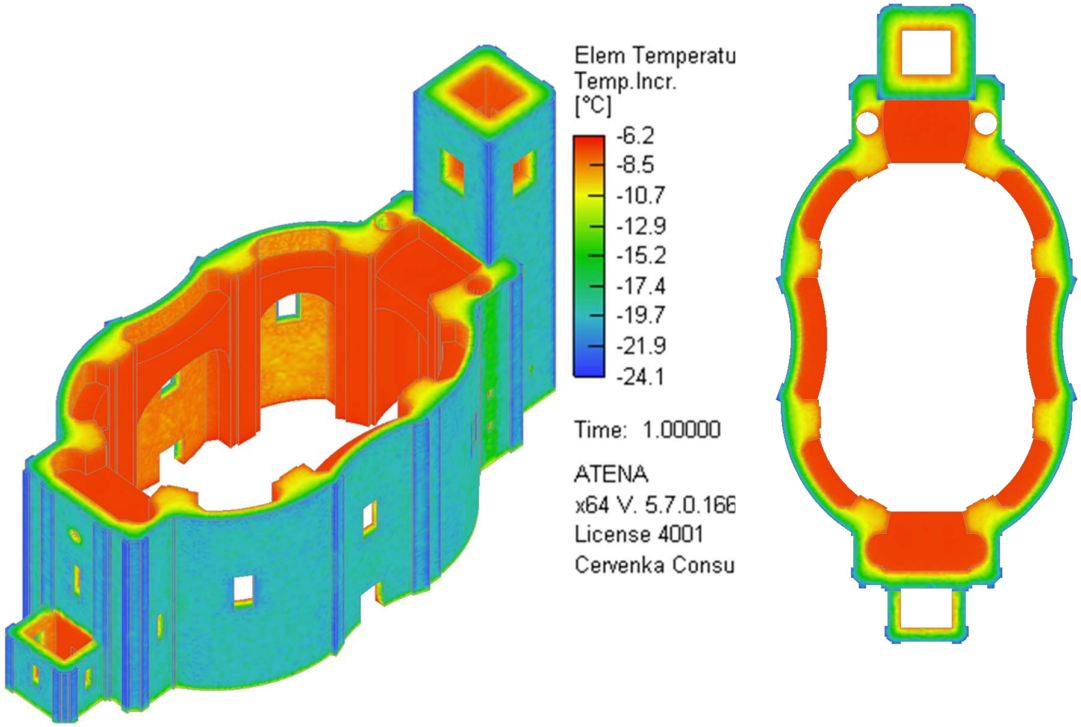

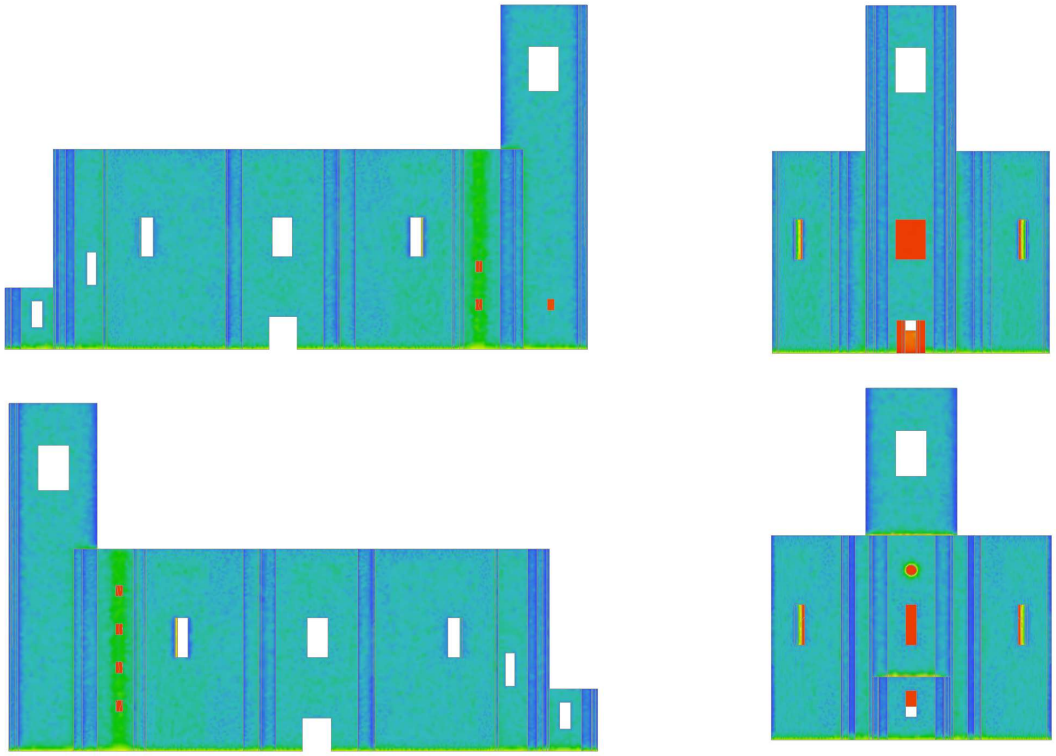

Figure E.2 - Temperature fields, Combination B

APPENDIX F – LINEAR ELASTIC ANALYSIS RESULTS

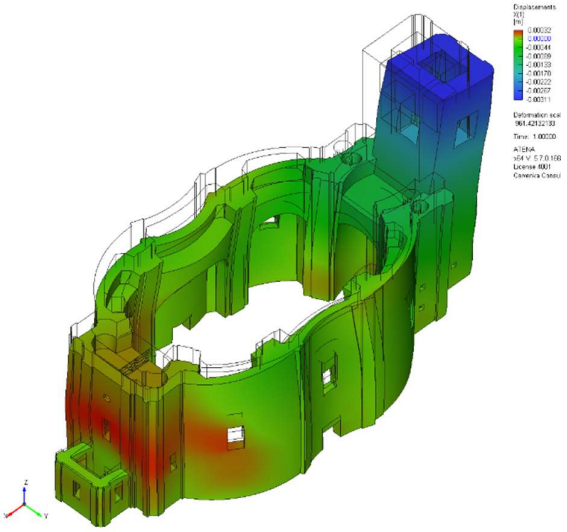

Figure F.1 - Displ. x, Load Case 3

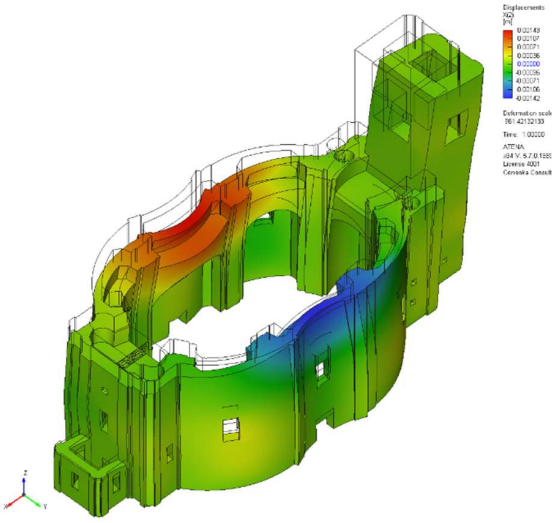

Figure F.2 - Disp. y, Load Case 3

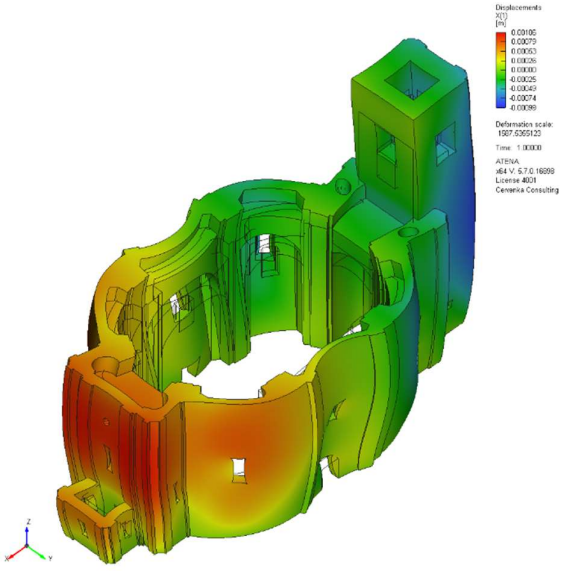

Figure F.3 - Displ. x, Load Case 4

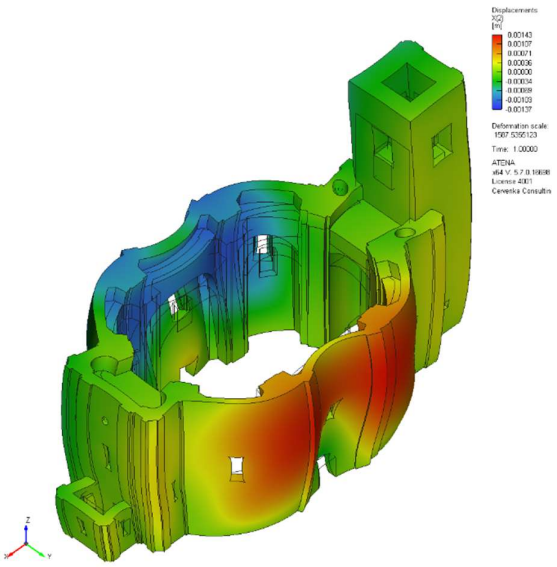

Figure F.4 - Displ. y, Load Case 4

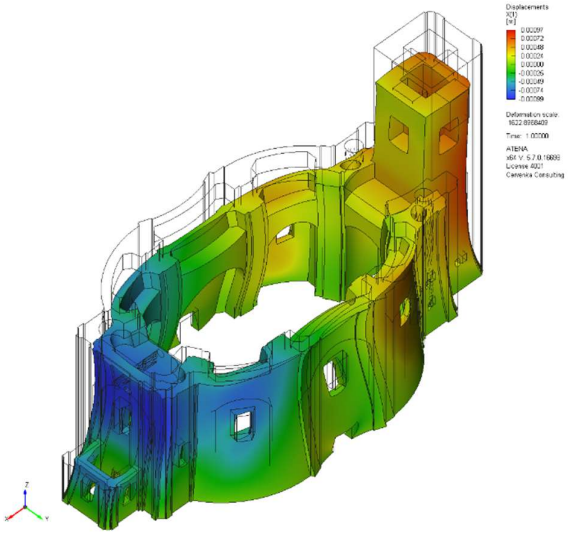

Figure F.5 - Displ. x, Load Case 5

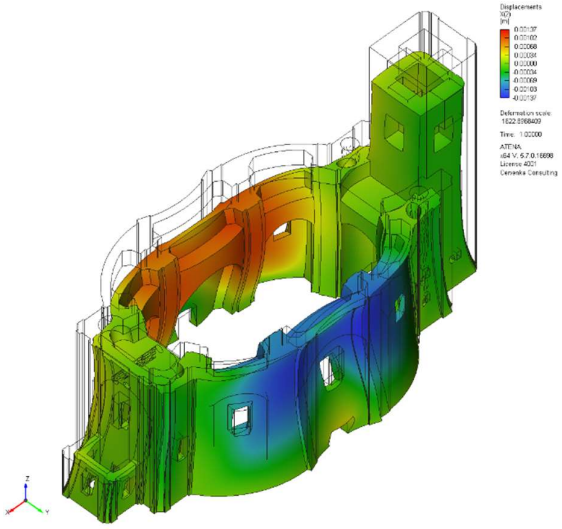

Figure F.6 - Displ. y, Load Case 5

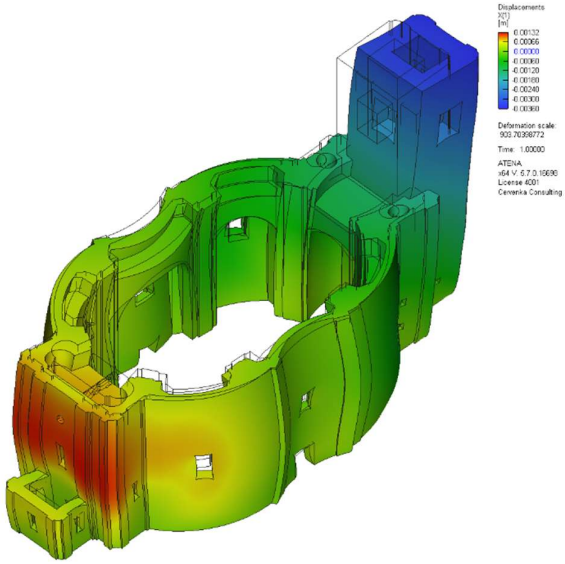

Figure F.7 - Displ. x, Load Case 6

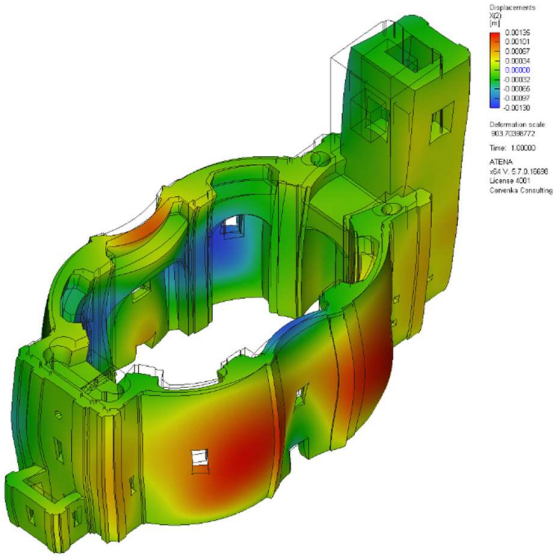

Figure F.8 - Displ. y, Load Case 6

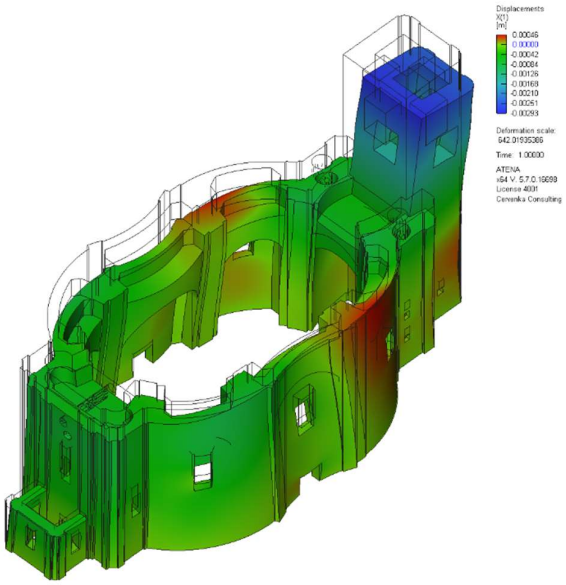

Figure F.9 - Displ. x, Load Case 7

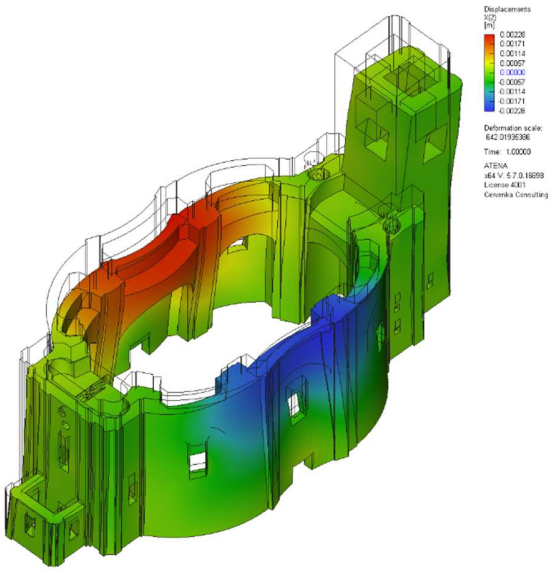

Figure F.10 - Displ. y, Load Case 7

APPENDIX G – NONLINEAR ANALYSIS RESULTS

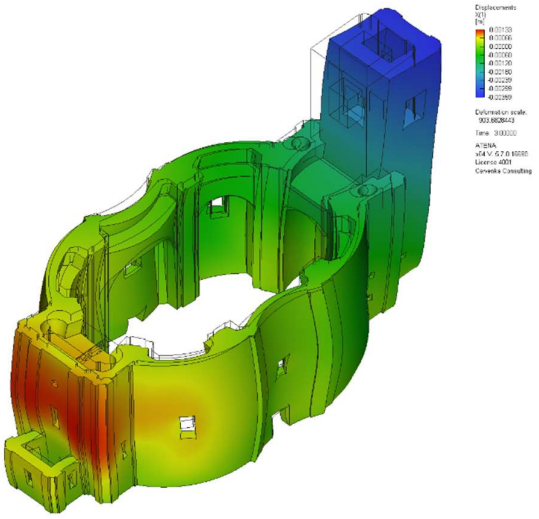

Figure G.1 - Displ. x, Load Case 8

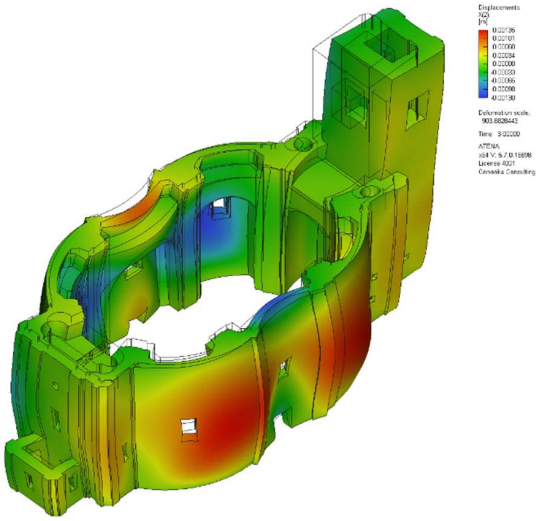

Figure G.2 - Displ. y, Load Case 8

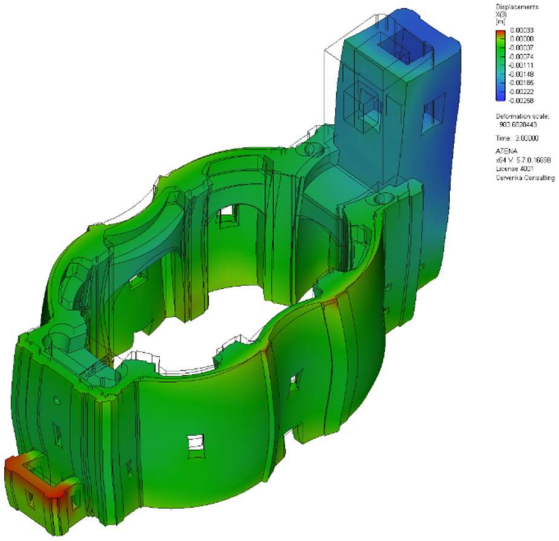

Figure G.3 - Displ. z, Load Case 8

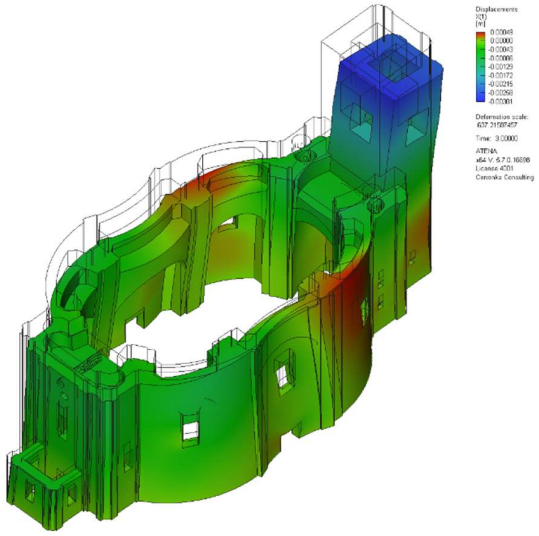

Figure G.4 - Displ. x, Load Case 9

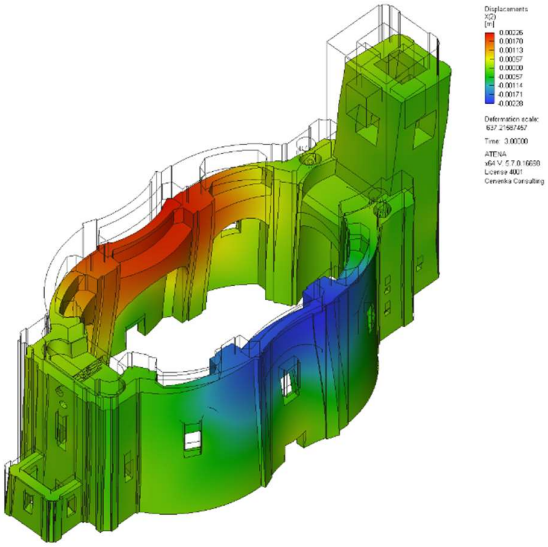

Figure G.5 - Displ. y, Load Case 9

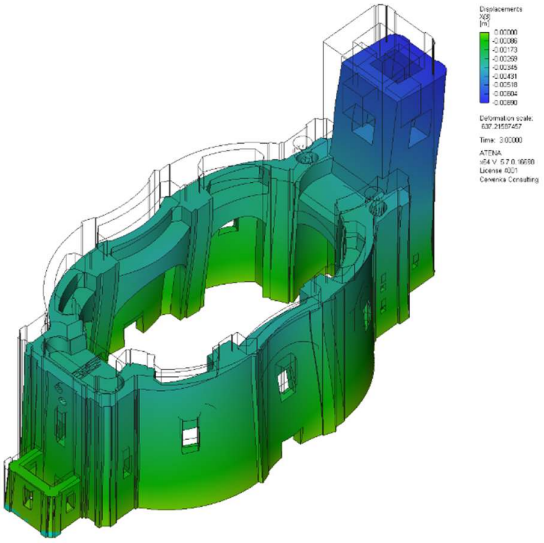

Figure G.6 - Displ. z, Load Case 9